Università degli Studi di Palermo

AREA QUALITÀ, PROGRAMMAZIONE E SUPPORTO STRATEGICO
SETTORE STRATEGIA PER LA RICERCA
U. O. DOTTORATI

CIVIL, ENVIRONMENTAL AND MATERIALS ENGINEERING.
Dipartimento di Ingegneria
ICAR 01

An innovative approach to simulate thrombosis with smoothed particle hydrodynamics

IL DOTTORE
ALESSIA VIOLA

IL COORDINATORE
PROF. GIUSEPPE CAMPIONE

IL TUTOR
PROF. ENRICO NAPOLI
PROF. GAETANO BURRIESCI

CO TUTOR
DOTT.SSA ALESSANDRA MONTELEONE

CICLO XXXV
ANNO CONSEGUIMENTO TITOLO 2023

An innovative approach to simulate thrombosis with smoothed particle hydrodynamics

“Il divertimento della ricerca scientifica è anche trovare sempre altre frontiere da superare, costruire mezzi più potenti d'indagine, teorie più complesse, cercare sempre di progredire pur sapendo che probabilmente ci si avvicinerà sempre di più a comprendere la realtà, senza arrivare mai a capirla completamente.”

(Margherita Hack)

Acknowledgement

Completing the PhD and writing this thesis has been an amazing journey that would not have been possible without the support and encouragement of many outstanding people.

My greatest appreciation and gratitude goes to my tutors Prof. Enrico Napoli for his trust, support and to give me the opportunity to return to the world of research, and Prof. Gaetano Burriesci whom I would like to thank first for advising me during all phases of my PhD, but also for giving me the freedom to find my own way in the research project and welcoming me into the Ri.MED Bioengineering Group, always making me feel at home and an integral part of a big project. Thanks! Thanks a lot!

I really cannot find the words to thank each of my amazing colleagues and friends in Ri.MED Bioengineering Group (Alessandra, Danila, Giulio, Sofia, Valentina). Spending time with you, learning and discovering so many new things has opened my mind. I am grateful for all joy and harmony shared together over these past three years. The moments and experiences spent side by side have been magnificent gifts that I will keep with me forever.

A special thank goes to my co-tutor Dr. Alessandra Monteleone who was a mentor to me. She introduced me to the fantastic world of SPH with enormous patience and preparation and taught me "to love simulations". Thank you for your support.

Last but not least, I would like to express my deepest gratitude to Fabrizio, my family and my friends. They always have supported me and shared with me both the great and the difficult moments of life. I owe them much more than I would ever be able to express. Thank you so much for your love and care.

List of Figures

List of Tables

Abstract

Thrombosis is a pathology leading to the formation of clots, that can result in arterial obstructions and, eventually, migrate through the cardiocirculatory system causing heart attack, stroke or pulmonary embolism. The process is complex and its mechanism is still unclear, being the result of the interaction between various factors, including platelet activation and aggregation, chemical reactions, and hemodynamics.

It is crucial to consider and minimise thrombosis in the design and implementation of artificial organs, such as artificial heart valves, and vascular prostheses. The study of hemodynamics can provide effective support to identify and prevent the risk of thrombosis.

Due to the lack of adequate analytical solutions and the complexity of experimental studies, research increasingly evolves towards the use of computational methods.

This thesis aims at modelling the formation, growth and evolution of thrombus by means of a Smoothed Particle Hydrodynamics (SPH) numerical method coupled with a fluid-structure interaction (FSI) model. The proposed model describes the main phases of the coagulative cascade through the balance of four biochemical species and three types of platelets. SPH particles can switch from fluid to solid phase when specific biochemical and physical conditions are satisfied. Fluid-solid coupling is modelled by introducing elastic binds between solid particles, without requiring detention and management of the interface between the two media.

In order to reach this goal, firstly the model is validated by comparing the numerical prediction with experimental data available in the literature, secondly, it is applied to describe thrombosis formation due to relevant pathologies such as atrial fibrillation and cerebral aneurysms where the insertion of flow diverter creates thrombogenic stasis zone.

Chapter 1

1. Introduction

Thrombosis is a pathology characterised by the presence of clots within the blood vessels, that limits the flow. In developed countries, acute venous and arterial thrombosis is the leading cause of death [1]. Due to intricate interactions between blood cells (including platelets), plasma proteins, coagulation factors, inflammatory factors, cytokines, and the endothelial lining of vessel lumens, blood flows freely in vessels.

Recently, the attention of research on the phenomenon of thrombosis has grown also due to the complications that have emerged in patients affected by Covid 19. In fact, although the connection is still a source of debate, a prothrombotic condition is brought on by COVID-19 [2], and the high frequency of significant thrombotic events that have been reported prompts worry about a specific prothrombotic aetiology. In the vasculature of the lungs, spleen, brain, gut, and peripheral areas of COVID-19 patients, micro- and macro-vascular thromboembolic or in situ thrombotic consequences have been noted. There have been reports of arterial and venous thromboembolism developing despite preventive or fully therapeutic anticoagulation, frequent thrombus formation in hemodialysis circuits, strokes as a presenting symptom in young patients who were previously healthy, and more. Patients who were otherwise asymptomatic have reported the incidence of thrombotic episodes. Another evidence that the prothrombotic state may persist for several weeks or even longer after hospitalisation comes from the identification of thrombosis both in the acute context and in the weeks after critical illness.

Other interesting aspects of this process regard the complications related to the place the thrombi are located, in fact, the most serious problems include stroke, heart attack, and serious breathing problems. The diagnosis and treatment of thrombosis are therefore very complex. Furthermore, heart valves, stents, and other blood-contacting medical devices are frequently used to treat cardiovascular problems and thrombus development is a frequent reason for these devices to malfunction. The use of

antiplatelet drugs and/or anticoagulants is therefore common to prevent or cure thrombi that form on blood-contacting medical devices, that typically consist of platelet aggregates and fibrin.

It is crucial to understand how blood-contacting medical devices trigger clotting in order to effectively manage it. Given the phenomenon's complexity from several points of view (medical, biological, etc), it is fundamental to study the process in depth. Taking a broader view of the problem will enable better understanding and perhaps intervening with appropriate treatments or interventions. In this particular context, the development of computational models have allowed to predict localised thrombus risks in patient-specific geometries.

1.1 *Research Objectives and Thesis Outline*

The main purpose of this thesis is to develop a computationally efficient approach to simulate thrombus formation, growth and dissolution in patients affected by pathologies, such as atrial fibrillation, or treated with biomedical devices, such as flow diverter employed for cerebral aneurysms. In the literature, several studies examined how to predict thrombosis under various circumstances; however, most of these studies focus on simplified geometries and neglect the effects of thrombus growth on fluid flow.

To overcome these limitations, a novel thrombus formation model has been developed based on a monolithic Fluid-Structure Interaction (FSI) approach, realised using the Smoothed Particle Hydrodynamics (SPH) numerical method. This thesis presents a numerical model capable of integrating the biochemical nature of the process with the hydrodynamic and physical variables that influence or favour it. Furthermore, thanks to the mesh-less feature of the SPH method, it can be applied to model complex geometries or used as a diagnostic tool to support selection of pharmacological or surgical treatments. In this research, the open-source software PANORMUS (PArallel Numerical Open-souRce Model for Unsteady flow Simulations), which contains a SPH solver, was employed.

The thesis is organised into six chapters and one appendix that are briefed as follows:

- Abstract

- Chapter 1 introduces briefly a background knowledge on thrombosis. The motivations and objectives of the thesis are outlined;
- Chapter 2 gives a literature review on cardiovascular diseases and biological nature of thrombus formation. An overview of the state of the art of numerical models used to treat thrombosis is also provided;
- Chapter 3 describes the fundamental and basic concepts of the SPH method, explaining the most relevant aspects of the PANORMUS-SPH code;
- Chapter 4 proposes a novel thrombosis model. It describes all equations involved and presents the spring model used to simulate thrombus formation, growth and dissolution. A benchmark test (backward-facing step) is used to validate it;
- Chapter 5 presents two case studies where the SPH thrombus model is applied, associated with different pathologies: thrombi induced by biomedical devices such as the flow diverter in cerebral aneurysms and thrombi formed and grown in the left atrial appendage LAAs under atrial fibrillation conditions;
- Chapter 6 draws main conclusions and suggests possible future research directions;
- Appendix A describes the MATLAB tool designed to transfer information between the commercial software ANSYS and PANORMUS.

Chapter 2

2. Background and Literature Review

2.1 Cardiovascular system

The circulatory system has a vital role in sustaining human life, as it is responsible for providing oxygen and nutrients to the cells and for removing waste products and CO_2. One of the major elements that composes the circulatory system is the cardiovascular system. Its primary function is circulating blood to the major organs and tissues, and it consists of the heart, vessels, and blood.

The heart is a muscular organ that pumps blood into two separate circuits (the pulmonary and systemic circulation). The left and right sides (red and blue representation in Figure 1) of the heart carry out different functions: while the left side is liable for systemic circulation and pumps oxygenated blood and nutrients to the organs, the right side manages pulmonary circulation and blood oxygenation. Each of the two parts is composed of two elements, an atrium, where blood enters, and a ventricle, from which blood is pumped into blood vessels (as shown in Figure 1).

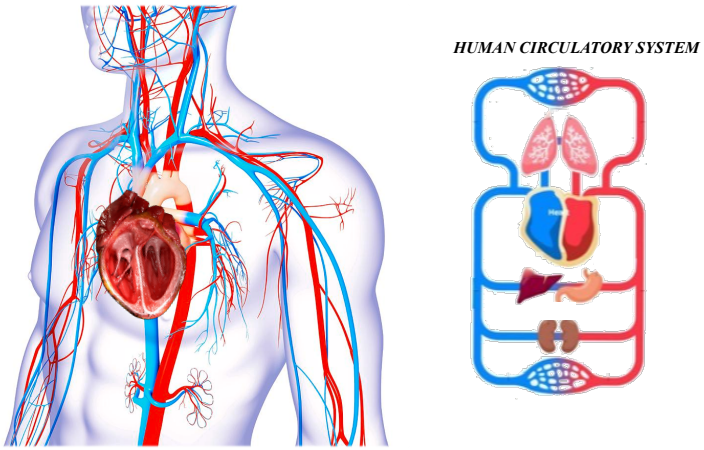

Figure 1 - Representative diagram of the cardiovascular system: blue line indicates the right side and the red represents the left side (image adopted from https://theheartfoundation.org/2017/05/19/cardiovascular-system/)

Blood consists of several components, including plasma, platelets, red and white blood cells as shown in Figure 2. Plasma constitutes about 55 % of the total blood volume and is mainly composed of water (up to 90-95 %) along with different dry substances, such as dissolved proteins (6-8 %), glucose, coagulation factors, electrolytes, hormones, carbon dioxide and oxygen. The remaining 45 % of the volume is composed of platelets, white blood cells and mainly Red Blood Cells (RBC).

Blood and nutrients are transported to organs and tissues through a complex network of blood vessels composed of arteries, veins, arterioles, venules and capillaries, characterised by different diameters and structures.

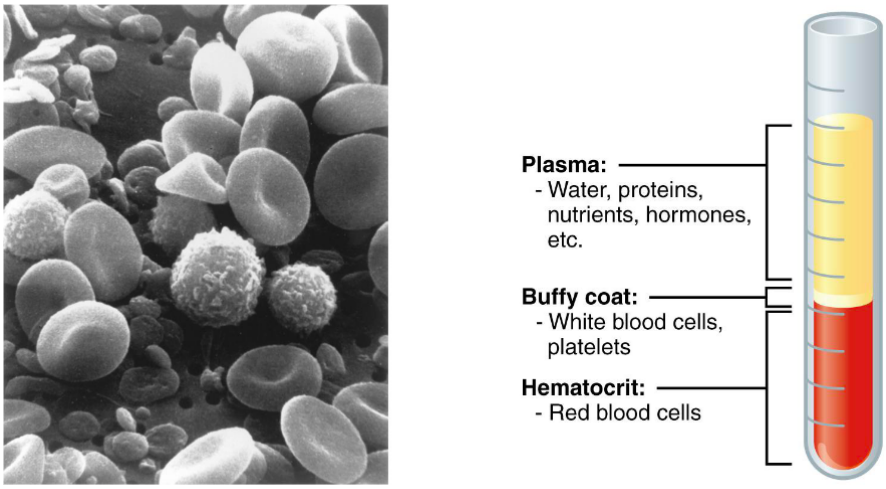

Figure 2 - Circulating human blood (left) and a schematic representation of the blood composition (right). The image is taken from [3]

Vessels constitute the ducts through which blood flows. The arterial and venous systems have a tree structure. The section of the arteries decreases from the aorta towards the periphery, but at the same time there is an increase in the number of vessels in parallel, so the total section increases with a consequent decrease in speed allowing a greater transit time at the capillary level. Conversely, it occurs on the venous front, where there is a progressive increase in the caliber of the vessels from the periphery to the heart with a decrease in the number of branches in parallel. Blood vessels have a complex and diversified structure from area to area about the specific function to be performed.

The human cardiovascular system is an incredibly complex system in which the ability to communicate between parts is the most surprising and important aspect.

2.2 Cardiovascular system disease (CVD)

Cardiovascular diseases are the leading cause of death in Europe accounting for 32,88 % of deaths (see Figure 3). They also constitute the most demanding expenditure of the health systems in the old continent. It is estimated that if the major forms of cardiovascular diseases were eliminated, life expectancy would increase by at least seven years [4], [5].

From the Second World War to today, in the most developed countries, epidemiological data have shown a transition process from infectious diseases to an increase in chronic degenerative diseases. The term "chronic degenerative diseases" indicates non-communicable diseases that are based mostly on common and modifiable risk factors, such as cardiovascular dysfunctions, cancer and diabetes.

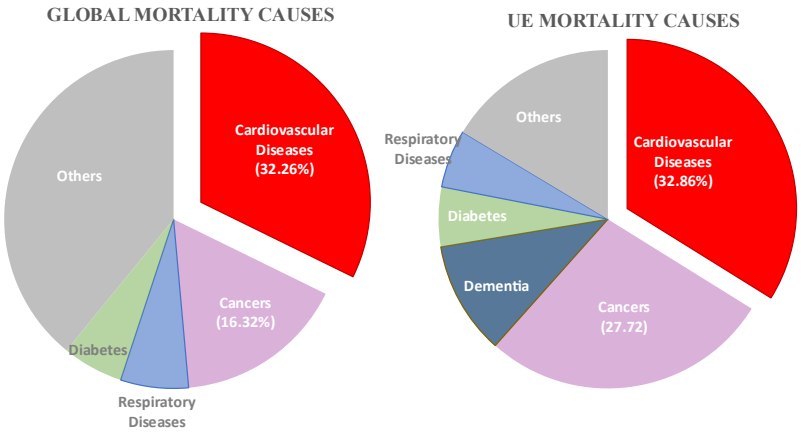

Figure 3 – Statistical data of mortality causes (World and European Union)

By the year 2030, the UN Sustainable Development Goals aims to reduce premature mortality from non-communicable diseases by a third. Cardiovascular diseases (which include coronary heart disease and stroke) are the most common non-communicable diseases globally and are associated with a group of disorders of the heart and blood vessels. Figure 4 identifies several types of heart disease.

Coronary Artery Disease (CAD) is caused by atherosclerosis in the coronary arteries, which are the vessels carrying blood to the heart muscle. A heart attack and heart failure can occur when arterial plaque makes blood flow through them difficult.

Congestive Heart Failure is a critical, chronic illness that worsens over time. Heart failure indicates that the heart is no longer performing its function as intended. The heart may begin pounding more quickly and expand in size to compensate for this.

This is typically associated with a growth of the heart, to add muscle power and stroke to compensate the loss in pumping efficiency.

Have heart valve disease is associated with malfunctions of one or more of the heart's valves. Heart valve disease can be caused by stenosis, which occurs when the leaflets of the heart valves get too thick or stiff and do not open properly, making it difficult for blood to pass through; or regurgitation, which occurs when the leaflets of the valve do not close properly.

Heart arrhythmia indicates irregularities in the heart beat —either by beating too quickly or too slowly—. While some people can develop this illness over time, some people are born with it.

Pericarditis happens when the pericardium, a tissue sac surrounding the heart muscle becomes inflamed or swollen.

Cardiomyopathy is a form of the cardiac condition that can weaken the muscular heart tissue, making it more difficult for the heart to pump blood effectively. This could promote heart failure and/or heart valve issues.

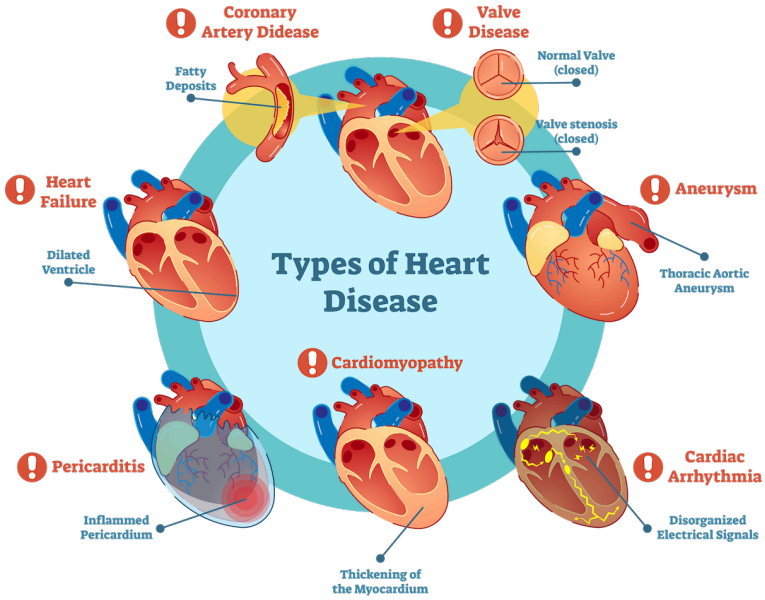

Figure 4 – Description of types of heart disease (image taken from /www.udmi.net/cardiovascular-disease-risk)

Thrombosis is one of the main causes of CVD, which results in the formation of a clot that can obstruct the physiological blood circulation, or fragments that flow through the cardiovascular system to critical organs, thus causing disorders such as ictus, stroke or pulmonary embolism. Paragraph 2.3 will deal with this pathology in greater detail.

2.3 Cardiovascular thrombus

A thrombus is a blood clot that forms inside a vessel when the hemostatic process becomes abnormally activated and can result in partial or complete obstruction of the vessel lumen. When the lumen is only partially barred (see Figure 5), the altered haemodynamics, caused by the narrowing, may produce the growth of the clot and, eventually, levels of shear stress and pressure differences sufficient to detach the full clot or parts of it from the anchor region. These masses, released in the bloodstream, can travel to smaller vessels, and obstruct the blood supply to the downstream tissues, causing their death.

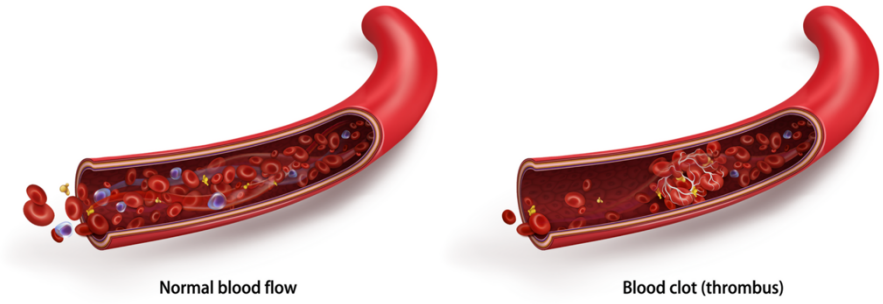

Figure 5 – Difference between normal blood and blood with clots

Thrombus formation associated with pathologies, such as atrial fibrillation or cerebral aneurysm, might cause fatal consequences. Furthermore, recent studies have underlined that thrombosis has emerged as an important complication of coronavirus disease 2019 (COVID-19), particularly among individuals with severe illness [6]. However, the precise incidence of thrombotic events remains uncertain, but the detailed knowledge of the process and the intervention of each player (platelet, enzymes, blood) involved, could support the prevention of cardiovascular complications.

2.4 Mechanism of Thrombosis

As said above, the thrombus is a solid mass consisting of red blood cells, platelets, fibrin, and white blood cells, resulting from alterations in the vascular endothelium, blood flow, or blood clotting mechanisms. The knowledge of hemostasis and blood clotting is fundamental to understanding thrombus formation.

There are two main types of thrombosis (see Figure 6) depending on which blood vessels are blocked, and it is possible to distinguish:

- Red thrombus: is associated with red blood cell infiltration and happens when a blood clot blocks an artery. In addition to transporting oxygen-rich blood from the heart to the rest of the body, arterial thrombosis can also be very dangerous. It is possible to suffer a heart attack if a blood clot forms in the main arteries of the heart. Blood clots in the brain's arteries can cause strokes.
- White thrombus: is rich in fibrin with few cellular elements. Usually, a blood clot blocks a vein. Veins carry oxygen-depleted blood from the body back to the heart, and blockages can cause serious problems. An example of venous thrombosis is deep vein thrombosis (DVT), which most commonly affects veins in the legs, such as the femoral vein.

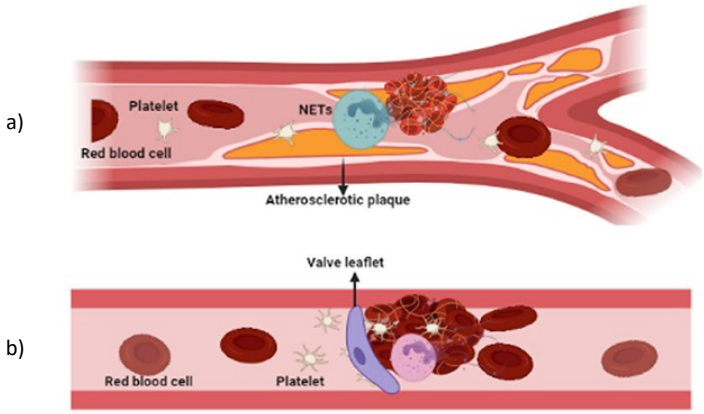

Figure 6- Arterial (a) and Venous (b) thrombus

Thrombus formation is a complex biological process involving many chemical and biological species, transport phenomena, and kinetic processes. The chemical and biological nature of this phenomenon will be discussed in paragraph 2.4.

The coagulation process is a sequence of events designed to limit potential blood losses, thus leading to hemostasis.

Hemostasis is a complex physiological process due to the interaction among blood, platelets, clotting factors, and coagulation inhibitors. The process can be subdivided into primary and secondary hemostasis.

Primary hemostasis, begins with the activation of platelets by thrombogenic materials, including subendothelial collagen, thrombin, adenosine diphosphate (ADP),

epinephrine (Epi), arachidonic acid (AA) or foreign materials. Platelet surface activation receptors, GPIa / IIa, and GPVI glycoproteins are important for the activation of the platelet surface by collagen. Platelet activation, aggregation, and secretion are driven by platelet surface activation receptors, P2Y1 and P2Y12, which bind to ADP. After activation, the process of platelet adhesion, aggregation, and secretion occurs. The platelet surface receptors, GPIb, which binds to von Willebrand factor (vWF), and GP Ia / IIa, which binds to collagen, activate the platelets which undergo shape changes making them extremely adhesive. The activation also carries the entire GPIIb / IIIa platelet receptor, which is the largest. This receptor binds to vWF and fibrinogen, leading to platelet aggregation. Activated platelets also secrete numerous proteins including ADP, thromboxane A2 (TXA2), serotonin, fibronectin, thrombospondin, fibrinogen, platelet-derived growth factor, and others. These factors recruit and activate additional platelets, stabilize platelet aggregates and induce vasoconstriction. This phase represents the final stage of primary hemostasis and the result is the formation of the platelet plug.

The coagulative cascade is the process behind the thrombus formation and represents the heart of secondary hemostasis. The coagulation cascade leads to fibrin polymerization and platelet plug stabilization, and involves a number enzymes and zymogens, called 'factors' that circulate in their inactivated state. Upon a specific biochemical signal, they initiate a series of biochemical reactions that contribute to forming the blood clot. The coagulation factors that circulate in blood in their inactive form are listed in Table 1.

In particular, the coagulation cascade can be initiated through two parallel pathways defined as intrinsic and extrinsic (Figure 7).

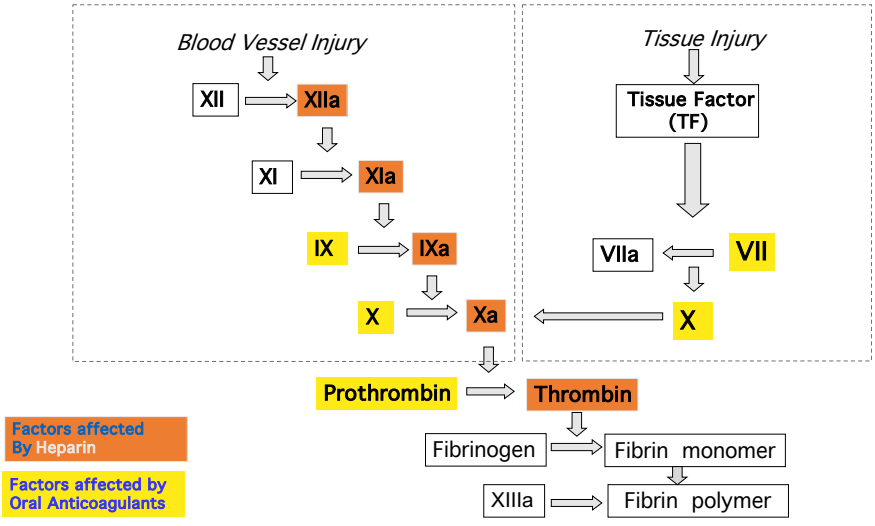

Figure 7 – Coagulative Cascade: extrinsic and intrinsic way

The Tissue Factor (TF) activates the extrinsic pathway, which is present in the subendothelial tissue. Under normal physiological conditions, the vascular endothelium minimises the contact between TF and plasma procoagulants, while in the case of vascular damage, TF binds to factor VIIa promoting the conversion of factor X into Xa. As for the intrinsic pathway, it begins with the activation of factor XII which in turn leads to the activation of factor XI that, once activated, leads to the activation of factor IX. Factor IX acts with its cofactor to form a complex on a phospholipid surface that allows the activation of factor X. Finally, there is a common pathway that is a "crucial" phase because the activated factor X together with its cofactor, tissue phospholipids, platelet phospholipids, and calcium form the prothrombinase complex that converts prothrombin (II) to thrombin (IIa). The latter acts as an enzyme to transform fibrinogen (I) into fibrin filaments (Ia) that surround the platelets, blood cells, and plasma, leading to the formation of the clot. The result is the formation of the fibrin clot which is deposited on the mesh of the platelet plug (previously activated by primary hemostasis) and is stabilised in a "red clot" (indicated as fibrin polymer in Figure 7. A lot of enzymes are involved during the coagulative cascade which are inserted in Table 1.

Factor	**Names**	**Physiological mean**	**Clinically range**	**Type**	**Way**
I	Fibrinogen			Protein	Common
II	Prothrombin	1.4 μM	0.8-2.0	Serine Protease	Common
IV	Calcium ion			Chemical element	Common
V	Labile factor	20 nM	12-28	Cofactor	Common
VII	Proconvertin	10 nM	6-14	Serine Protease	Extrinsic
VIII	Antihaemophilic factor	0.7 nM	0.4-1.6	Cofactor	Intrinsic
IX	Christmas factor	90 nM	64-135	Serine Protease	Intrinsic
X	Stuart Power factor	160 nM	96-224	Serine protease	Common

ATIII	Antithrombin	3.6 μM	3.2-6.3		
TFPI	Tissue Factor Pathway Inhibitor	2.5 nM	1.1-4.3	Cofactor	Extrinsic

Table 1 – Circulating inactive coagulation factors and their mean physiological concentration in blood (values taken from [7])

2.4.1 Causes of thrombus formation

Thrombus formation and its pathological role have been investigated for centuries, however, only in the second half of the nineteenth century, some fundamental progress was made to provide some systematic understanding of the process. In 1856 Virchow [8] published his observations on the influence of blood flow conditions on platelet activation and, consequently, on thrombus formation. This led to the elaboration of *Virchow's triad*, which identifies changes in blood components (*hypercoagulability*), vessel wall surface (*endothelial injury*), or flow characteristics (*stasis*) as synergic contributors to the phenomenon, as shown in Figure 8.

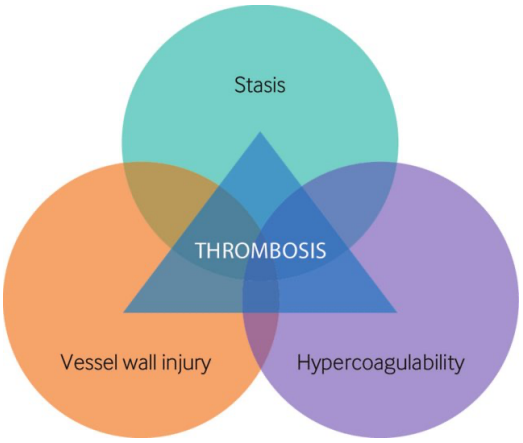

Figure 8 – Virchow's triad (image taken from [9]).

Nowadays this theory is still accepted and used to predict the process. Each of the three elements of Virchow's triad can act independently or simultaneously on the formation of thrombi.

The condition of hypercoagulability can be caused by genetic or acquired disorders, such as cancer, liver diseases, obesity, smoking, and birth control, and could

increase concentrations of procoagulants (fibrinogen and Factor VII) or reduce values of anticoagulants (like antithrombin and protein-C), or create a condition of high viscosities or local hemodynamic changes [10].

Trauma, rupture of atherosclerotic plaques, and high shear stress may lead to injury and exposure to tissue factors, which will stimulate immune responses, induce platelet activation and initiate clotting. Several studies have focused on understanding shear rates and stress on platelet activation. These parameters act as a physical agonist on platelet activation, promoting morphological changes in the structure of the cells by applying elongation constraints and at the same time affecting endothelial function and causing red hemolysis with subsequent release of ADP, a chemical agonist for platelet activation. Regions of recirculation and stasis are generally characterized by high residence times, allowing the accumulation of coagulation factors and preventing their dilution.

These areas are generally exposed to low shear rates. Shear rates lower than physiological values stimulate atherogenic and thrombogenic phenotypes. In low shear conditions, cell-cell interactions are enhanced, resulting in an increase in viscosity and sedimentation is favoured by fibrinogen, as opposed to high shear conditions where VWF and fibronectin are more involved. The composition of thrombi formed under low shear conditions is usually rich fibrin and platelets (white thrombus) differently from arterial thrombi which usually form near high shear regions

2.5 Numerical models for thrombosis modelling

Given the complexity of the process and the large number of chemical or physical variables involved numerical modelling represents an attractive tool to simulate the phenomenon of thrombosis. Different coagulation models can be used for specific purposes. They differ in many aspects, including physical properties to consider, scales of phenomena, and biochemical models coupled with biomechanics. There are also important differences in the mathematical formulation of the coagulation models and the numerical methods used to solve them [11].

For example, microscopic thrombus models are methods that consider microscale objects, like cellular scale matter with dimensions of the order of 1–10 μm. These models resolve all these items and can better convey the significance of RBCs,

platelets, and other microparticles in the blood coagulation process. Only at this scale blood cell motility, deformation, aggregation, adhesion dynamics, and other microscopic behaviour can be accurately characterised. Therefore, the primary goal is to obtain detailed and high-resolution simulation results. Moreover, any macroscopic (continuous or statistical) models cannot adequately represent the blood flow and, consequently, blood coagulation in microvessels, which are vessels with a diameter of the same order of magnitude as the size of RBCs. At this scale, the continuity hypothesis is no longer true, necessitating the usage of models explicitly accounting for blood cells [11].

The class of macroscale models is based on the continuum hypothesis and macroscopic description of blood with typical scales being larger than 100 μm. At this scale, it is believed that single particles cannot be resolved, the particulate nature of blood is not crucial, and continuum description can be employed without incurring in significant inaccuracy. One may explain the coagulation process and thrombus formation by using macroscopic variables and characteristics like velocity, concentration, viscosity, or diffusivity. The macroscopic approach typically relies on the solution of the Navier–Stokes equations and convection-reaction–diffusion equations [12].

Considering the classification cited above, literature has suggested many methods based on statistical, discrete, and continuum models to forecast thrombosis and characterise the various biochemical and physical pathways involved in the production of blood clots.

The relationship between local flow characteristics and thrombus formation have been the subject of numerous experimental and computational research. Blood clot size and shape, thrombi formation and growth rates, and local fluid dynamics are all important aspects. For example, Stein *et al.* [13] examined the impact of turbulence on thrombus development in canine femoral arteries and veins through experimental works. They revealed a positive association between Reynolds numbers and the weight of the thrombi. Other researchers studied the relationship between thrombus formation and hydrodynamics parameters such as shear strain rate (SSR).[1] For example, Hellums [14] defines a shear stress threshold that is influenced by the stress magnitude and the exposure time. Considering the influence of SSR on thrombosis, several studies

[1] Shear strain rate: a measure of the flow velocity correlated to the dimensions of the space crossed, linked to the rheological response as well as to the thrombogenicity of blood.

analysed the complications of pathologies such as aneurysms or stenosis when thrombosis occurs [15]–[17]. The studies on fluid dynamics discussed above investigate the role of blood flow in thrombus formation, but they ignore the intricate role of biochemical pathways at play. As a result, these models cannot predict growth rates, thrombus composition, and potential embolization. In the literature, more complete models were put forth that incorporate fluid flow with chemical processes as well as the transport of various species using continuous or Lagrangian methods.

Another interesting classification of thrombus modelling regards the computational approach used to simulate the process. Generally, we can distinguish computational fluid dynamics (CFD), that uses numerical analysis to analyse and solve problems that involve fluid flows [18], and the fluid-structure interactions (FSI) approaches, where structural and fluid problems are described and mutually solved [19].

Most of the macroscopic models are based on CFD analysis, where convection-diffusion equations are solved to describe the interaction between blood flow and chemical or biological agents involved in the thrombosis process. In this framework, Sorensen *et al.* [20] defined a novel model able to show the mechanism of platelet activation and aggregation in the proximity of the vessel wall, including the action of chemical agonists species, through a weight function. Moreover, they emphasised the key role of thrombin during thrombus formation. Leiderman and Fogelson [21] presented a novel continuum blood clotting model to reproduce the interactions among the main chemical species, the platelet concentration, and flow transport aspects linked to shear rate. Anand *et al.* [22] described the formation and dissolution of blood clots using biochemical reactions and rheological factors, focusing on the role of fibrin.

CFD simulations have also been used to understand complex pathologies involving thrombus formation. In this context, Sarrami *et al.* [15] developed a computational model to predict the thrombogenic dynamics in intracranial aneurysms treated with flow-diverter devices. Menichini *et al.* [23] proposed a novel haemodynamics-based model to predict the formation of thrombus in type B aortic dissection, where shear rate, fluid residence time, and platelet distribution were used to evaluate thrombosis and stimulate its growth. Vella *et al.* [24] evaluated thromboembolic risk in the left atrial appendage under atrial fibrillation pathology using an ideal geometry and imposing the wall movement under different blood flow conditions.

Although in the literature there are numerous examples of mathematical models or CFD techniques that describe blood clotting or thrombus formation, fluid-structure interaction (FSI) approaches have recently been applied to describe the process more realistically. Generally, FSI is used to model multiphysics phenomena that occur in systems where the fluid flow and deformable structure interact synergically, as in common cardiovascular applications [25]. FSI approaches can be classified into partitioned and monolithic. In partitioned FSI, two different solvers are used to describe the fluid and solid phases, and mutual interaction occurs at the interface separating the two domains. In particular, fluid flows are commonly described using Eulerian[2] formulations, whilst solid structures are modelled through Lagrangian[3] approaches. The coupling of the fluid and solid domains is commonly achieved by employing Arbitrary-Lagrangian-Eulerian [26]–[29] techniques or Immersed Boundary (IB) strategies [30]. On the other hand, in monolithic methods both solid and fluid domains are treated with a unique solver and no interface is required. In this case, Fully Eulerian [31], [32] or Lagrangian [33]–[37] formulations are adopted in the whole domain. In the context of the Lagrangian particle method, smoothed particle hydrodynamics (SPH) has recently been adopted for the modelling of thrombosis considering the influence of blood flow, platelets, and biochemical factors [38], [39]. Chui *et al.* [40] used SPH to model the adhesion and the aggregation of clot particles and the mechanism governed by physical triggers (i.e. low shear stress). Al Saad *et al.* [41] idealised an SPH model to describe thrombus formation, where platelet adhesion and aggregation are obtained through elastic forces that depend exclusively on geometrical distances from an injured vessel.

This thesis describes a new SPH numerical method for the simulation of thrombus formation, where an innovative monolithic FSI approach is developed to describe the interaction between blood and the forming thrombus. The fluid-solid coupling is guaranteed thanks to the inclusion of elastic forces between solid particles which form by switching fluid particles when specific biochemical conditions are satisfied. Other novel aspects regard the parameters involved that is biochemical and hydrodynamics variables that give more realistic aspect to thrombus modelling.

[2] Eulerian methods discretize the space in which the material moves through the simulation elements, which are fixed in space. All Eulerian methods are mesh-based methods, for example the finite difference and finite volumes methods.

[3] Lagrangian methods discretize the material that is simulated, and the discretization moves during the simulations. Particle methods and SPH are examples of methods based on Lagrangian approach.

Chapter 3

3. Smoothed particle hydrodynamics (SPH): basic and formulation

Smoothed particle hydrodynamics (SPH) is a meshless method suitable for solving flow problems characterised by highly complex geometries or involving multiple phases and/or fluid interfaces. The method, which is based on Lagrangian dynamics, was first proposed to solve astrophysical problems in three-dimensional space. Later it was extended to compressible and incompressible flows in different fields such as bioengineering [42].

In this thesis, an existing open-source code has been further developed and specialised to some classes of fluid dynamic problems mainly related to thrombosis pathologies. The code, named PANORMUS (PArallel Numerical Open-souRce Model for Unsteady Flow Simulations) [43] was developed at the Department of Engineering of the University of Palermo (Italy). PANORMUS is distributed under the General Public Licence (GPL) and is available at http://www.panormus3d.org. The numerical model contains a Finite-Volume package, named PANORMUS-FVM and a fully incompressible smoothed particle hydrodynamics (SPH) solver, PANORMUS-SPH [43]. The equation solvers are written in FORTRAN 95 programming language while the Graphical User Interface is written in C++ and based on the multiplatform Qt R library (https://www.qt.io) [44].

SPH consists in discretising the computation domain with a set of particles, each defined by a mass, density, volume, and other characteristic physical properties. The particles, without a fixed connection, are arranged to simulate a continuous medium. A simulation based on the SPH method involves two main steps, *kernel approximation,* and *particle approximation*. The first step involves representing the function and its derivatives in a continuous form through integral representation. This representation is based on the evaluation of a smoothing function. In the second step, referred to as particle approximation, the computational domain is first discretised by representing the domain with an initial distribution of particles.

3.1 Kernel approximation

The continuous representation of a general function *f* at position vector **x** as a convolution integral extended over the domain D constitutes the *kernel approximation*

$$\langle f(\boldsymbol{x})\rangle = \int_D f(\boldsymbol{x}')\delta(\boldsymbol{x}-\boldsymbol{x}')d\boldsymbol{x}' \tag{3. 1}$$

where δ is the integral of δ in D equal to 1 if $\boldsymbol{x}=\boldsymbol{x}'$ and 0 elsewhere.Replacing the Dirac delta function with a weight function W($\boldsymbol{x}-\boldsymbol{x}', h$), the kernel approximation of *f* (indicated with the symbol$\langle f(\boldsymbol{x})\rangle$), the equation (3. 1) can be written as

$$\langle f(\boldsymbol{x_i})\rangle = \int_D f(\boldsymbol{x}')W(\boldsymbol{x}-\boldsymbol{x}', h)d\boldsymbol{x}' \tag{3. 2}$$

where the smoothing length, or *h*, is a characteristic length of the weight function W, also referred to as the *kernel function*. The smoothing length has a role analogous to the cell dimension for grid-based approaches and regulates the influence domain of the kernel function W while defining its support domain.

The primary requirements for the kernel functions are mentioned below:

Unity condition - integration of *W* over the whole domain *Ω* is equal to one:

$$\int_\Omega W(\boldsymbol{x}-\boldsymbol{x}', h)\, d\boldsymbol{x}' = 1 \tag{3. 3}$$

Compact support condition - The area of influence of *W*, named support domain, has a limited width equal to *kh*. It is, thus:

$$W(\boldsymbol{x}-\boldsymbol{x}', h) = 0 \text{ for } |\boldsymbol{x}-\boldsymbol{x}'| > kh \tag{3. 4}$$

Positivity condition - The function *W* is positive for each particle inside the support domain at *x*:

$$W(\boldsymbol{x}-\boldsymbol{x}', h) > 0 \ for |\boldsymbol{x}-\boldsymbol{x}'| \leq kh \tag{3. 5}$$

Monotonically decreasing behaviour - The value of *W* is monotonically decreasing with the increase of the distance $|\boldsymbol{x}-\boldsymbol{x}'|$

Symmetric condition - *W* is an even function and particles with the same distance, but different positions have equal effects on a given particle

$$\int_\Omega (\boldsymbol{x}-\boldsymbol{x}')W(\boldsymbol{x}-\boldsymbol{x}', h)\, d\boldsymbol{x}' = 0 \tag{3. 6}$$

3.2 Wendland function

Many different functions to describe Kernel approximation were proposed. Examples include the Gaussian model and the cubic spline representation. The following Wendland function has been used in this study, where the smoothing length h and the radius of the support domain are related by a constant k equal to 2.

$$W_{ij} = \frac{21}{16\pi h^3}\begin{cases}(1 - r_{ij}/2)^4(2r_{ij} + 1), when\ 0 \le r_{ij} < 2 \\ 0\ when\ r_{ij} \ge 2\end{cases} \quad (3.\ 7)$$

where r_{ij} is the ratio $|\boldsymbol{x_i} - \boldsymbol{x_j}|/h$. The function and its derivative trend are plotted in Figure 9.

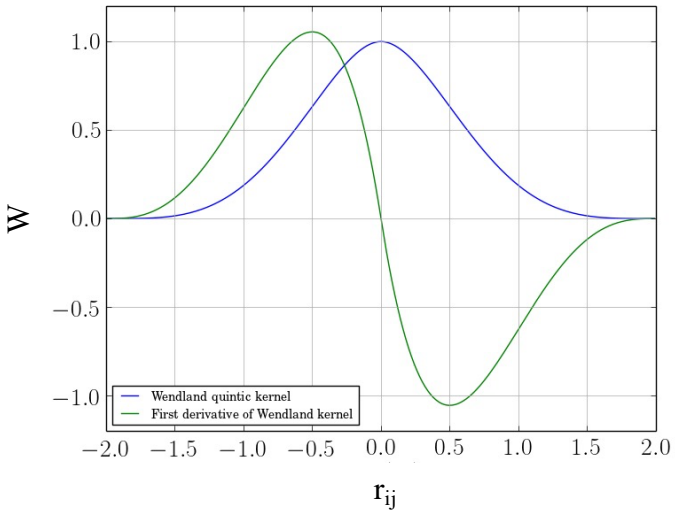

Figure 9 - Wendland function (blue line) and its derivative green line

3.3 Particle approximation

The particle approximation involves representing the problem domain using N_e particles, where the field variables are estimated. Figure 10 shows the support domain for a generic i particle, which comprises the particles in its immediate vicinity whose distance from its position (x_i) is less than the product of the characteristic width h of the kernel function and a constant k that depends on the kernel function's shape (see 3.2.).

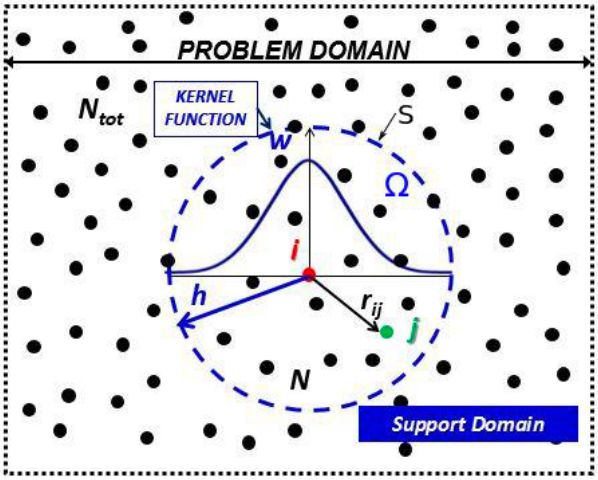

Figure 10 - Draft of the particle support domain. Continuous blue line: kernel function; red full cycle: particle i; empty dashed blue circle: support domain of i (Ω_i) (image taken from [44]

The integral of eqn (3. 2) calculated at the position $\boldsymbol{x}_i$ of the i particle can be substituted in a discretised form as the sum over the N particles lysing into the domain Ω_i

$$\langle f_i \rangle = \sum_{j=1}^{N} \frac{m_j}{\rho_j} f_j W_{ij} \tag{3. 8}$$

Where, for simplicity, $\langle f_i \rangle$ indicates $\langle f(\boldsymbol{x}_i \rangle$ and the weighting function $W(\boldsymbol{x}_i\text{-}\boldsymbol{x}_j, h)$ is written as W_{ij} because its value depends on the distance d_{ij} between the particle i and its surrounding particle j. In the equation, m_j and ρ_j are the mass and density of j, respectively.

3.4 Boundary conditions treatment

Differently from grid-based computational methods, where the implementation of Neumann, Dirichlet or mixed boundary conditions is generally simple thanks to the regularity of the domain, in the case of meshless methods, such as the SPH, imposing conditions on the outlines is more complex. In bioengineering applications, the aspect related to boundary conditions represents a particularly important feature of the problem. The most used approaches to impose boundary conditions in the SPH method are based on mirror particles. In particular, the approach based on mirror particles consists of the generation of a virtual particle for each fluid particle close to the boundary (as shown in Figure 11).

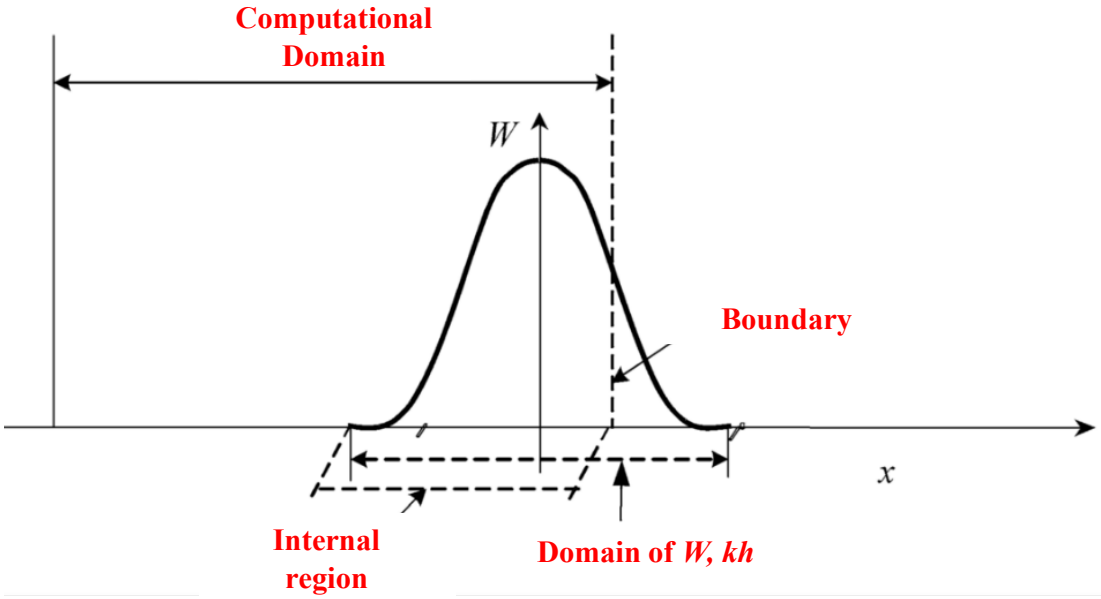

Figure 11 – Computational domain and boundaries in SPH

In PANORMUS-SPH mirror particles are employed at solid walls, while a peculiar procedure is used at inflow/outflow boundaries based on ghost particles. Mirror particles are generated in directions normal to the boundary by effective particles that are closer to the boundaries than *kh*. Each mirror particle shares the same physical characteristics as the generating effective particle, such as mass, density, viscosity, etc., while the velocity is selected to guarantee that the necessary boundary conditions are satisfied (adherence, free-slip, Neumann, wall-law, periodic, etc..). The boundaries of the computational domain in the PANORMUS-SPH model are discretised into triangles to make it easier to identify the normal direction and the distance particle-wall [45]. Triangle discretisation enables accurate descriptions of complex shapes and as they are planar, it makes also very simple to determine normal directions.

Before running the simulation, the boundary file must be created. This file contains the boundary conditions for each triangle such as corresponding nodes coordinates, triangle indices and conditions. The boundary file is read at the start of the simulation, and for each triangle the plane coefficients are computed. More details of the procedure used to identify the particles are given in [43], [44].

Thus, the procedure for mirror generation can be summarised as follows [44]:

1. The domain boundaries are discretised into triangles and a virtual grid[4] is created;
2. The cells of the virtual grid are classified into types 1, 2, 3, and 4 (and 5 and 6 for parallel computation);
3. Only the effective particles belonging to cells of type 2 and 3 are considered, since they can have a distance from the boundary shorter than kh;
4. The distance (d_S) between each particle S (identified at step 3, which lies thus in a cell of type 2 or 3) and each triangle intersected or close the cell of S ($cell_S$) is calculated. To this aim, the intersection at point $\boldsymbol{x_I}$ between the current triangle plane (named *nb*) and its normal line starting from S is identified. The variable d_S is thus obtained as the distance between S and the intersection point $\boldsymbol{x_I}$;
5. If $d_S < kh$ and the intersection point $\boldsymbol{x_I}$ is inside the triangle surface, one mirror particle S' is generated with coordinate: $\boldsymbol{x_{S'}} = 2\,\boldsymbol{x_I} - \boldsymbol{x_S}$.

3.5 Governing equations and numerical procedure

In SPH simulations of incompressible flows, two different approaches can be used: Weakly Compressible (WCSPH) and Truly Incompressible (ISPH).

In the WCSPH scheme, an equation of state is introduced to relate pressure to density. Instead, the fractional-step method can be used in the ISPH algorithm to solve the equations of motion and continuity. Continuity and momentum equations for incompressible flows, can be written as

$$\nabla \cdot \boldsymbol{u} = 0$$
$$\frac{D\boldsymbol{u}}{Dt} + \frac{1}{\rho}\nabla p - \nu\nabla^2\boldsymbol{u} - \boldsymbol{f}_i = 0 \qquad (3.9)$$

where $\boldsymbol{u}$ is the instantaneous velocity, $\boldsymbol{f}_i$ is the mass force per unit mass, p is the pressure, t is the time, ρ is the fluid density, and ν is the kinematic viscosity. In the context of ISPH [46] these equations are resolved using the projection approach [47],

[4] The virtual grid is used to simplify the mirroring procedure (precisely because only the particles found inside cells of type 2 and 3 are investigated) and the search for nearby particles (for the creation of the support domain, the distance between the particles j which are found in the cells adjacent to that of i).

which enforces incompressibility by requiring the resolution of the Pressure Poisson Equation (PPE). The momentum and continuity equations are solved using the fractional-step method in PANORMUS-SPH. There are three separate steps in the procedure: predictor step, PPE, and corrector step.

In the first step of the procedure, named predictor-step, the momentum equation is solved by removing the pressure gradient term, to obtain the intermediate velocity $\boldsymbol{u}^*$. In SPH approximation, this equation can be written as

$$\frac{\boldsymbol{u_i^*} - \boldsymbol{u_i^{(r)}}}{\Delta t} + \frac{3}{2} Diff_i^{(r)} - \frac{1}{2} Diff_i^{(r-1)} - f_i = 0 \tag{3. 10}$$

where Δt is the time step, the index r indicates the time instant *t*, $\boldsymbol{u_i^*}$ is the intermediate velocity of the *i* particle, $\boldsymbol{u_i^r}$ is the velocity at time r, and f_i is the mass force per unit mass acting on the *i* particle. In eqn. (3. 10), $Diff_i$ is the diffusive term that is calculated using the Adams–Bashforth scheme [48] to obtain a second-order accurate explicit approximation:

$$Diff_i = -\sum_{j=1}^{N_i} m_j (\nu_i + \nu_j) \frac{(\boldsymbol{x_i} - \boldsymbol{x_j}) \cdot \nabla W_{ij}}{d_{ij}^2} (\boldsymbol{u_i} - \boldsymbol{u_j}) \tag{3. 11}$$

where ∇W_{ij} is the gradient of the *kernel function* and d_{ij} is the distance between the *i* and *j* particles.

The PPE are then solved to obtain the corrective velocity:

$$\sum_{j=1}^{N_i} \frac{2\, m_j}{\rho_j} \frac{(\boldsymbol{x_i} - \boldsymbol{x_j}) \cdot \nabla W_{ij}}{d_{ij}^2} (\psi_i - \psi_j) = -\frac{1}{\Delta t} \sum_{j=1}^{N_i} \frac{m_j}{\rho_j} (\boldsymbol{u_i^*} - \boldsymbol{u_j^*}) \cdot \nabla W_{ij} \quad (Poisson) \tag{3. 12}$$

where ψ is the pseudo-pressure, which has the dimension of the kinematic pressure $\left(p/\varrho\right)$.

The updated velocity $u_i^{(r+1)}$ is finally obtained as

$$\boldsymbol{u_i^{(r+1)}} = \boldsymbol{u_i^*} - \Delta t \sum_{j=1}^{N_i} \frac{m_j}{\rho_j} (\psi_i - \psi_j) \nabla W_{ij} \tag{3. 13}$$

3.6 The PANORMUS-SPH code's architecture

The flow chart for the SPH procedure in the PANORMUS-SPH code is summarised in Figure 12. Three components of the code can be split and treated individually: initialise, initial conditions, and time marching.

- **INITIALISE**
  - STEP 1: The boundary triangles and the boundary conditions to be specified at each triangle are read from a file, as explained in section 3.4.
  - STEP 2: By locating the left-south-down corner of the virtual and deducting the distance *kh* (in all directions) from the border triangle with the vertex having the lowest coordinates, the virtual grid is constructed. We create and save a list of all the nearby particles that are closer to each effective particle than *kh*. The equations in the code can determine the number of virtual cubic cells in the three directions (n_x, n_y, and n_z). The virtual grid's cubic cells are then divided into kinds 1, 2, 3, and 4.

- **INITIAL CONDITIONS**
  - STEP 3: The code generates an initial particle distribution for the domain with a starting isotropic particle distance. If the simulation starts from developed conditions, the software can read the particle positions and their hydrodynamic variables from a file in vtk format. In contrast, these variables are set to zero if the simulation starts from the beginning. For each particle, the virtual cell is thus determined.
  - STEP 4: The mirror particles are generated following the procedure described above (see section 3.4).
  - STEP 5: This step is fundamental to defining the support domain of the effective particles. To do this, a list of all the nearby particles for each effective particle that are closer to it than *kh* is created and saved.

- **TIME MARCHING**
  - STEP 6: The fractional-step procedure starts from simulation time t_0 (that can be $t_0 = 0$ or $t_0 \neq 0$, if the simulation starts from rest or developed conditions, respectively).
  - STEP 7: The intermediate velocity is calculated for the effective particles through eqn 3.10. For the mirror particles u^*_n is calculated at the x_b position.

- STEP 8: For each effective particle, the PPE equation is solved through a system of equations 3.12.
- STEP 9: The corrected velocities $\boldsymbol{u_i^{k*1}}$ are calculated using equation 3.13.
- STEP 10: For each effective particle, the new position $\boldsymbol{x_i^{k*1}}$ is obtained.
- STEP 11: The "new" mirror particles are created, and the previous mirror ones are removed after updating the particle positions.
- STEP 12: Each effective particle's support domain is updated.
- STEP 13: To enhance the particle distribution, the effective particles are shifted away from d_{si} (determined using shifting procedure to improve particle distribution [46], [49]), and the hydrodynamics variables in the new position are modified.
- STEP 14: The mirror particles are created following the shifting process (again removing the previous mirror particles).
- STEP 15: The action of the step 12 is repeated.
- STEP 16: One-time step is added to the simulation's running time (t = t+dt). If the adaptive time step technique is activated, it must be determined whether the Courant[5] (*CFL*) limit constraint is satisfied or the time step needs to be changed (if $CFL < CFL_{min}$ or $CFL > CFL_{max}$).
- After the sixteenth action, the procedure is restarted with the predictor step (STEP 7).

[5] the minimum and maximum values of the Courant-Friedrichs-Lewy (CFL) stability condition are imposed and, at the end of each iteration, it is checked if $CFL_{min} < CFL < CFL_{max}$ During the simulation, the CFL_{min} and CFL_{max} have been set to 0:2 and 0:5, respectively.
The CFL number is calculated as $\bar{u}_{max}\Delta t/\Delta x$ where u_{max} is the maximum magnitude particle velocity in the whole domain and Δx is the starting particle distance. If the condition is not satisfied due to $CFL < CFL_{min}$ or $CFL > CFL_{max}$, the time step is modified (increasing or decreasing, respectively, its value).

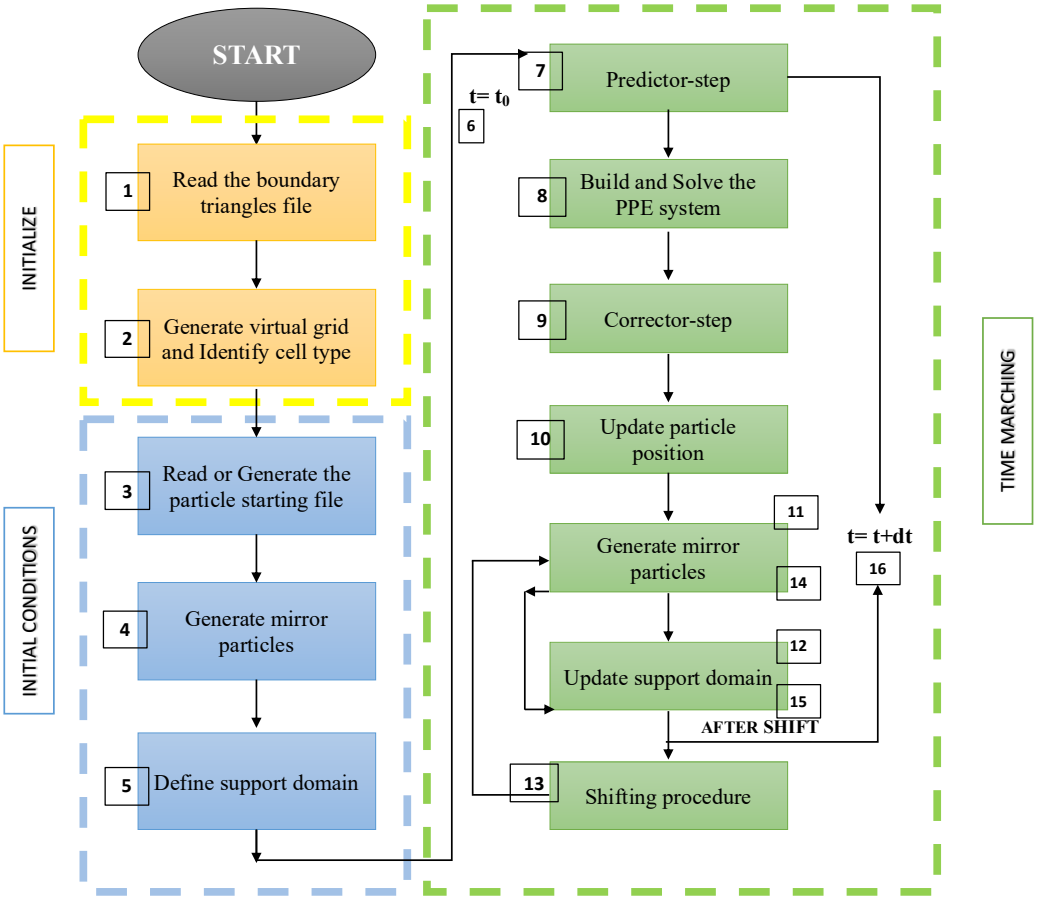

Figure 12 – Flowchart of PANORMUS code

Chapter 4

4. Thrombus formation model

The main aim of this chapter is to describe the thrombus model introduced in the PANORMUS code. In detail, the paragraphs below inserted will explain the step-by-step path for the final creation of the novel tool that can simulate thrombus formation, growth, and dissolution in a single solver. Initially, a brief description of the convection-diffusion equations of the species involved in the coagulation process is provided. Successively, an algorithm to simulate thrombus formation, growth, and dissolution is described, based on the biochemical evolution of the enzymes and platelet.

4.1 Biochemical species and platelets activation

The coagulative cascade takes a leading role in thrombus formation. As shown in Figure 13, many factors are involved in the process. In this study, four biochemical species were considered, to simplify and simulate clot formation: prothrombin (*pt*), thrombin (*th*), fibrinogen (*fg*) and fibrin (*fi*). In detail, they were chosen as the main factors of the coagulative cascade as described in section 2.4. These species, highlighted in red in Figure 13, come into play at the conclusive stage of the coagulative cascade, when the formed fibrin interacts with the activated platelets. The proposed model also includes three platelet states: resting platelets (*rp*), activated platelets (*ap*) and fibrin-bound aggregated platelets (*bp*).

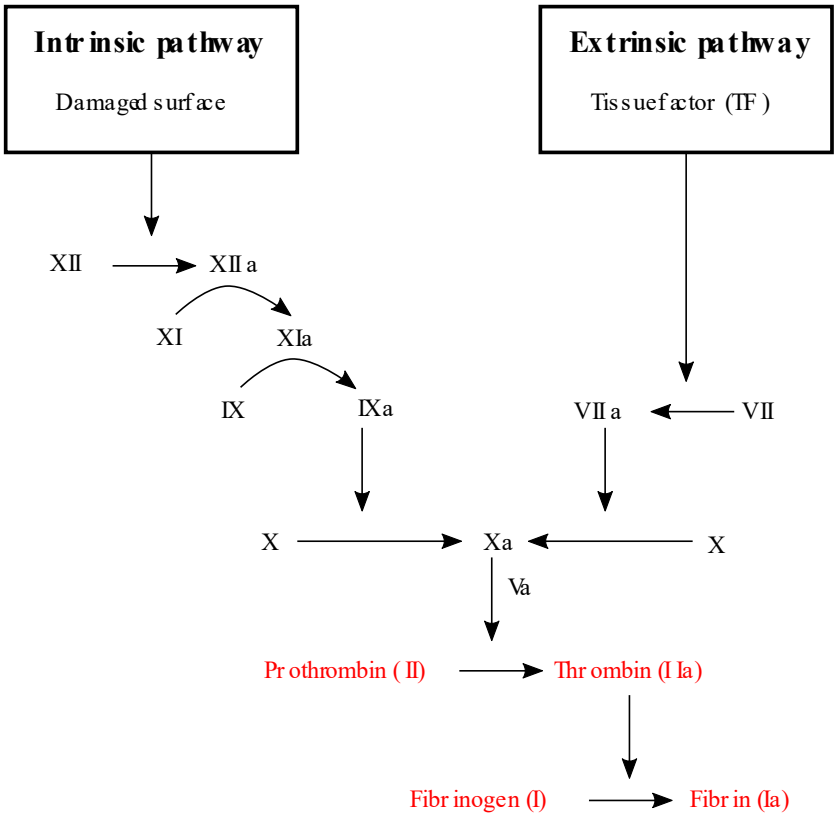

Figure 13 – Schematic view of the coagulative cascade (image taken from [50],p.6, fig.1)

The transport of the modelled species through the flow domain was evaluated by solving the convection-diffusion equation:

$$\frac{\Delta C_s}{\Delta t} - \alpha_s \nabla^2 C_s - S_s = 0 \tag{4. 1}$$

where C is the time dependent concentration of the generic specie ($s = pt, th, fg, fi, rp, ap, bp$), α_s and S_s are the diffusivity and the source term, respectively, and $\Delta C/\Delta t$ is the total derivative operator that, in the Lagrangian formulation, includes the convective term. In SPH, the concentration is associated with each mass point. Therefore, for the generic i particle the value of the concentration for the species s, $C_{i,s}$, can be calculated at the updated time step $(r+1)$ as

$$C_{i,s}^{(r+1)} - C_{i,s}^{(r)} - \alpha_s \left(\frac{3Diff_i^{(r)}}{2} - \frac{Diff_i^{(r-1)}}{2} \right) \Delta t + S_s \Delta t = 0 \tag{4. 2}$$

with the diffusive term $Diff_i$

$$Diff_i = -\sum_{j=1}^{N_i} m_j (v_i + v_j) \frac{(x_i - x_j) \cdot \nabla W_{ij}}{d_{ij}^2} (C_{i,s} - C_{j,s}) \tag{4. 3}$$

where $C_{j,s}$ is the concentration of s associated to the j particle lying in the support domain of i, and the other symbols are known.

The source terms for the modelled species are summerised below:

$$S_{th} = k_{th}^{rp}\, C_{rp}\, C_{pt} + k_{th}^{ap}\, C_{ap}\, C_{pt} \tag{4. 4}$$

$$S_{pt} = -S_{th} \tag{4. 5}$$

$$S_{fi} = \frac{k_{fi}^{th}\, C_{th}\, C_{fg}}{K_{m,fi}^{th} + C_{fg}} \tag{4. 6}$$

$$S_{fg} = -S_{fi} \tag{4. 7}$$

$$S_{ap} = k_{ap}\, C_{rp} - k_{bp}\, \phi_{pb}^{fi}\, C_{ap} \tag{4. 8}$$

$$S_{rp} = -k_{ap} C_{rp} \tag{4. 9}$$

$$S_{bp} = k_{bp}\, \phi_{pb}^{fi}\, C_{ap} \tag{4. 10}$$

The conversion of prothrombin to thrombin was assumed to occur on the surface of resting and activated platelets having kinetic constants k_{th}^{rp} and k_{th}^{ap}, respectively (see Table 2). According to Rosing [51], activated platelets support thrombin generation at a much higher rate than resting platelets, thus different values of kinetic constants were adopted for *rp* and *ap*. Thrombin promotes the conversion of fibrinogen to fibrin and the activation of resting platelets. The generation of fibrin promoted by thrombin was assumed to follow Michaelis-Menten kinetics [52] with kinetic constants k_{fi}^{th} and $K_{m,fi}^{th}$. For the activation of platelets, a function of local agonist concentrations was employed for the kinetic constant k_{ap}, as discussed in [20]. This function evaluates the impact of each single species on the rate of platelet activation and can be expressed as

$$k_{ap} = \begin{cases} 0, & \Omega < 1 \\ \dfrac{\Omega}{t_{act}}, & \Omega \geq 1 \end{cases} \tag{4. 11}$$

where t_{act} is the platelets activation time equal to 1 s [20]. The activation function Ω can be written as

$$\Omega = \sum_{s=1}^{N_s} w_s \frac{C_s}{C_s^*} \tag{4. 12}$$

Where w_s is the weight assigned to the agonist *s*, C_s is the concentration of the agonist *s*, and C_s^* is the threshold value for the concentration of *s*. In the proposed model, thrombin was considered as the only agonist species, as it typically contributes to most of the platelet activation phenomenon. Hence, eqn. 4.12 reduces to:

$$\Omega = w_{th}\,\frac{C_{th}}{C_{th}^{*}} \tag{4. 13}$$

where $w_{th} = 1$ and C_{th}^{*} is the threshold concentration for thrombin, that was set equal to $9.11 \cdot 10^{-10}$ M, according to Sorensen *et al.* [17] and Weiss [50] (see Table 2). Therefore, the conversion from resting to activated platelets is guaranteed when the concentration of the thrombin reaches the threshold value C_{th}^{*}. Activated platelets aggregate to the fibrin network to form bound platelets and, thus, the clot. Following [1], thrombin-induced fibrin generation and its effect on platelet trapping and aggregation is modelled using a second order Hill function ϕ_{pb}^{fi} that describes processes involving cooperative binding events [54]

$$\phi_{bp}^{fi} = \frac{C_{fi}^{2}}{C_{fi}^{2} + C_{fi,50}^{2}} \tag{4. 14}$$

where $C_{fi,50}$ is the half-saturation constant (concentration of fibrin where the half-maximal occupation occurs).

The constants and parameters used in the model are obtained from experimental studies available in the literature [15], [20], [53], [55]–[57]. These values are listed in Table 2 and are generic and applicable in different flow conditions.

Biochemical reactions kinetic constants			
Symbol	Value	UM	References
$\boldsymbol{k_{th}^{rp}}$	$6.50 \cdot 10^{-10}$	U PLT^{-1} s^{-1} μM^{-1}	[20]
$\boldsymbol{k_{th}^{ap}}$	$3.69 \cdot 10^{-10}$	U PLT^{-1} s^{-1} μM^{-1}	[20]
$\boldsymbol{K_{m,fi}^{th}}$	3160	nM	[55]
$\boldsymbol{k_{fi}^{th}}$	59	s^{-1}	[3]
$\boldsymbol{k_{pb}}$	$1 \cdot 10^{4}$	s^{-1}	[58]
$\boldsymbol{C_{th}^{*}}$	$9.11 \cdot 10^{-10}$	M	[4]
$\boldsymbol{C_{fi,50}}$	600	nM	[15]
Diffusion Coefficients			
$\boldsymbol{D_{th}}$	$6.47 \cdot 10^{-7}$	cm^2 s^{-1}	[55]
$\boldsymbol{D_{fi}}$	$2.47 \cdot 10^{-7}$	cm^2 s^{-1}	[3]
$\boldsymbol{D_{ap}}$	$2.50 \cdot 10^{-7}$	cm^2 s^{-1}	[58]
$\boldsymbol{D_{bp}}$	0	cm^2 s^{-1}	[15]
Biochemical Initial Concentrations			
$\boldsymbol{C_{pt}}$	1400	nM	[15]
$\boldsymbol{C_{fg}}$	7000	nM	[15]
$\boldsymbol{C_{rp}}$	$2 \cdot 10^{8}$	PLT ml^{-1}	[1]
$\boldsymbol{C_{ap}}$	$1 \cdot 10^{7}$	PLT ml^{-1}	[15]

Table 2 - Values of reactions kinetic, diffusive coefficients, and initial concentrations adopted in the model

4.1.1 Case test: Evolution of biochemical species in benchmark test

A cylindrical pipe with two different diameters D_1 = 7.5 mm, D_2 = 10 mm and length $L_1 = D_1$ and $L_2 = 3D_2$ was considered to analyse the transport of tracers. A parabolic velocity profile was imposed at the inlet with a mean velocity of 0.16 m/s (as shown in Figure 14.) No-slip boundary condition was set at the pipe solid walls, whilst zero pressure was imposed at the outlet.

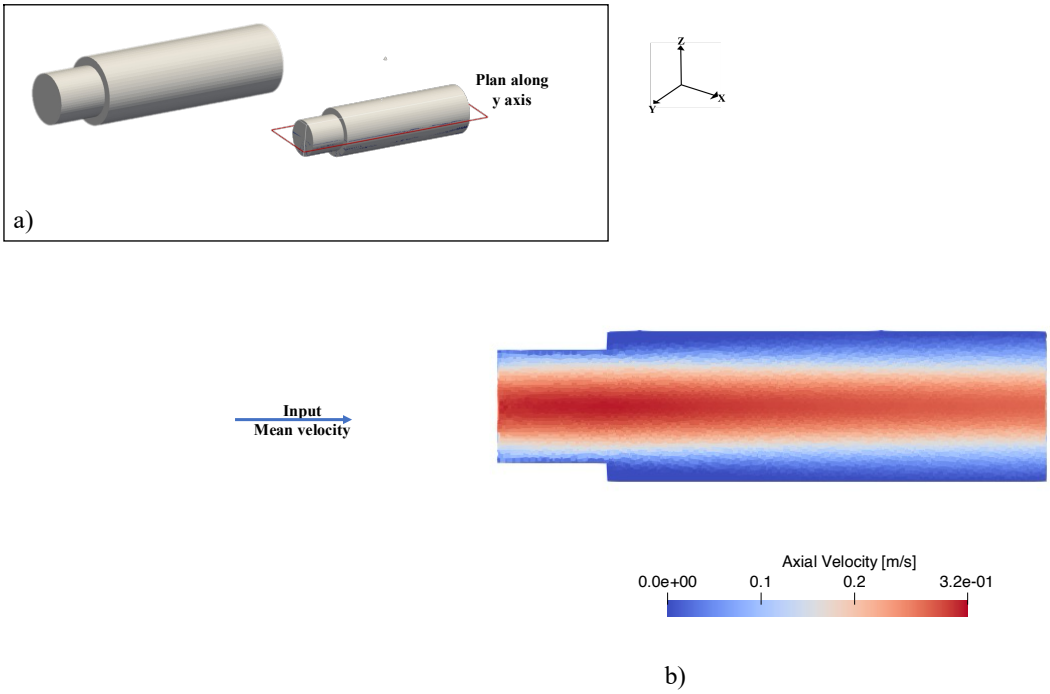

Figure 14 – a) Cylindrical pipe and y plan section used to represent results; b)Sketch of the fluid domain with input velocity

The initial particle distance was set to $\Delta x = 2.5 \cdot 10^{-4}$ m, so as to have 30 particles along the smaller pipe diameter; the resulting total number of particles was N_e = 173,800. To simulate the filling patterns, the whole domain was initialised with zero tracer concentration. Paraview software (https://www.paraview.org) was used to represent the results of the simulation.

Figure 15 shows the thrombin evolution in time. In particular, figure 16 represents half of the plan (along y axis) that has been considered for symmetry The evaluation of the species involved is essential to understand the process and to investigate possible anticoagulant therapy. Figure 16 analyses the temporal evolution in a selected point, with coordinates P (0.001;0.010;0.0035) of all biochemical species selected.

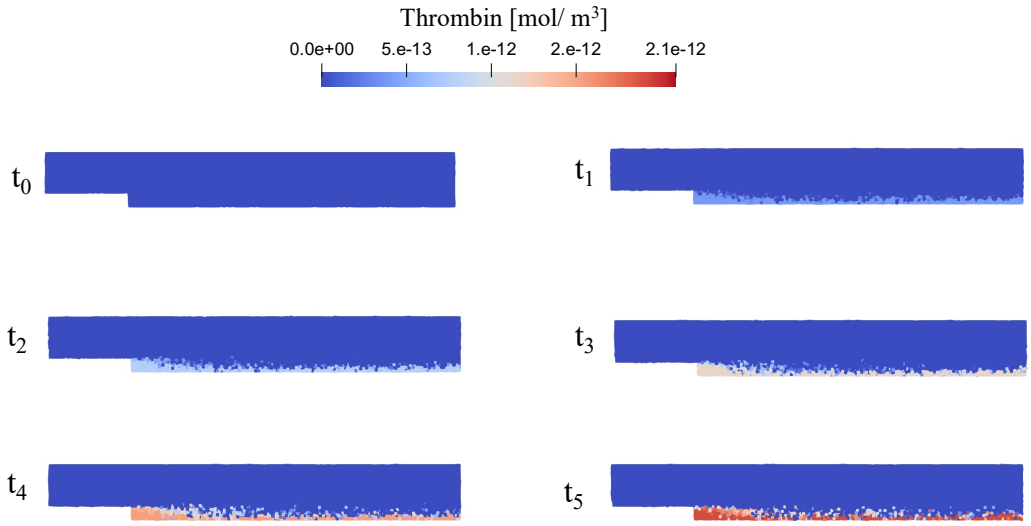

Figure 15 - Thrombin evolution considering six different time instants: t_0=0s, t_1=0.1s t_2=0.2s, t_3=0.3s, t_4=0.4s).

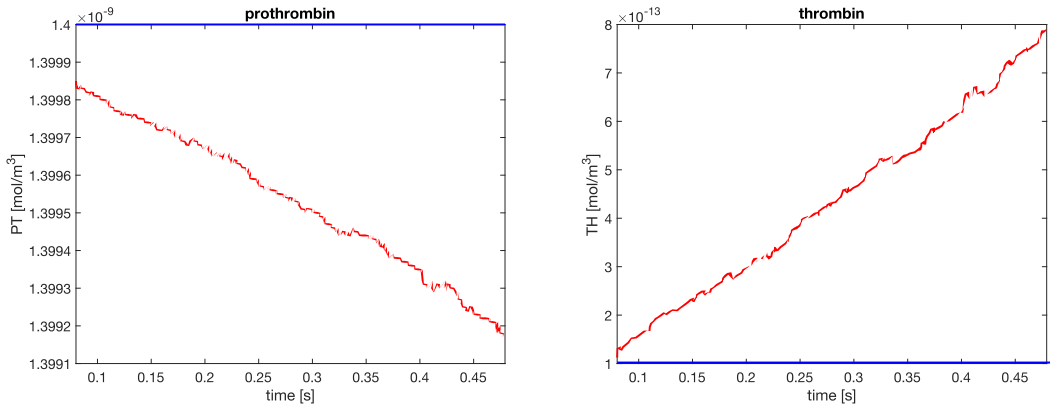

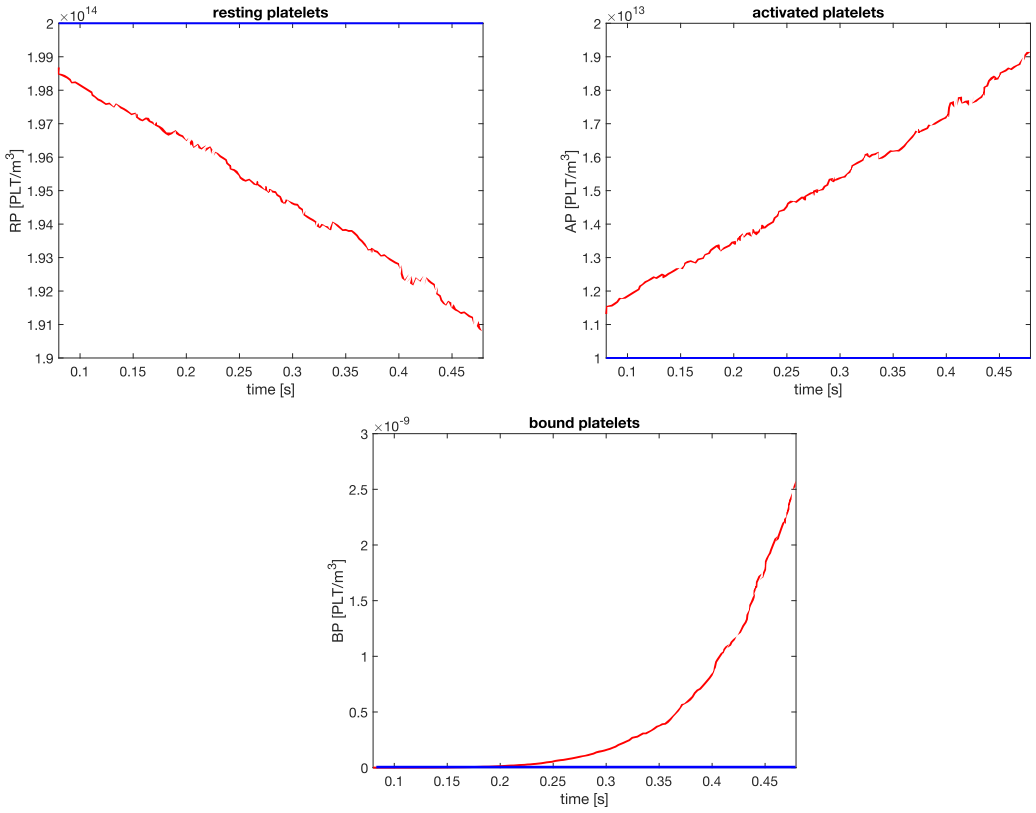

Figure 16 – Temporal trend of the modelled species involved in the coagulative cascade. Starting value: blue line; temporal consumption or growth: red line.

4.2 Trigger factor and boundary conditions

A trigger factor can be used as the start condition for thrombus formation. Since thrombin is considered to have the greater contribution to the coagulation process [59] (leading to platelet activation, fibrin mesh generation and bound platelets formation), the triggering is imposed as flux boundary conditions for thrombin concentration at the injured wall, that is a region of the vessel damaged that is characterised by the growth of enzymes that promote coagulation.

Figure 17 summarises, with a 2D sketch, the boundary conditions imposed for the modelled species at inflow/outflow boundaries and healthy and injured walls.

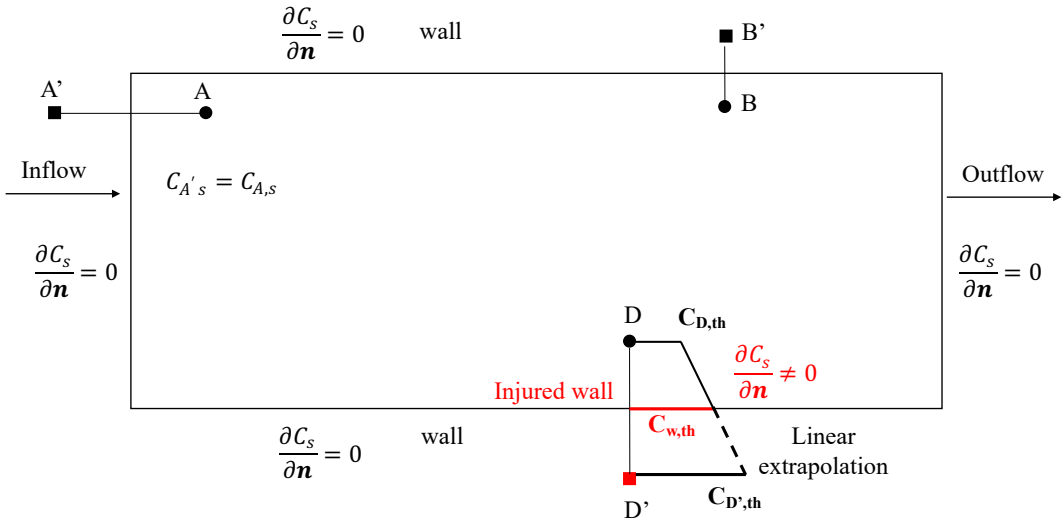

Figure 17 - Boundary conditions for the species involved in the coagulation cascade process. Circles: effective particle; squares: mirror particles; red bold line: injured wall (image taken from [50], p.9, fig.2)

Specifically, at the healthy vessel walls (including inflow/outflow boundaries), homogeneous Neumann conditions are imposed for the concentration of all the species $\frac{\partial C_s}{\partial n} = 0$, where n is the direction normal to the boundary (pointing towards the interior of the domain). This is achieved by imposing the concentrations of the mirror particle equal to that of the generating particle. In Figure 17 the concentration of mirror particle B' (black square), generated through the wall boundary, is equal to the concentration of the generating particle B (black circle). The same occurs for inflow and outflow boundaries (mirror particles A' and E', respectively). On the other hand, at the injured wall region (red bold line in Figure 17), a non-null value for the normal derivative of thrombin concentration is imposed. To this aim, the concentration of the D' mirror particle (red square) generated through the injured wall is obtained through a linear extrapolation based on the value of the generating particle D and the assigned concentration of thrombin at the injured wall, indicated as $C_{w,th}$

$$C_{D',th} = 2C_{w,th} - C_{D,th} \tag{4. 8}$$

4.3 Thrombus formation, growth and dissolution: a monolithic FSI solver

This section describes the implementation in PANORMUS of the two approaches allowing to simulate the primary thrombogenic processes. These encompass the aggregation of particles under hydrodynamic conditions as the increase in blood viscosity or elastic forces both driven by biochemical conditions. Based on the results of the first test cases, the model of thrombus formation, growth, and dissolution has been enriched by incorporating a close link between biochemical parameters and aggregation, more closely simulating natural processes. In particular, the biochemical species involved will be four: prothrombin, thrombin, fibrinogen, and fibrin. Three types of platelet particles will be distinguished: at rest, active and bound. The reactions will be described using convection-diffusion equations (see section 4.1). The definitive validation will be performed on Backward facing steps geometry presented in section 4.4.

4.3.1 First approach: Increase of dynamic viscosity

During the coagulation process, the blood undergoes change processes transforming itself from a liquid phase to a "gel-solid" state. These changes are evident in the variation of its viscosity value [60]. The viscosity is a physical quantity that defines the internal friction of a fluid and can be determined as the ratio between the shear stress and the velocity gradient between fluid layers or shear rate (SR). For Newtonian fluids, viscosity is independent of shear rate and is a constant value. Differently, blood is a non-Newtonian fluid; in fact, its viscosity is a function of the shear rate and depends on various other parameters such as the haematocrit or the concentration of fibrinogen. As previously mentioned, viscosity variation is a key rheological parameter for the prediction of thrombus formation (or growth). Initially, to simulate thrombus formation, it was introduced a novel tool that can convert "sample" fluid particles into "activated" particles representing a gel-solid state. The latter are particles which are found at a certain distance d_{ij} (less than a previously established threshold value) from the injured arterial/vascular wall and differ from other fluid particles by their viscosity value, which was increased 50-fold or 100-fold, as suggested in the literature [60], [61]. Figure 18 shows a sketch of the implemented model.

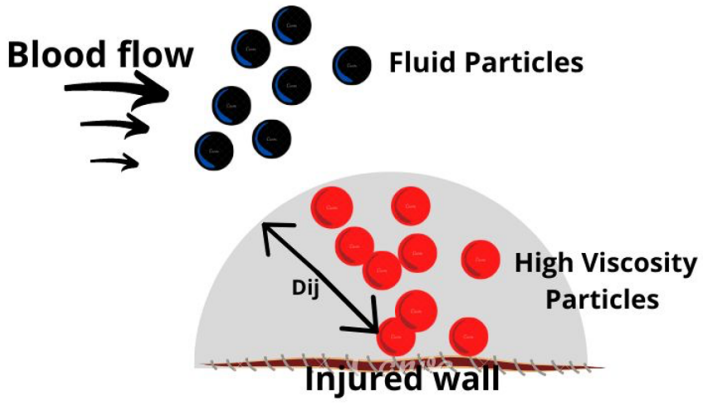

Figure 18 - Schematic model of the platelet activation process. Particles in black represent plasma, particles in red are activated platelets

A cylindrical pipe was used to analyse viscosity change during thrombus formation. The pipe has diameter D_1 equal to 0.025 m and length $L_1=2D_1$. The initial particle distance was set to $\Delta x = 1\times10^{-3}$ m, so as to have 25 particles along the pipe diameter, with a resulting total number of particles is $N_e = 196{,}800$. The viscosity of the activated particles was increased of 2 orders of magnitude. Therefore, the value of the kinematic viscosity varied between 3.3×10^{-6} and 3.3×10^{-4} m^2/s. The pressure gradient applied between the inlet and outlet sections was equal to 1.8 Pa, producing a velocity field between 0 and 0.4 m/s. No-slip boundary conditions were set at the lateral solid walls. The results obtained (Figure 20) show a decrease in the velocity values in the vicinity of the injured area, where the particles act as a highly viscous block which slows down the particles. The particles remain in this slower regime until the central flux drags them away from the injured region.

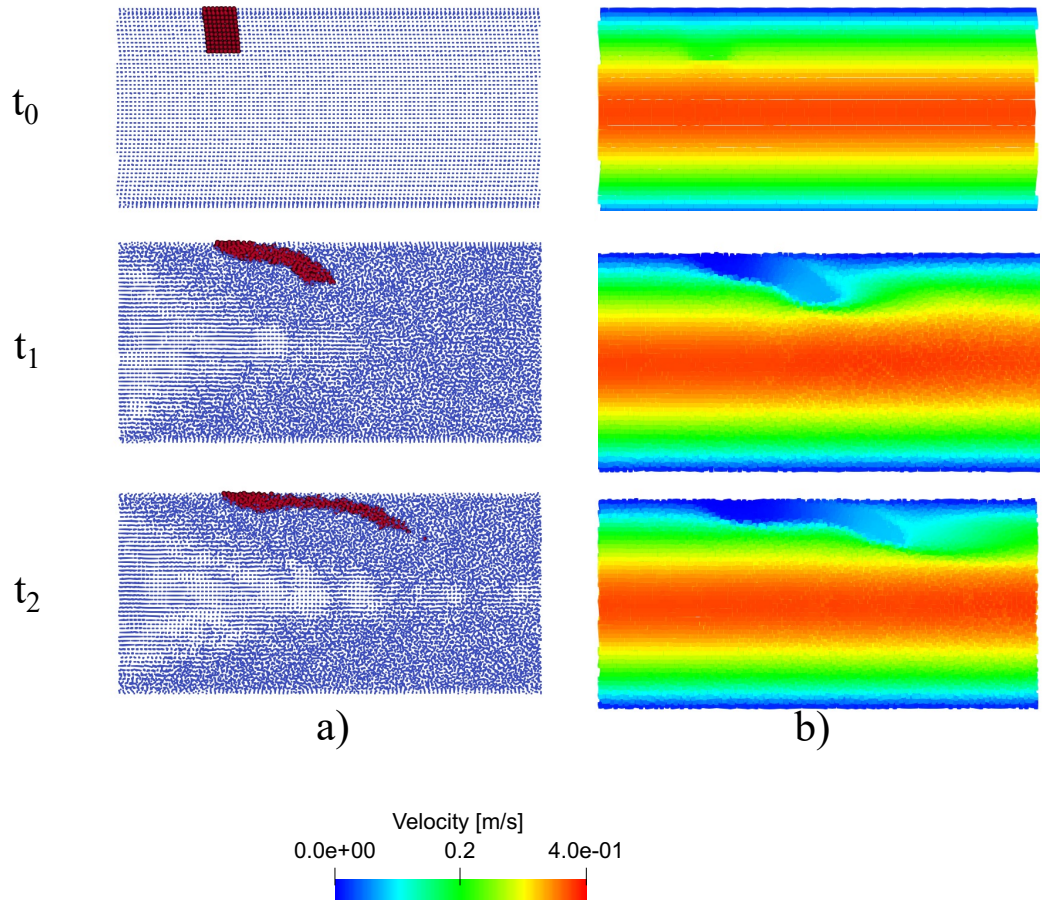

Figure 19 – a) Variation of active and aggregated particles over time (t_0=0 s;t_1=0.2 s;t_2=0.4 s). Red particles indicate activated fluid particles. b) Velocity field over time

4.3.2 Second approach: Introduction of elastic forces between particles

The endothelial injury exposes the subendothelial connective tissue causing platelets adhesion and their activation. The factors that are released from the platelet granules (ADP, TXA2, serotonin and others) recruit further platelets which aggregate above the first ones (aggregation phase). This platelet reaction occurs within minutes of the injury and constitutes the primary phase of thrombus formation. This process can be simulated using a system of forces acting between the activated particles [62], [63]. The platelet particles that are closer to the injured area than a distance d_{ij} (lower than the threshold value previously pre-set) are identified as active and a force $\boldsymbol{F_{ij}}$ begins to aggregate the particles, as shown in Figure 20.

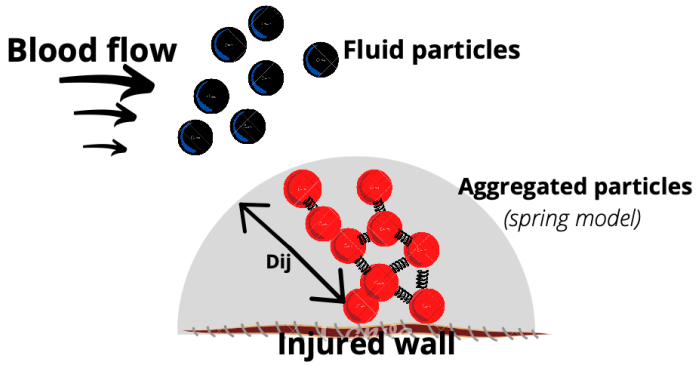

Figure 20 – Sketch of platelets aggregation phase

The aggregation force can be described as elastic forces (spring model), as described in eq. 4.15. The activation and subsequent aggregation is also considered for the particles in the neighbourhood of the activated ones:

$$\boldsymbol{F}_{ag} = \begin{cases} k_{ag}\left(l_0^{ag} - d_{ij}\right) \cdot \hat{\boldsymbol{ij}} & |d_{ij}| \leq d_{ag,threshold} \\ 0 & |d_{ij}| > d_{ag,threshold} \end{cases} \quad (4.15)$$

where k_{ag} is the spring constant expressed in [N/m], d_{ij} is the distance between the particles (variable in the various time steps), between the *i* and *j* particles, and l_0^{ag} is the natural length of the spring. The cylindrical pipe test (reported in section 4.3.1) was used to validate the spring model already described. For the activated particles the value of the elastic constant was equal to 0.005 N/m and based on experimental studies in the literature [41], [63]. The results present the aggregation of the particles by simulating the platelet activity for the formation of the primary thrombus. Figure 21 shows the position of the activated particle (red circles) at three time instants and the corresponding velocity field. As it can be observed, thanks to its meshless and Lagrangian nature, the SPH method lends itself very well to realistically capture the multiphysics interaction between blood flow and thrombi. The introduction of internal elastic forces between the particles has the major effect of creating stable bonds between the particles, causing a variation of the velocity field. The block of spring bonded particles represents a real obstacle for fluid particles, which deviate from their initial trajectory (as shown in Figure 22).

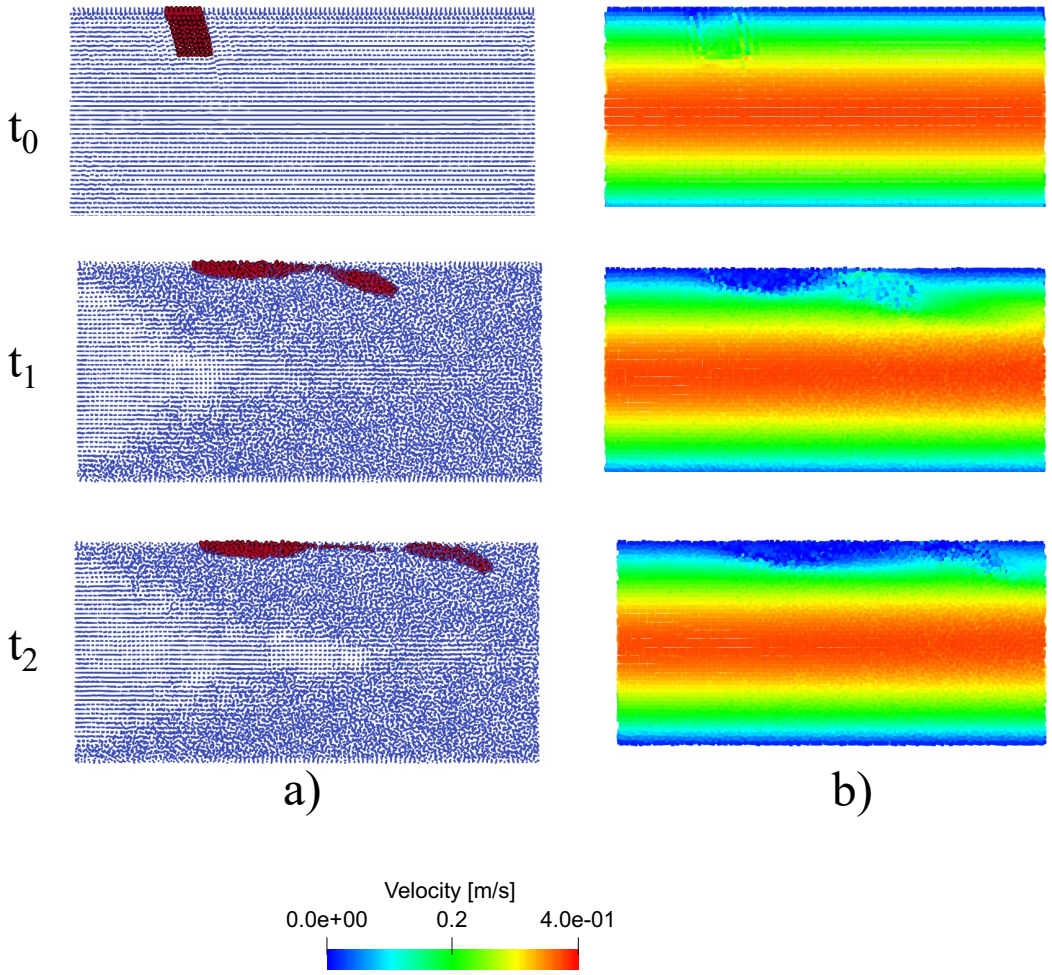

Figure 21 - Active and aggregated particles over time and influence on velocity field ($(t_0$=0.01 s;t_1=0.1 s;t_2=0.2 s)

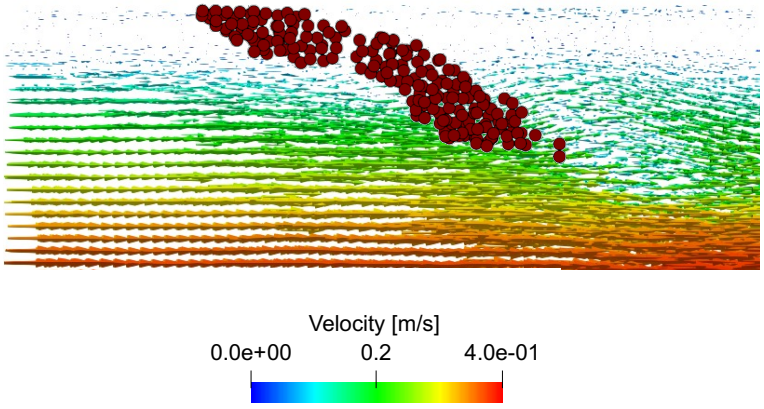

Figure 22 - Variations in velocity vector trajectories around activated particles

4.3.3 Thrombus formation model: particle agglomeration algorithm

As seen in previous sections, both the velocity variation and the spring model can be used to simulate particle aggregation (as seen in the first stage of hemostasis). Although the viscosity variation allows the simulation of a highly viscous gel, it was decided to extend the force model to include soft bonds, which better models what happens in nature or the interactions between fibrin ligaments and activated particles.

In the proposed model here discussed, the concentrations of *pt*, *th*, *fg*, *fi*, *rp*, *ap* and *bp* are evaluated at each particle through the convection-diffusion described by eqn. 4.1, with the source terms in eqn.s 4.4-10. Moreover, it was assumed that the concentrations of the species do not affect the blood velocity in normal conditions, in the absence of thrombus. On the other hand, a monolithic fluid-structure interaction approach is used when fluid blood particles convert to solid particles, mimicking the presence of thrombus.

The scheme represented in Figure 23 describes the proposed thrombus formation model. For a generic *i* particle, the concentration of thrombin $C_{i,th}$ is calculated solving the convection-diffusion eqn. 4.2 with source term from eqn. 4.4. Thrombin promotes the conversion of fibrinogen $C_{i,fg}$ into fibrin $C_{i,fi}$ through the source term of eqn. 4.6. Thrombin allows the conversion of resting platelets into activated platelets (eqn. 4.2 + source term in eqn. 4.8). Since the function Ω is greater than 1 (eqn. 4.12) and the kinetic constant k_{pa} in eqn. 4.11 is greater than 0, the activation of platelets begins when the concentration of thrombin $C_{i,th}$ exceeds the threshold value C_{th}^{*}. Activated platelets connected to the fibrin network generate bound platelets (eqn. 4.2 + source term of eqn. 4.10). Therefore, if the concentration of bound platelet $C_{i,bp}$ exceeds a set limit C_{bp}^{*} , the i fluid particle is switched to a solid particle by enforcing spring connections with the neighbouring solid particles. On the other hand, if $C_{i,bp}$ is below C_{bp}^{*}, i remains a fluid particle.

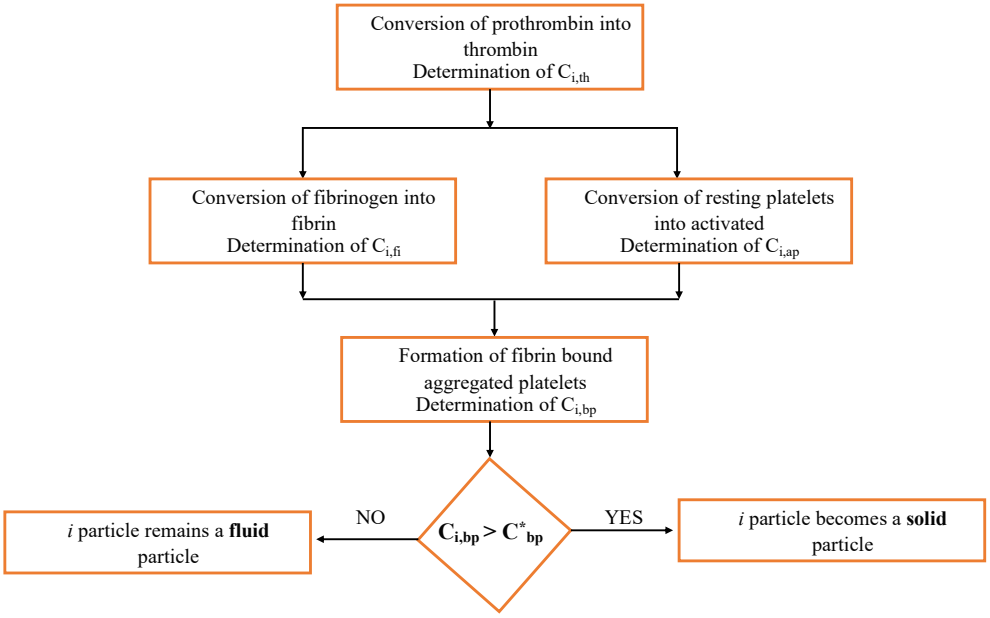

Figure 23: Schematic representation of the proposed thrombus model

In Figure 24a, which represents a snapshot at time instant r, all the represented particles have a concentration of bound platelets lower than the threshold value C_{bp}^{*}. These particles (represented as full black circles) are treated as fluid particle following the ISPH formulation described in section 3. At the $r + 1$ time step (see Figure 24b), the concentration of C_{bp} for particles A, B, C and E exceeds the threshold value. These particles, represented in figure as red full circles, are converted into solid particles by introducing internal elastic forces to simulate the solid behaviour. A procedure similar to that proposed by Monteleone *et al*. [64] was adopted here to obtain the elastic forces acting on the solid particles. However, instead of separating the fluid and solid domains through FSI-interfaces, in the proposed model particles are simply switched from fluid to solid phase by adding spring links without the need for the identification of the interface separating the two media. Specifically, when a fluid particle becomes a solid particle, it is linked to the neighbouring solid particles having a distance less than kh from it (particles lying in the dashed circle). In Figure 24b, the particle A is linked to B and C through springs, whilst E is not connected to A, being the distance between the two particles, d_{AE}, greater than kh.

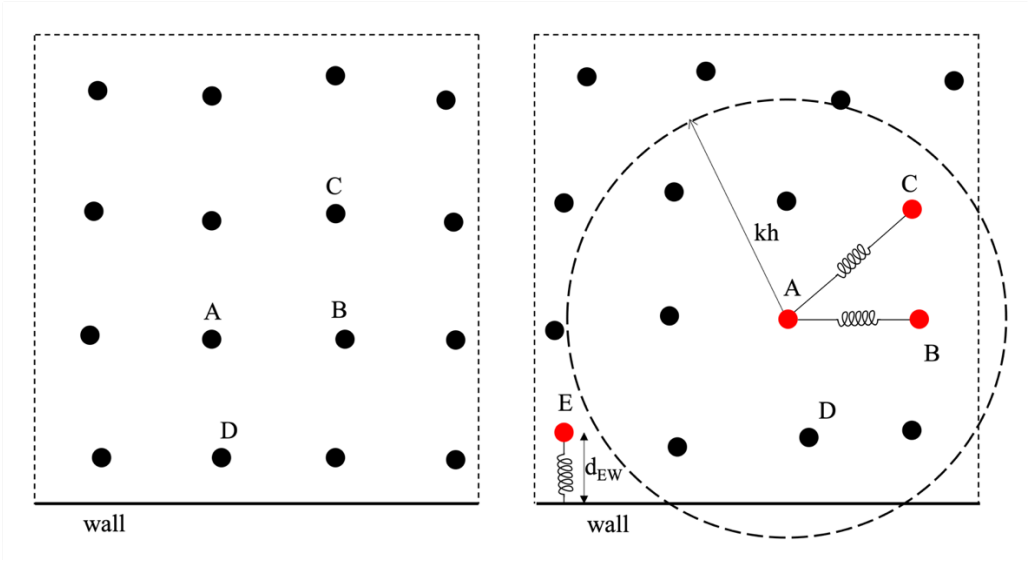

Figure 24: Sketch of the solid particle formation. Black full circles: fluid particles; red full circles: solid particle; bold black line: wall. a) Time instant r; b) time instant r+1 (image taken from [50], p.11, fig.4)

In principle, the links between solid particles were set not to change in time, so that the *i* solid particle maintains the same neighbouring *p* solid particles. Each pair of mass points *i-p* is connected via a spring having an elastic constant k_e and a rest length $l_{0,ip}$. In the model, the rest length of the spring is set equal to $l_{0,ip} = \Delta_x\sqrt{2}$ which is the average distance of the particles in the reference starting configuration. It was observed that this is the distance to which the particles tend in a general distribution, which is that existing when the thrombus starts to form. Therefore, it was verified that the use of this value gives a more stable solution, avoiding numerical instabilities. To reach and preserve the rest length, the springs respond by applying internal forces. Indicating with l_{ip} the instantaneous updated distances from the *i* solid particle to the neighbouring solid particles, the total internal force per unit mass acting on *i*, f_i, can be expressed as

$$\boldsymbol{f}_i = \frac{k_e\,\Delta_x}{m_i}\sum_{p=1}^{N_p}\left(l_{0,ip} - l_{ip}\right)\hat{\boldsymbol{x}}_{ip} \qquad (4.16)$$

where the summation is extended to the total number N_p of solid particles connected to *i* and $\hat{\boldsymbol{x}}_{\boldsymbol{ip}} = \left(\boldsymbol{x_i} - \boldsymbol{x_p}\right)/l_{ip}$ is the unit vector directed from *i* to *p*. The force $\boldsymbol{f}_i$ is introduced in the momentum equation as body force per unit mass. To handle the

elastic deformation of the thrombus, a relationship between the spring constant ke and the structure mechanical properties was obtained using a procedure similar to that employed by Monteleone *et al.* [64]. Specifically, a solid cube discretised with SPH particles bounded with springs is used to perform a tension stress analysis. In the test, several *ke* values were investigated and the Young's modulus *E* of the material was measured. As a result, a linear relationship between the spring coefficient and the Young's modulus was obtained, where *E/ke* = 6.31.

Moreover, the solid particles having distance to the boundary less than $\Delta_x/2$ are linked to the wall through a spring to model the adhesion of the thrombus to the vessel. In Figure 24b the solid particle *E* has a distance $d_{Ew} < \Delta_x/2$ and, therefore, it is connected to the wall.

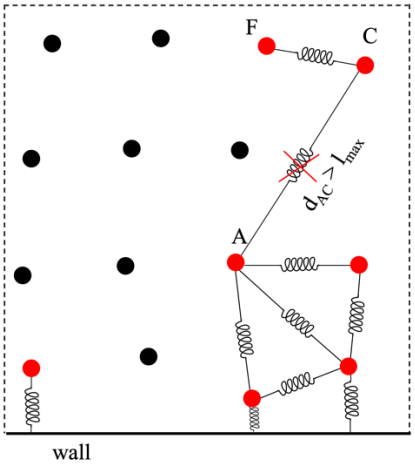

Figure 25: Sketch of the solid particle separation. Black full circles: fluid particles; red full circles: solid particle; bold black line: wall (image taken from [50], p.12, fig.5)

In this study, the potential thrombus dissolution is handled through a procedure similar to that proposed by Tosenberger *et al.* [65] to model platelets adhesion. In particular, once the spring forms, it can be stretched up to a threshold distance l_{max} (corrisponding to a treshold force), beyond which the link between the two particles is released. Therefore, single particles or group of particles linked together can separate from the main thrombus and embolise. In Figure 25 the length of the spring connecting the particles *A* and *C* becomes larger that l_{max} and is therefore removed, whilst the spring between *C* and *F*, although detached from the main thrombus (particles connected with *A* in the figure) can persist and can evolve into a second thrombus growing in dimensions, that can be carried by the flow.

A flow-chart describing the single steps of the proposed thrombus formation model is shown in Figure 26. The actions indicated in the flow chart are briefly explained in the following:

- ACTION 1: The source terms of the modelled species (*pt*, *th*, *fg*, *fi*, *rp*, *ap* and *bp*) to be introduced in the convection-diffusion equation are determined for each particle according to eqns. 4.4-4.10
- ACTION 2: The concentration of the modelled species is calculated for each particle through the convection-diffusion eqn. 4.2
- ACTION 3: For each solid particle, the total force resulting from the system of neighbouring springs is calculated through eqn. 4.17
- ACTION 4: In the predictor step, eqn. 3.10 is solved to calculate the intermediate velocity $\boldsymbol{u}^*$. For the solid particles, the force calculated at ACTION 3 is added to eqn. 3.10
- ACTION 5: The pseudo-pressure ψ is calculated solving the system made up of one PPE (eqn. 3.12) for each particle;
- ACTION 6: In the corrector step, the intermediate velocities are corrected obtaining the updated velocities (eqn. 3.13);
- ACTION 7: The particle positions are updated;
- ACTION 8: The mirror particles are generated and the boundary conditions for the modelled species are imposed, as discussed in section 4.2;
- ACTION 9: The support domain of each particle is determined including all the surrounding particles with distance lower than *kh*;
- ACTION 10: The solid particles are identified. Specifically, for each fluid particle, it is checked if the concentration of bound platelets exceeds the imposed threshold value. If this condition occurs, the particle becomes solid and its list of neighbouring solid particles is created. Moreover, for each solid particle, the list of the springs is updated during the simulation to be included new neighbours solid particles or to be excluded others that have exceeded the imposed threshold for the distance (l_{max}). The last condition is used to consider the possible thrombus dissolution.
- ACTION 11: The solid particles to be anchored to the wall are checked. To this aim, the distance from the wall is determined and if it is less than $\Delta_x/2$, a bond with the wall is created.

The simulation time is advanced by one-time step ($t = t+dt$), after the eleventh action, the procedure is restarted with ACTION 1.

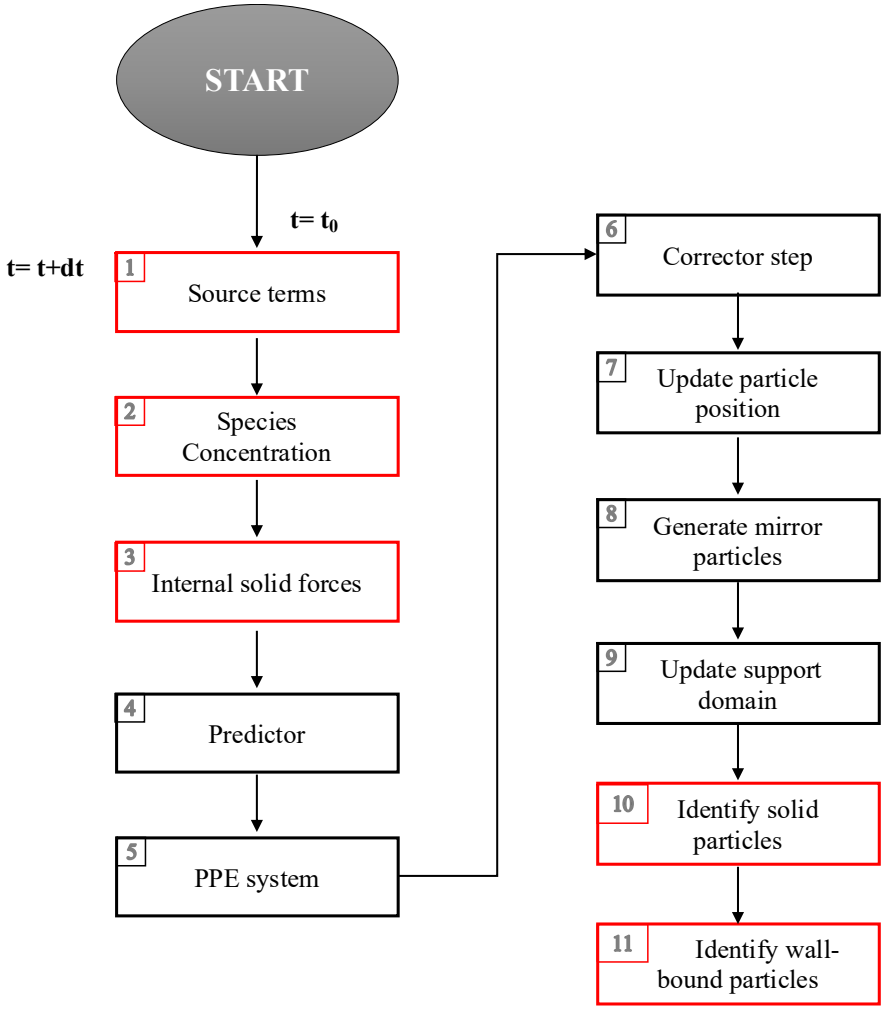

Figure 26: Flowchart of the proposed thrombus formation model (red text box)

4.4 Benchmark test to validation: thrombus formation in backward-facing step

To validate the proposed thrombus model described in the previous paragraph, the case study proposed by Taylor *et al.* [66] was replicated, where the thrombus growth was analysed in a Backward-facing step (BFS). BFS configurations are often employed to analyse phenomena where the presence of flow separation and reattachment regions is a leading factor [60]. These geometries are easy to adapt to different engineering problems, thanks to the direct control of the fluid domain by parameters such as the Reynolds number and the geometrical dimensions of the channel and step. The BFS geometry and dimensions selected by Taylor *et al.* [41] are represented in Figure 27.

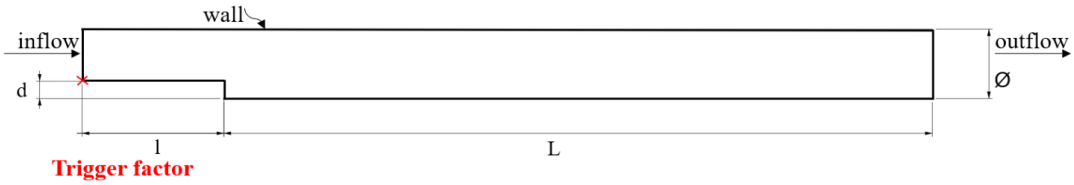

Figure 27 - Boundary Conditions imposed; Geometry and dimension: d=2.5 mm; Ø=10 mm; l=20 mm; L=100 mm, (image taken from [50], p.14, fig.7)

In the simulation, the kernel width was set to 0.7 mm, resulting in a total of 215,000 particles. A flow rate of 0.76 l/min was imposed at the inlet section, whilst zero pressure was set at the outflow section (see Figure 27). In this study, the procedure described by Monteleone *et al.* [67] is used to handle open boundaries. This ensures mass conservation through the introduction of new particles in the computational domain, through the inflow section, balancing the particles which leave it through the outlet. Blood was modelled as a Newtonian fluid (the shear-thinning behaviour and yielding were neglected), with density and dynamic viscosity equal to 1,060 kg/m^3 and 0.0035Pa s, respectively. The resulting Reynolds number was equal to 460, well within the laminar flow regimen.

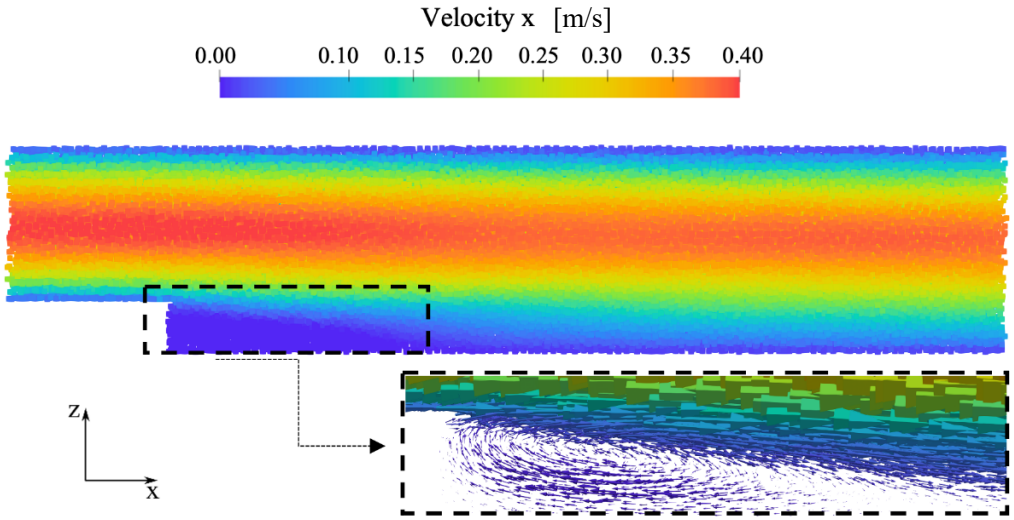

Figure 28 - Streamwise particle velocity [m/s] in BFS without thrombus. An enlargement of the region near the step is highlighted with the velocity vectors (image taken from [50],p.15, fig.8)

In the numerical analysis, the parallel scheme of Monteleone *et al.* [68] was employed to save computational costs.

A preliminary hydrodynamic analysis was performed on the steady-state simulation without a thrombus model (see Figure 28) to identify the recirculation region, obtaining a reattachment length equal to 17 mm, about 6.8 times the step height, consistent with Taylor *et al* [66].

As previously described, the formation of blood clots is regulated by a complex cascade of biochemical reactions taking place on the surface of a growing thrombus. The transport of enzymes in the coagulation is reported to be dominated by convection phenomena in the bulk, whilst becomes diffusion-dominated in the zones characterised by low velocities [23]. Flow can both promote and limit thrombin generation and thrombus formation, and this behaviour makes its prediction a challenging task.

Recent investigations by Kamada *et al*. [59],[60] have indicated that thrombin generation is modified by variations in shear strain rate (SSR) and, in particular, its presence reduces where SSR is high. Due to the multi-scale nature of the problem, some strategies were used to speed up the computation. In the presented model, the SSR parameter was selected to amplify the different behaviour between bulk regions and low-velocity zones. Specifically, as described in section 4.2, since thrombin is selected as a trigger factor, an amplification value equal to 10^5 was employed for the diffusive coefficient and source term of thrombin. Moreover, this coefficient was related to the SSR by applying it to particles having SSR lower that an imposed threshold value. Due to the accelerated conversion of thrombin, a continuous supply of the inactive biochemicals (*pt* and *fg*) and resting platelets was imposed.

The concentrations of the modelled species were initialised in the bulk through a steady-state simulation imposing the typical values in healthy human blood (as reported in Table 2) except for the concentrations of thrombin, fibrin and bound platelet, which were set to zero. Moreover, an initial concentration of activated platelets was considered to simulate primary hemostasis. This value is equal to 5% of the background concentration of resting platelets [15].

The biochemical reaction kinetic constants and the threshold value for the thrombin used in the simulation are reported in Table 2. A Young's modulus equal to 200 Pa (defined through the linear relationship between the Young's modulus and the spring constant *ke* described in section 4.3.3) was used in the analysis to simulate the early stage of the thrombus formation.

In this study, the threshold distance l_{max} considered for the springs dissolution (as discussed in section 4.3.3, this was set equal to 1.1 *kh*, as this value was found to

lead to improved numerical stability and better correlation with experimental findings [41]).

Given that physically the thrombosis process is a phenomenon that develops over a large period of time (days if not months), for the numerical modelling it was necessary to apply techniques to speed up the simulation and reduce the computational burdens. The key factor (trigger) controlling the phenomenon is thrombin, therefore it was decided to amplify the diffusion of thrombin with a numerical coefficient, linking the diffusion phenomenon to a threshold shear strain rate (SSR) value.

To identify the optimal values, a calibration/optimisation of the model was carried out by performing different numerical simulations adopting different variable parameters:

- four different SSR thresholds equal to 40-30–20-10 s^{-1} adopting the same amplification coefficient (named Φ);
- four different values of Φ setting the threshold SSR = 20 s^{-1}

A qualitative analysis was performed to evaluate the best match value of the SSR threshold and Φ. Figures 30 and 31 illustrate a comparison of the shape taken by the simulated thrombus considering different values. As it can be observed, using an SSR threshold equal to 10 s^{-1} (as recommended by Menichini and Xu [23]) and an amplification factor equal to 10^5, the thrombus front is about triangular, with shape and dimensions that well resemble the experimental results described by Taylor *et al* [66] (see Fig 32b).

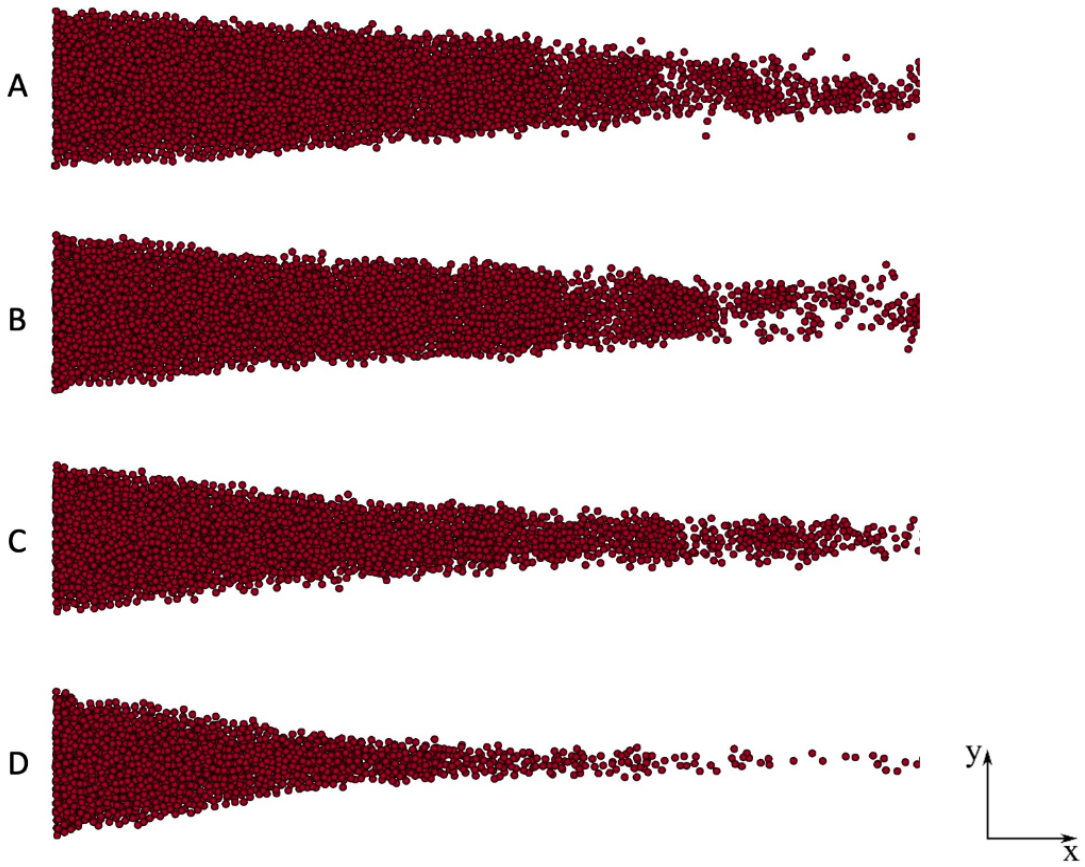

Figure 29 - Numerical results of thrombi formed (final time) considering various SSR thresholds. A) 40 s^{-1}; B) 30 s^{-1}; C) 20 s^{-1}; D) 10 s^{-1} (image taken from [50],,p.16, fig.9)

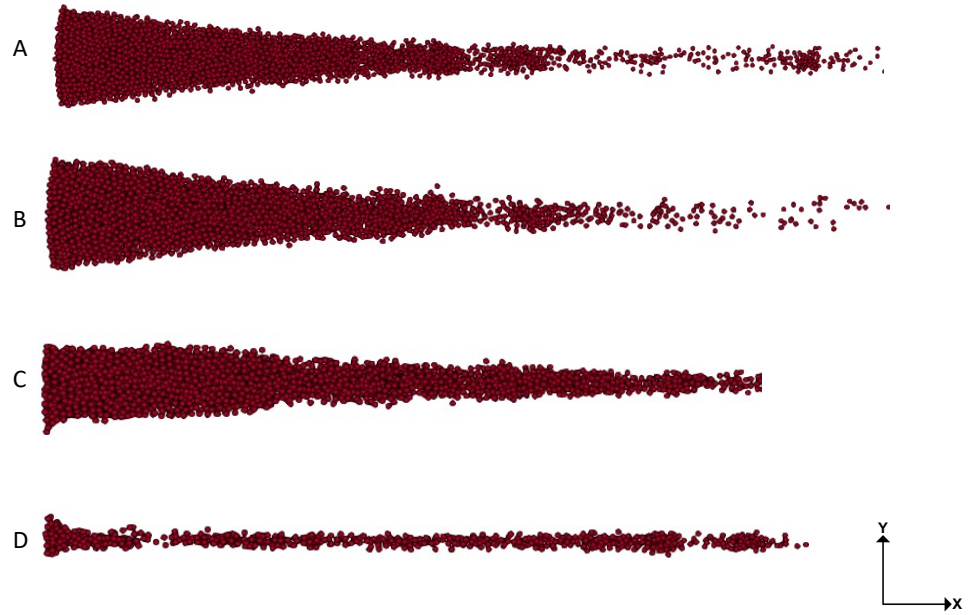

Figure 30 - Numerical results of thrombi formed (final time) considering various Φ. A) 10^6; B) 10^5; C) 10^4; D) 10^3

The trigger factor condition was imposed at the middle point of the step corner, as indicated in Figure 27, with a concentration of thrombin at the injured wall equal to the threshold value for thrombin amplified with the factor specified above ($C_{w,th}$=10^5 C_{th}*).

The temporal evolution of the thrombus, in terms of formation and growth, is represented in Figure 31. The thrombus formation increases in both the radial and axial directions. Initially, the thrombus height reaches the step height (2.5 mm), while the maximum thrombus length achieved is equal to ten times the step height (25 mm). This is in agreement with the experimental results observed by Taylor *et al* [66].

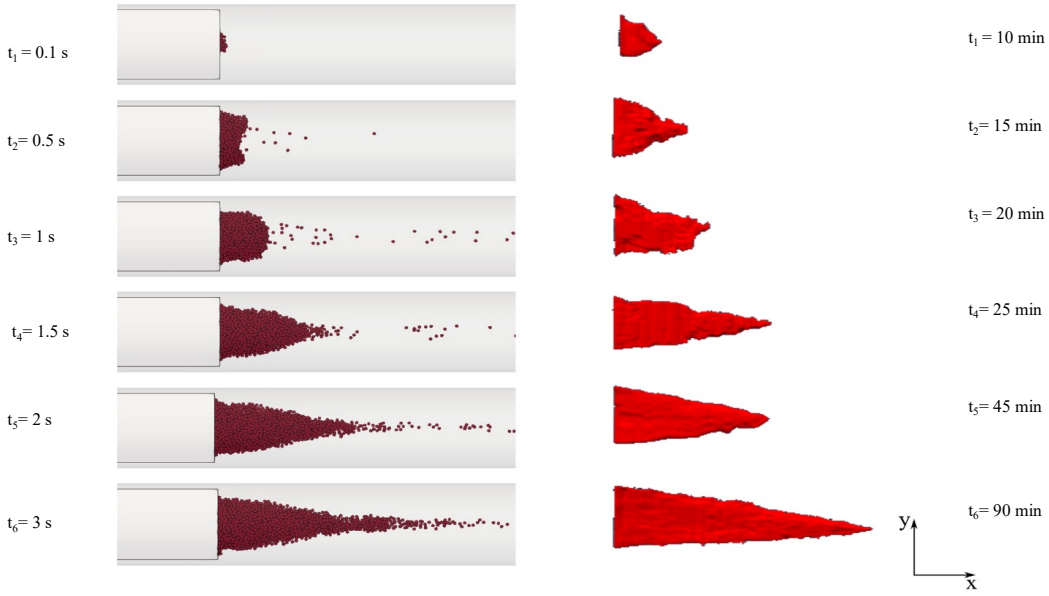

a) *b)*

Figure 31 - Thrombus growth within the BFS. a) Numerical results of FSI monolithic approach; b) Experimental results of [66]shown for comparison. Adapted from Taylor et al. [66] Copyright © 2014 ASME (image taken from [50], p.17 fig.10)

To assess the robustness and efficiency of the FSI monolithic method, the velocity field near the thrombus was examined. As shown in Figure 32, the thrombus growth is totally enclosed within the initial recirculation region, which eventually becomes entirely occupied by blood clotting.

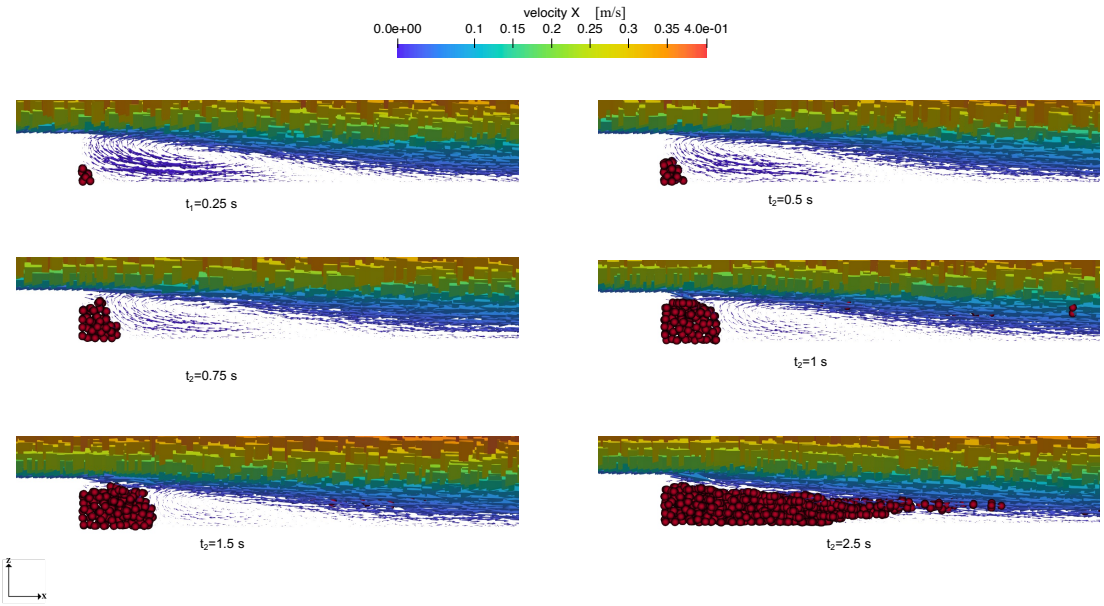

Figure 32 - Effect of thrombus formation on the velocity field in the vicinity of the step (image taken from [50], p. 18, fig.11).

The velocity profile at a cross-section positioned at an axial distal distance from the step equal to 8 mm, is plotted in Figure 33 at three-time instants. The diagrams show the temporal decrease of velocity as the thrombus propagates and approaches the cross-section, as described in Figure 32.

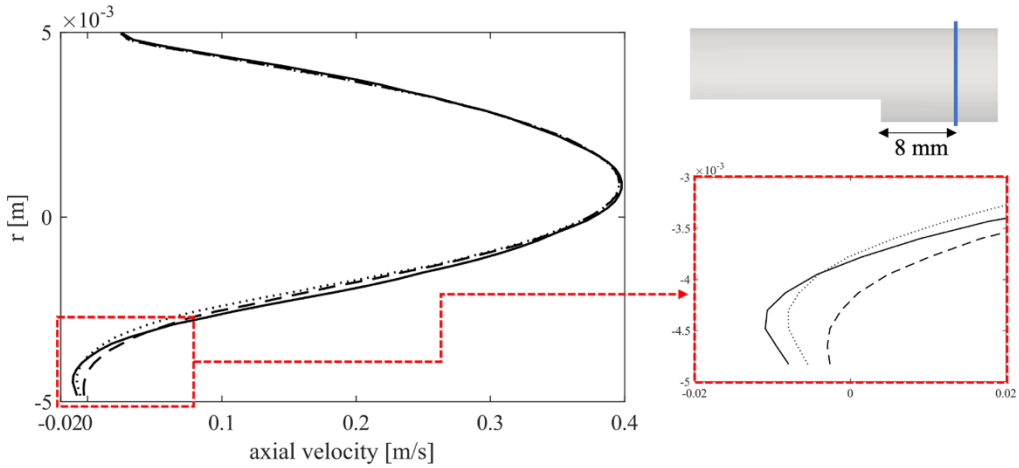

Figure 33- Axial velocity profile at three-time instants with a zoom of the region close to the step. Continuous line: velocity at time zero; dotted line: time 0.5 s; dashed line: time 1 s(image taken from [50], p.18, fig.12).

This confirms the mutual interaction between hydrodynamic variables and blood clotting. Furthermore, the observed thrombus length reaches an asymptotic value that relates to the reattachment length of the initial recirculation region. It should

be noted that, exceeding this asymptotic length, as the clot increases downstream the step it is dragged due to a high-velocity field. Therefore, although particles reach the conditions at which they can become solid, they cannot bind to the main thrombus, which maintains its size. The thrombus lysis is simulated using only maximum distances (as discussed in section 3.3). Correlation with the maximum fibrin concentration might reproduce the process more realistically and may be incorporated into the code in a future iteration.

An analysis of the species concentration is shown in

Figure 34. Considering three-time instants (indicated as t_1, t_2 and t_3 in the figure), the modelled active biochemical species (thrombin and fibrin) and platelets are triggered starting from the step position (see Figure 27) and spread downstream the channel.

The time evolution for the concentrations of the considered clotting factors was analysed at five different points in the recirculation region. These points are indicated in Figure 35. Points are positioned in the plane of symmetry, evenly spaced with a space equal to d (where d is the step height), with the first point *i* located at a distance equal to $d/2$ from the step. The concentrations are calculated by averaging the values of particles lying at distance less than kh from the considered central point. The graphs in Figure 36 show that all concentrations increase gradually until they reach an asymptotic value. Thrombin (Fig 37a) starts from a high value at point *i* as a consequence of the trigger factor imposed at the step, whilst the other points (*ii* to *v*) have an initial null value. A similar trend is highlighted in Fig 37b for fibrin evolution. Activated platelets (Fig 37c) have an initial value equal to 10^{13} PLT/m^3, which steeply increases after about 0.5 s at points *ii* to *v*, as the activation function becomes greater than 1. Since bound platelets depend on the activated platelets and fibrin mesh concentrations, their concentration follows the same development as in Fig 37d. The concentration analysis of the coagulative players of the thrombus formation process could be a helpful tool to individuate the regions involved by major risk-stopping the main trigger factors.

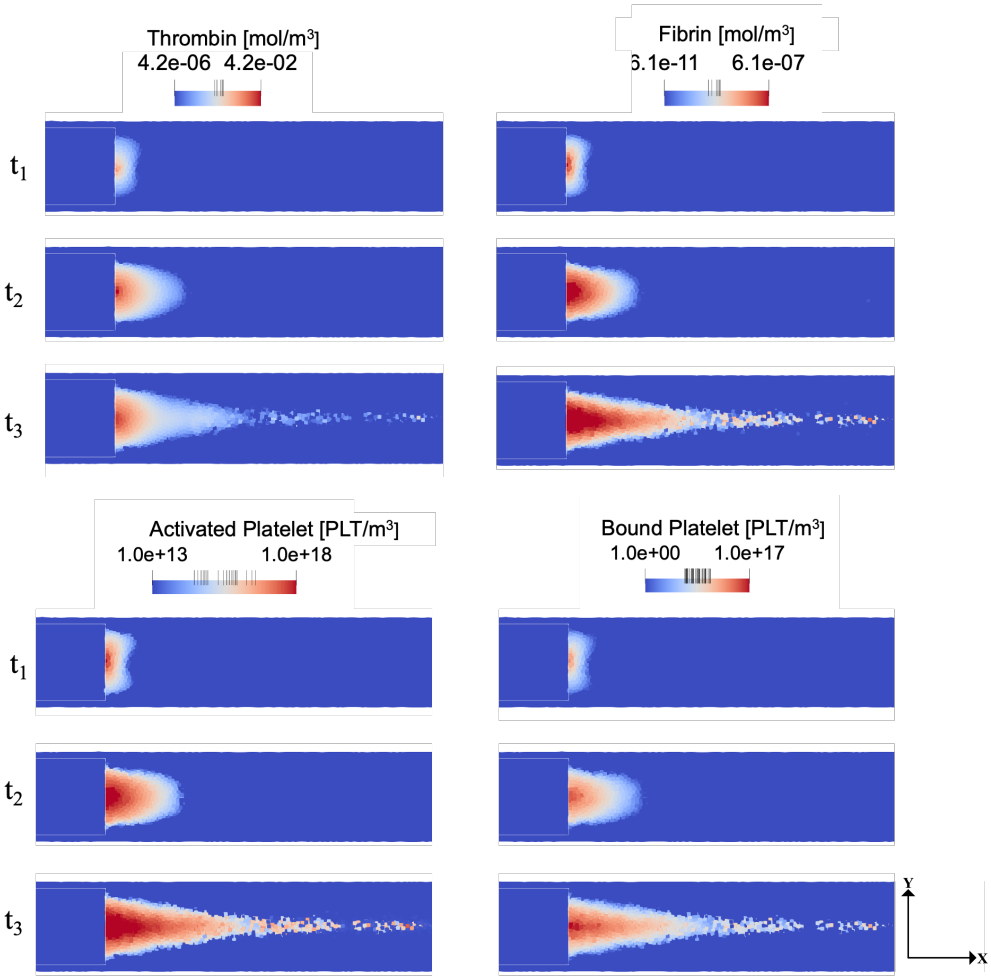

Figure 34 - Biochemical specie concentration map (logarithmic scale) at three time instants: t_1=0.5 s; t_2=1.5 s; t_3=3 s (image taken from [50], p.19, fig.13)

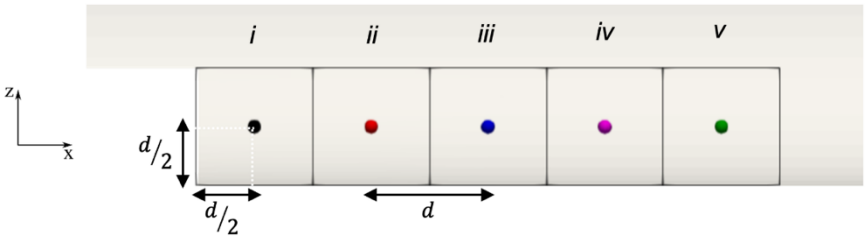

Figure 35 - Location of the measurement points used to evaluate the mean concentration of each specie (image taken from [50],p.19, fig.14)

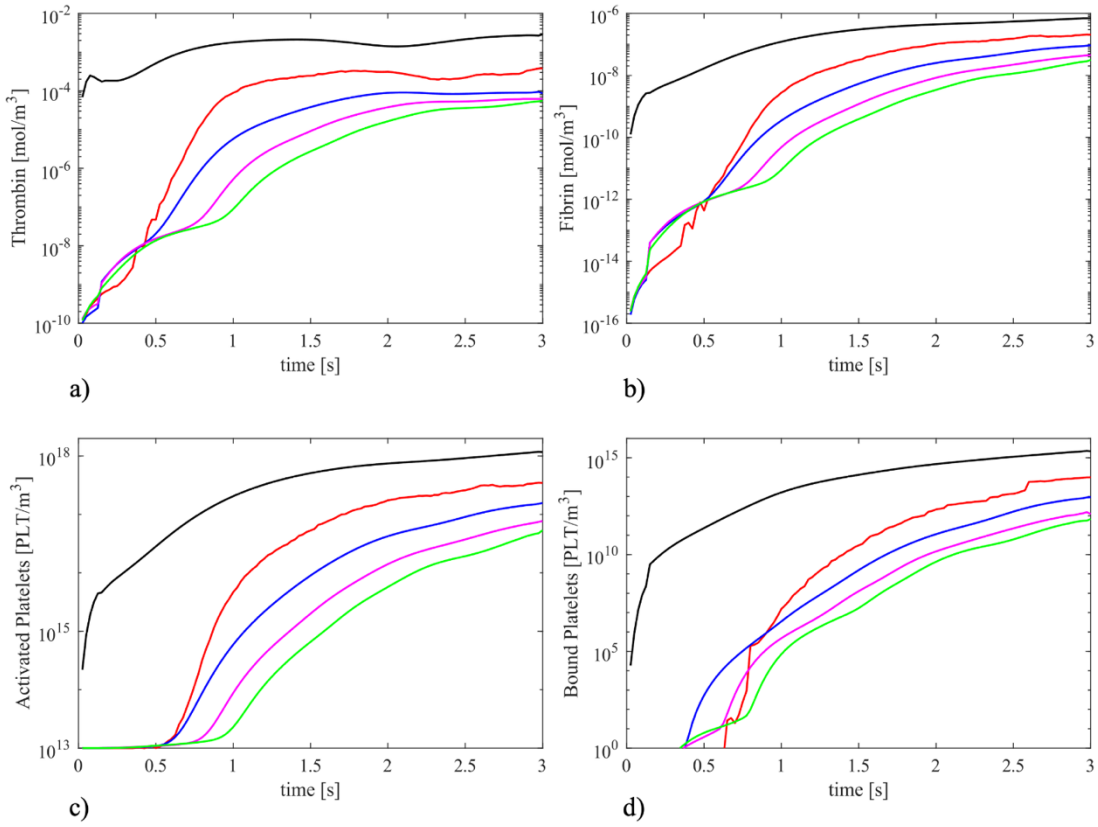

Figure 36 - Time evolution of the selected clotting factors considering five different points (see Fig 14). Black continuous line: point A; red dotted line: point B; blue dashed line: point C; magenta dashed line: point D; green dashed-dotted line: point E. Plotted used logarithmic scale in concentration axis(image taken from [50], p.20, fig.15)

4.5 Conclusions

The presented method is able to realistically describe the thrombosis phenomenon, including blood clotting variables (platelets, coagulative cascade enzymes), hydrodynamic parameters (shear strain rate and velocity) and mutual interactions between fluid dynamics of blood and the forming thrombus. The numerical model was developed following several fundamental steps to define the definitive model, such as the diffusion of tracers and the possible options to simulate platelets aggregated through spring bonds. Finally, an experimental test case presented in the literature was used to validate the methodology described here. In terms of the size and shape of the thrombus generated at the height of the step, the numerical results closely match the experimental results.

Chapter 5

5. Bioengineering applications of the proposed thrombosis model

5.1 Numerical modelling of thrombosis in cerebral aneurysms

A major application of controlled thrombosis is in the treatment of cerebral aneurysms.

Several studies [71]–[76] have developed computational methods aiming at simplify the interventional planning process but at the same time guaranteeing adequate support for preventive diagnostics. The literature describes models that address various aspects of intracranial aneurysm thrombosis. is the main focus is on developing multifactorial computational models that take into account the key parameters of the process to predict and explain thrombus formation in cerebral aneurysms.

Numerical modelling could play an important role from a clinical point of view, as it could offer an advantageous technique for evaluating the possibility of rupture of cerebral aneurysms in the case of spontaneous thrombosis but, at the same time it could predict and evaluate the conditions that occur following the implantation of a flow diverter, in the case of induced thrombosis. The chapter seeks to examine the phenomenon of thrombosis in cerebral aneurysms, evaluating the biochemical and hemodynamic factors that play a relevant role in the process. In particular, two different cases of thrombosis were analysed, the first is spontaneous thrombosis, which occurs more frequently in giant aneurysms than in small ones, while the second is thrombosis induced by an endovascular device. Ideal aneurysm geometries made using CAD modelling software were used and the thrombosis model (described in chapter 4) was employed.

5.1.1 Clinical classification of thrombosis in cerebral aneurysm

Cerebrovascular disorders such as cerebral or intracranial aneurysms are characterised by abnormal dilation of intracranial vessels caused by degenerative changes to all layers of the vessels, as shown in Figure 37. The aneurysms are frequently located near arterial bifurcations at the circle of Willis, a system of arterial anastomoses at the base of the braincase.

Figure 37 – DICOM of cerebral vessels where an aneurysm is located.

These pathologies carry an intrinsic risk of rupture resulting in intracranial haemorrhages which have a high associated mortality and morbidity rate [77]. Aneurysms that rupture can cause haemorrhage in the brain parenchyma and subarachnoid space, respectively. The latter is the one that occurs most frequently and has a mortality rate ranging from 25% to 50%. Furthermore, very serious permanent disabilities occur in 50% of survival cases [78].

It is particularly difficult to treat intracranial aneurysms because they often rupture without any symptoms. The development of neuroradiological techniques has improved the detection of unruptured aneurysms, so preventive treatments are currently considered valid therapeutic options. Although every treatment has a risk, it is best to treat aneurysms that pose a real threat of rupture; therefore, treatment planning requires a better understanding of the process of cerebral aneurysm formation

and growth as well as research into the consequences of the treatment. It is widely acknowledged that the interaction between haemodynamics and mechano-biology of the vessel wall plays an important role in the pathogenesis of cerebral aneurysms, although the mechanisms are unclear. Cerebral aneurysms are commonly associated with anatomical changes and pathological conditions such as hypoplasia or occlusion of a segment of the circle of Willis that locally cause increased flow in the cerebral circulation and, at bifurcation points. A significant incidence of cerebral aneurysms was associated with non-modifiable risk factors such as age and sex. Moreover, women are more likely to suffer from this disease than men in all age groups. The main modifiable risk factors are associated with excessive alcohol consumption, cigarette smoking, untreated hypertension, estrogen deficiency and high cholesterol.

Intracranial aneurysms can be classified into ruptured and unruptured aneurysms, in the latter case the aneurysm can be asymptomatic or symptomatic. Typically, ruptured aneurysms are discovered because they directly cause subarachnoid haemorrhages while unruptured aneurysms are usually found indirectly and incidentally by diagnostic tests.

Aneurysms can be classified according to various criteria based on location, morphology, and size (see [77], [78]). For example, based on the morphology they are divided into saccular and fusiform aneurysms. Saccular aneurysms are the most frequent (90%) and are characterised by a saccular outpouring from the parent vessel, they are located mainly in the anterior circle. Instead, fusiform aneurysms are segmental dilatations that affect the entire cross-section of the lumen. Based on the size it is possible to distinguish: small aneurysms (diameter < 10 mm); large aneurysms (10 mm < diameter < 25 mm) and giant aneurysms (diameter > 25 mm).

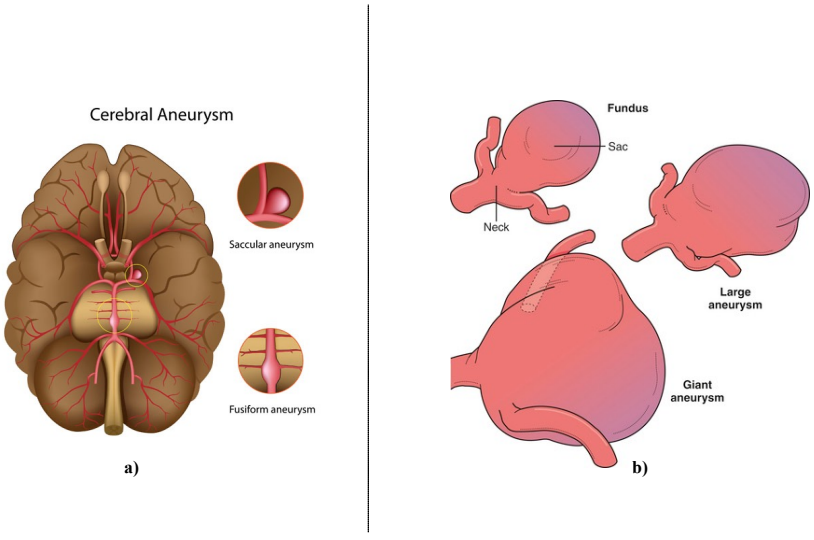

Figure 38 – General classification of cerebral aneurysms. a) Indication of saccular and fusiform aneurysms (taken from: https://orangecountysurgeons.org); b) small, large or giant aneurysms (taken from https://clinicalgate.com)

5.1.2 Cerebral aneurysm treatments

In general, the treatment options for patients diagnosed with a cerebral aneurysm are:

- medical therapy;
- surgical treatment or clipping;
- endovascular treatment or coiling.

Medical therapy is one of the options for treating an unruptured intracranial aneurysm. Strategies include changes in the patient's lifestyle (such as smoking cessation), blood pressure control, and the selection of appropriate medications. In addition, continuous monitoring is to examine the size and possible growth. Microsurgical clipping is a neurosurgical technique that allows direct surgical cutting using a metal clip after performing a craniotomy that allows direct access to the aneurysm. There are different clips for aneurysm locations, the final clip choice is highly individualized, based on the angioarchitecture of the specific aneurysm. Endovascular neurosurgery is a minimally invasive technique that is rapidly emerging as the mainstream treatment for many intracranial aneurysms. Coils are the first devices used for the endovascular neurosurgical treatment of an intracranial aneurysm. The treatment involves the use of a catheter that reaches the cerebrovascular system from the femoral artery and the location of the aneurysm. Nowadays, the innovative concept of flow-diverting offers a unique intraluminal approach to the management of cerebral aneurysms. The flow diverter is characterised by the insertion of a metal mesh, at the vessel hosting the aneurysm. Its function is to redirect the blood flow of the aneurysm so as not to acutely occlude the aneurysm. In contrast to traditional endovascular treatments, flow diverters induce thrombosis in the aneurysm sac through a reticular structure that promotes endothelization.

The main challenge is to evaluate the possible effect of thrombosis in cerebral aneurysms, identifying the complex mechanisms that lead to the formation of thrombosis within the aneurysm lumen. The current hypothesis assumes that the

thrombus, by occluding the aneurysm, modifies the pathological flow conditions that have arisen due to the presence of the aneurysmal cavity and re-establishes the normal physiological flow.

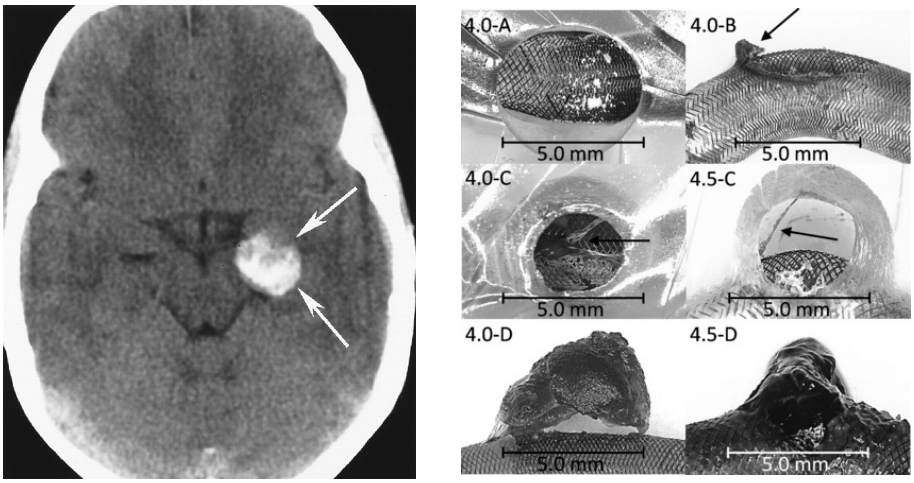

Figure 39 – Thrombosis in cerebral aneurysms: a) thrombus in axial CT in cerebral artery aneurysm in a child (image taken from [79]) b) thrombi growth in flow diverter inserted into the aneurysm (image taken from [80])

Aneurysm stability will be assessed by evaluating hemodynamic conditions in both physiological and pathological conditions. As well as presenting asymptomatically, thrombosis can mimic a brain tumour, causing seizures or an ischemic stroke. Depending on whether the thrombus occupies the entire internal volume of the aneurysm or not, this pathology can be complete or partial; moreover, it has been observed in ruptured, as well as unruptured aneurysms. Complete thrombosis of a cerebral aneurysm after rupture is a well-known event linked to hypotension, vasospasm, and local arterial wall damage. The incidence ranges from 1% to 2% and can increase up to 3% in patients treated with antifibrinolytic agents. Several factors affect intra-aneurysmal thrombosis, including the growth of the aneurysm and the installation of a flow diverter. Spontaneous intra-aneurysmal thrombosis is a well-documented phenomenon that has been observed in approximately 50% of giant intracranial aneurysms; with a lower incidence of defective for cases of complete occlusion than for cases of partial incidence [13]. On the other hand, the process of spontaneous thrombosis in small cerebral aneurysms has rarely been described and, in general, is poorly understood. In cases of unruptured aneurysms, thrombosis can stabilize the aneurysm but may accelerate the path to

rupture. Both spontaneous and externally induced thrombosis, such as flow diverters, are subject to these considerations.

5.1.3 Case study of spontaneous thrombosis in an ideal giant intracranial aneurysm

Giant intracranial aneurysms are defined as aneurysms with a dome's diameter greater than 25 mm. Another geometrical parameter used to classify them is the aspect ratio (AR) (shown in Figure 40) which is the maximum perpendicular height (h) of the aneurysm divided by the average neck diameter of the aneurysm (w).

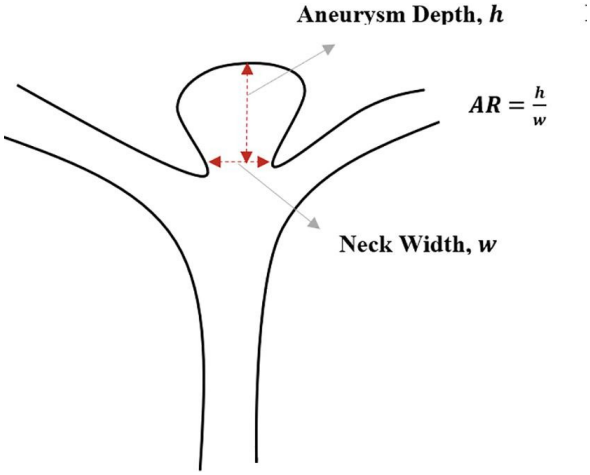

Figure 40 – Definition and representation of AR in an aneurysm

The ideal model of a giant aneurysm was modeled considering the artery as a cylinder of the constant section with a diameter equal to D_{artery} = 5.2 mm and length L = 104 mm. The aneurysm, on the other hand, was generated starting from a spherical shape with a diameter of 26 mm (equal to $5D_{artery}$). The geometric representation of the giant aneurysm is shown in Figure 41. In this study, blood was modelled as Newtonian fluid with density equal to 1,060 kg/m^3 and dynamic viscosity of 0.003 poise. This is consistent with other hemodynamic simulations of cerebral aneurysms reported in the literature [81]. As inflow and outflow boundary conditions, 0.2 m/s was set at the inlet, and zero pressure at the outlet. The blood flow regime was assumed to be laminar, and no turbulence modelling was performed since Reynolds numbers in large vessels are generally below the turbulence threshold [82], [83]. Furthermore, the steady flow assumption was made without considering the pulsatile motion of blood flow.

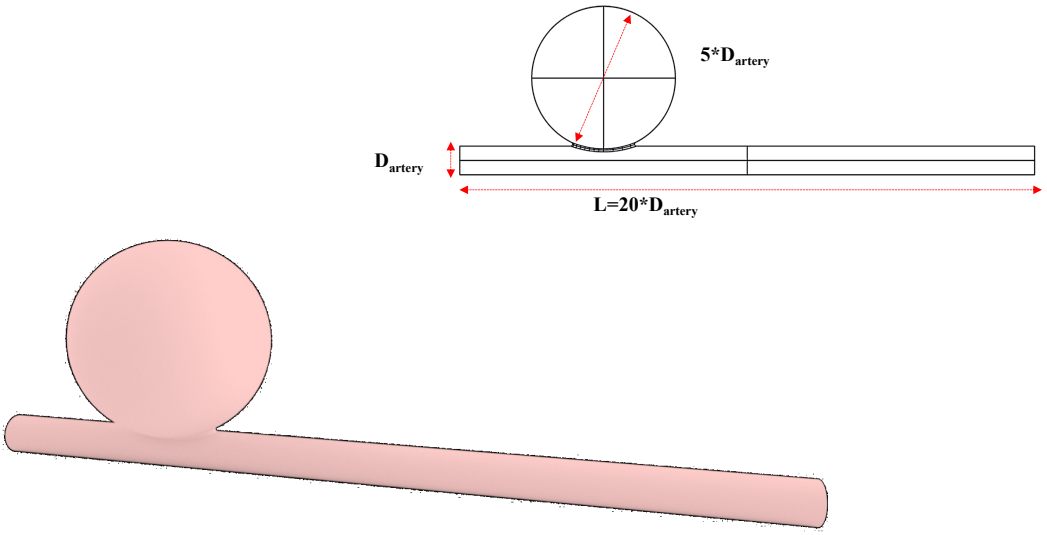

Figure 41 – Geometrical dimension of the giant cerebral aneurysm (D_{artery}=5.2 mm)

Initially, the hemodynamic variables of interest (such as velocity and SSR) were determined for the case of the giant aneurysm. The first variable considered is speed. In the case of a giant aneurysm, it is possible to observe that the velocity is higher inside the main vessel, and rapidly decreases in the neck and in the distal part of the aneurysm until it is close to zero in the remaining part of the aneurysm sac as shown in Figure 42a. Another hemodynamic variable subject to considerable attention due to its possible effects on thrombus development is the Shear Strain Rate (SSR) [84]. As shown in Figure 42b higher values are observed within the main vessel and lower values are observed in the distal part of the aneurysm sac. According to Musotto *et al.* [25], SSR directly affects flow and alters the balance between procoagulant biochemical species, such as thrombin, and anticoagulants, favoring the accumulation of the former and reduction of the latter. Hemodynamic parameters such as velocity and SSR influence coagulation, so they influence thrombus formation.

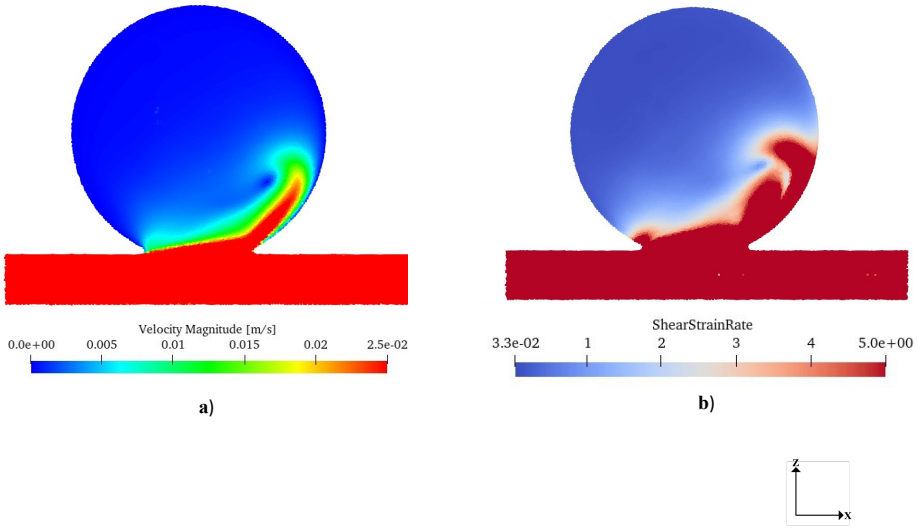

Figure 42- Hemodynamic parameters considering steady flow condition a) velocity b) SSR

In the simulation, the kernel width was set to 0.25 mm, resulting in a total of 1,000,000 particles. The concentrations of the modelled species were initialised in the bulk through a steady-state simulation imposing the typical values in healthy human blood (as reported in Table 2) except for the concentrations of fibrin and bound platelet, which were set to zero. The concentration of thrombin is imposed equal to 9.11×10^{-10} mol/m^3 to simulate a state of hypercoagulability of the blood. In fact, according to Virchow's triad, the formation of thrombus is promoted, among other, by the presence of stasis and hypercoagulability.

To decrease the computational times of the thrombus formation process in this case study, the thrombin concentration was amplified using a sigmoid function, called λ, and represented by:

$$\lambda = a\,\frac{SSR_t^n}{SSR_i^n + SSR_t^n} \qquad (5.1)$$

where a is an adimensional coefficient equal to 10^6, n is the exponent equal to 2, SSR_i is the value calculated for each particle at t instant, SSR_t is an imposed threshold value equal to 3 s^{-1}.

Initially, the time evolution of the concentrations of selected biochemical species, such as thrombin and fibrin, was evaluated.

It is possible to observe (see Figure 43) that the concentration of thrombin evolves rapidly until it reaches a concentration equal to 1×10^{-6} mol/m^3 , which is the limit concentration value that allows the activation of platelets as described in 4.1.

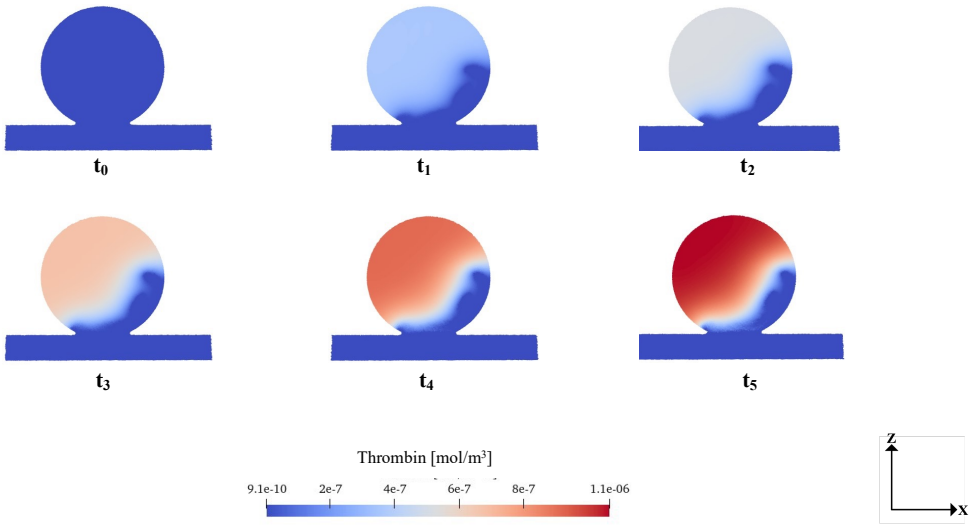

Figure 43 – Thrombin concentration trend: t_0=0 s, t_1=0.25 s, t_2=0.5 s, t_3=0.75 s, t_4=1 s, t_5=1.25 s.

However, the concentration of fibrin evolves less rapidly in the first instants of coagulation (see Figure 45). This phenomenon is regulated by a kinetic constant which determines the reaction rate. In the case of fibrin, the initial concentration is zero and the final value is instead equal to 3.9×10^{-11} mol/m^3.

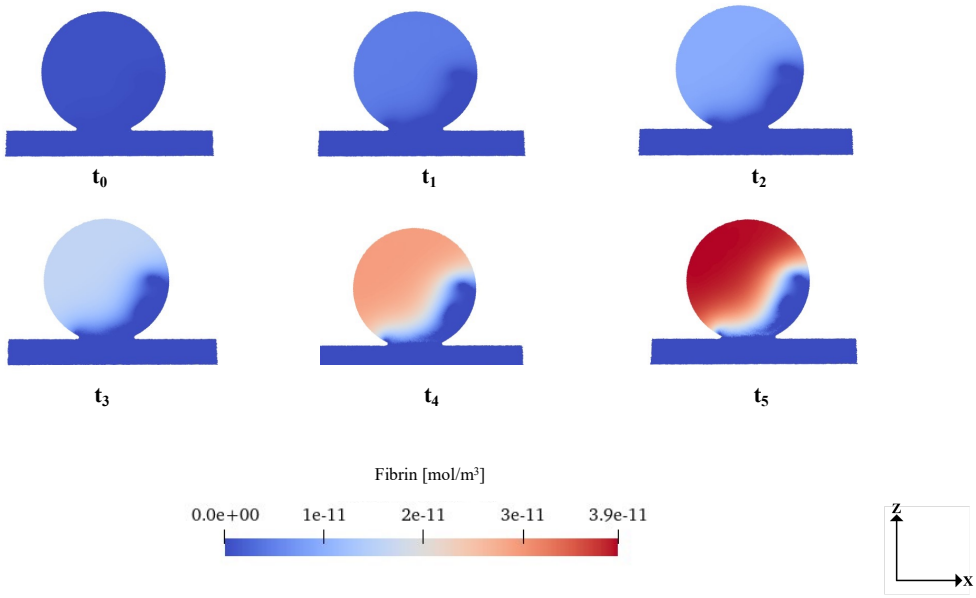

Figure 44 – Fibrin concentration trend: t_0=0 s, t_1=0.25 s, t_2=0.5 s, t_3=0.75 s, t_4=1 s, t_5=1.25 s.

The formation and growth of thrombus in the cerebral aneurysm was then analysed. Figure 45 shows the development until the stationary condition is reached, it is noted that the thrombus first progresses rapidly and then the development slows down significantly. The thrombus forms from the superior proximal area within the

aneurysm sac. Aneurysms typically develop thrombi along the wall before spreading to the center. The speed with which the thrombus develops inside the aneurysmal cavity is linked to the propagation of coagulation factors on its surface. This propagation stops when the swirling flow within the aneurysm does not allow further platelet recruitment. Although a high percentage of the aneurysm volume has been occluded by the thrombus, the occlusion is not complete.

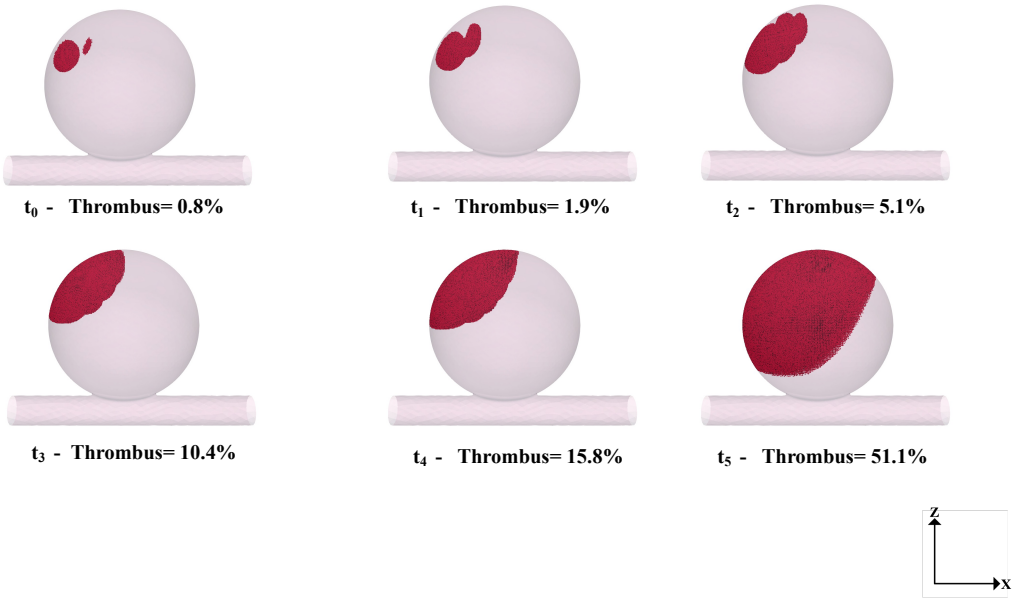

Figure 45 – Evolution of spontaneous thrombus: t_0=0 s, t_1=0.25 s, t_2=0.5 s, t_3=0.75 s, t_4=1 s, t_5=2 s (red area=thrombus) and percentage of occlusion

It is possible to make further considerations regarding the velocity inside the aneurysm in hydrodynamic conditions and when the thrombus has reached its maximum development. As shown in Figure 47, the velocity profile in the two cases has changed due to high increase of thrombus volume.

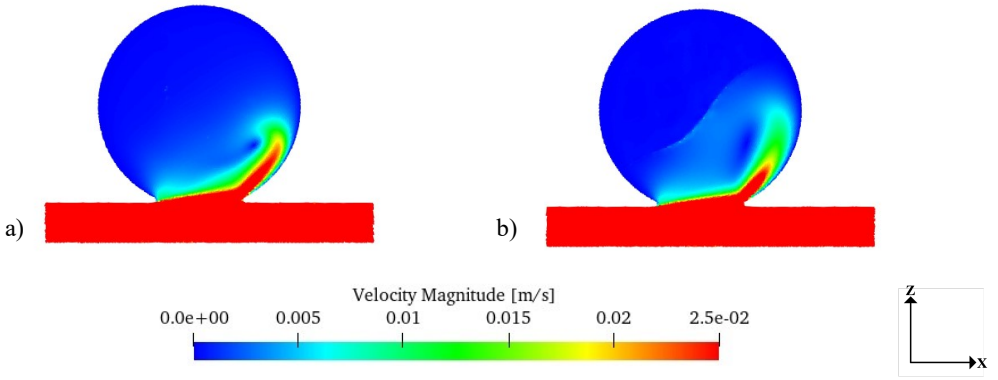

Figure 46 – Velocity field without (a) and with (b) the activation of the thrombus formation model

5.1.4 Case study of thrombosis induced by flow-diverting treatment in an ideal small cerebral aneurysm

The second case study discussed in this paragraph aims at the description of induced thrombosis in a small aneurysm with a flow diverter (FD) [15]. The ideal model of a small aneurysm was modeled considering again the artery as a cylinder of the constant section with a diameter equal to D = 5.2 mm and length L = 104 mm. The diameter of the dome is equal to the artery's diameter D. The geometry of the flow diverters was created using the 3D modelling software Rhinoceros. In this case, the grid that simulates the device was created by generating parallel segments and arranging them in two directions at 45° and -45°. To generate a regular grid, segments are separated by 0.62 mm, as shown in Figure 47.

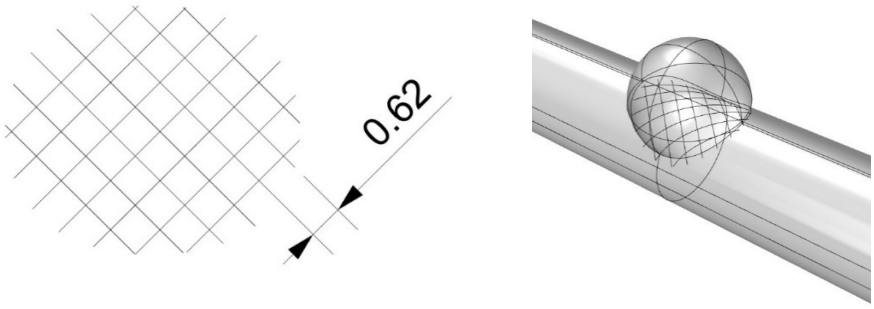

Figure 47 – Geometrical construction of the flow diverter

Starting from the simple geometry described, a tubular geometry was constructed in which the radius of the wires of the device was set equal to 0.2 mm. As the objective of this study is to determine the mechanisms that lead to thrombosis in the presence of flow diverters. Two views of the described structure are shown in Figure 48. Due to computational constraints, the flow diverter model is not generated in its entirety, but only in the part relating to the neck of the aneurysm, as a region of interest. This is the first phase of the simulation which is called FD identification (action 1 of the diagram of Figure 51)

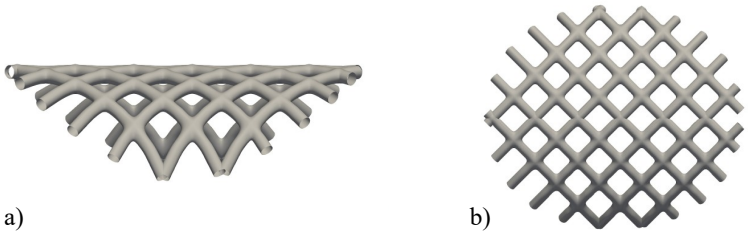

Figure 48 – a) 3D Front view of FD b) 3D top view of FD

The first phase of the study consists in the evaluation of hemodynamic parameters in the small cerebral aneurysm with and without FD. In Figure 49 it is possible to observe it.

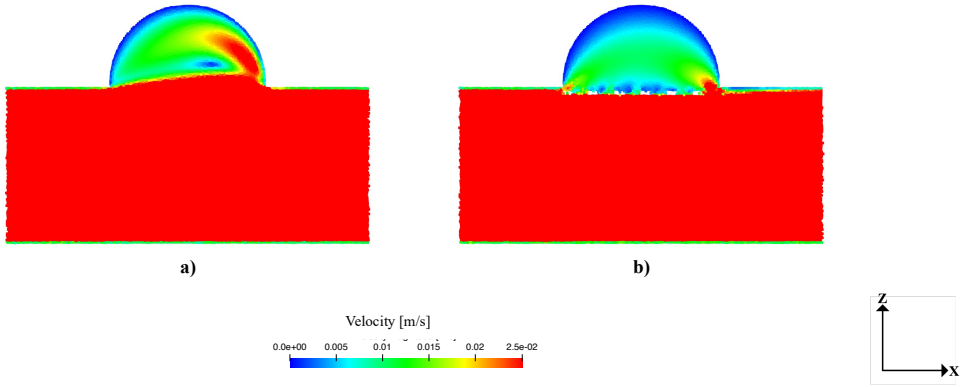

Figure 49 – Velocity field without (a) and with (b) FD.

When the flow diverter is not inserted into the vessel (see Figures 50-51 a), the flow enters the aneurysm from the distal neck, causing a vortex to occupy the entire volume of the aneurysm sac. Instead, in case the flow diverter is present in the vessel, as shown in Figures 50-51b, it is possible to observe a significant change in the flow inside the aneurysm. The flow diverter has significantly slowed down the flow near the upper central part of the device since the speeds near the walls of the dome of the aneurysm have decreased.

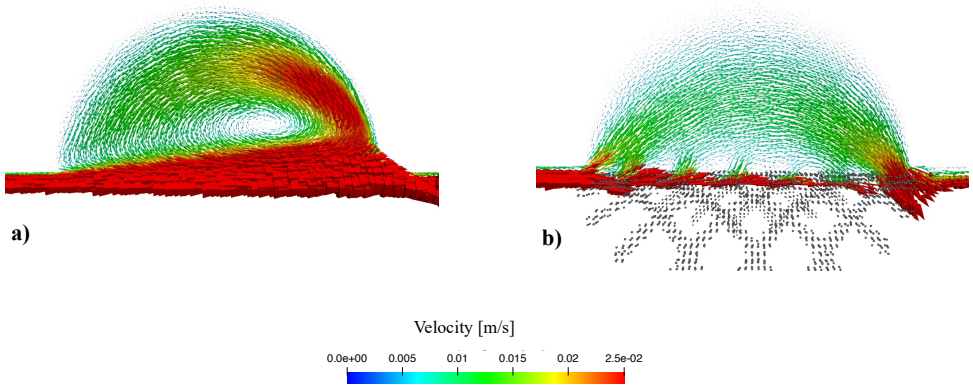

Figure 50 – Velocity vectors without (a) and with (b) FD

Another interesting and challenging aspect consists in the modelling of FD through the FSI SPH solver, the same used to simulate thrombosis phenomena. Simulating fluids and solids and their interactions are possible with the monolithic solver where no interface is needed. The particles that compose the fluid diverter are fixed in the initial geometrical distribution and they are interconnected between the elastic links.

Figure 51 shows a summary of the settings modified in PANORMUS code. First, the central axis of the wires of flow diverter's grid is created to identify the particles that are part of it, as previously mentioned (ACTION 1). The other steps are the same as described in 4.3.3. Another important change is the introduction of the FD boundary condition (ACTION 8) which is realized by imposing no velocity on FD particles.

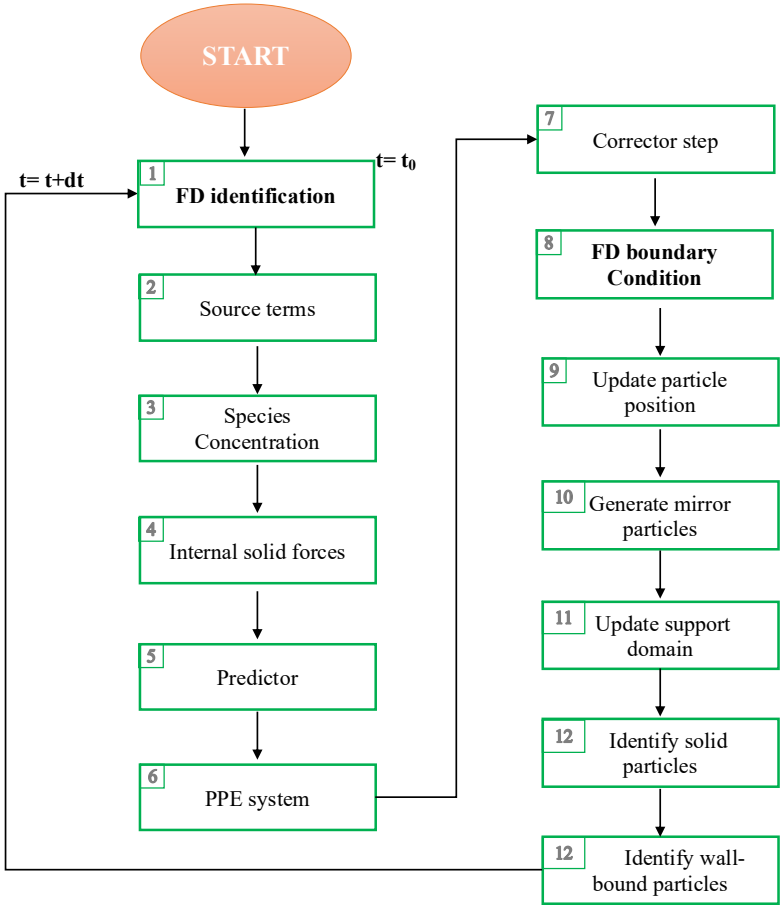

Figure 51 – Flowchart of the proposed FD model with thrombus formation

As reported in the literature [71], [73], [85], the flow diverter deployment, flow disruption and subsequent stable thrombus formation within the aneurysm are primary events that play a critical role in the aneurysm occlusion. Hence, the thrombosis phenomenon occurs because of the stasis condition and interaction with thrombogenic materials [80], [86], [87] (FD) are satisfied. To simulate it, a concentration of thrombin (equal to 0.09 mol/m^3) from the flow diverter was considered (see Figure 52). The high value chosen is selected to speed up the simulation and reduce computational costs.

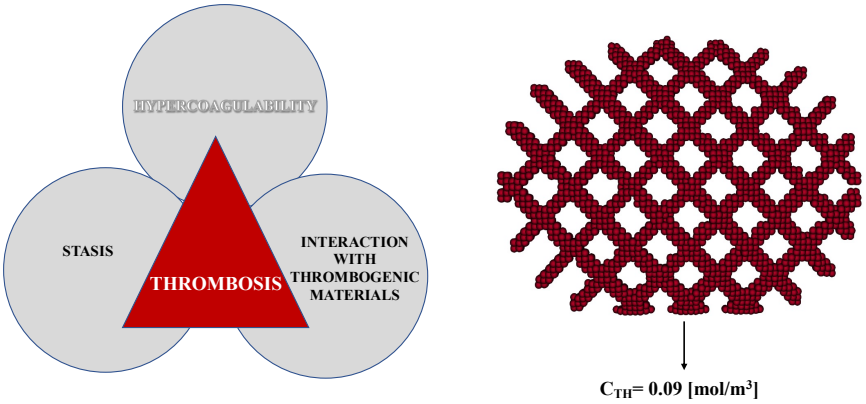

Figure 52 – Initial condition of thrombosis in small cerebral with FD

From the flow diverter to the aneurysm sac, the concentration of biochemical species evolves. Figures 55-55 show the evolution of thrombin and fibrin concentrations. Thrombus forms primarily in the proximal and upper parts of the flow diverter, while the distal part, where the velocity field is higher, remains non-thrombotic. As shown in Figure 55, it is also possible to observe that the thrombus has completely occluded the proximal part of the flow diverter, altering the flow and hemodynamic characteristics of the aneurysm. This is evident and easily visible in Figure 56 where there is a comparison of the velocity field in the two different cases.

The results of the performed numerical simulations clearly show that thrombus formation in an idealised geometry of a cerebral aneurysm involves a complex interaction between hemodynamic and biochemical factors. In both cases, it is evident that the thrombus forms in areas with very low velocity. Accordingly, stasis facilitates the development of thrombi, as postulated by Virchow. Stasis, by ensuring that thrombin reacts with fibrinogen to form a fibrin network that is not made unstable by the flow. The thrombus initially consists of a small mass, then develops by spreading to regions where the flow is slower. The speed of propagation is limited by the speed and availability of biochemical factors that affect the propagation of thrombus inside aneurysmal cavities.

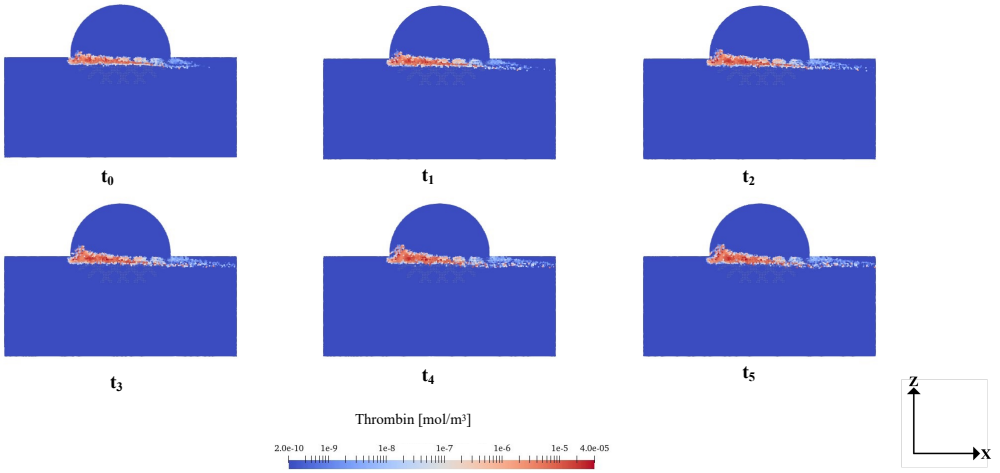

Figure 53 – Temporal growth of thrombin concentration t_0=0.1 s, t_1=0.2 s, t_2=0.3 s, t_3=0.4 s, t_4=1 s, t_5=0.5 s

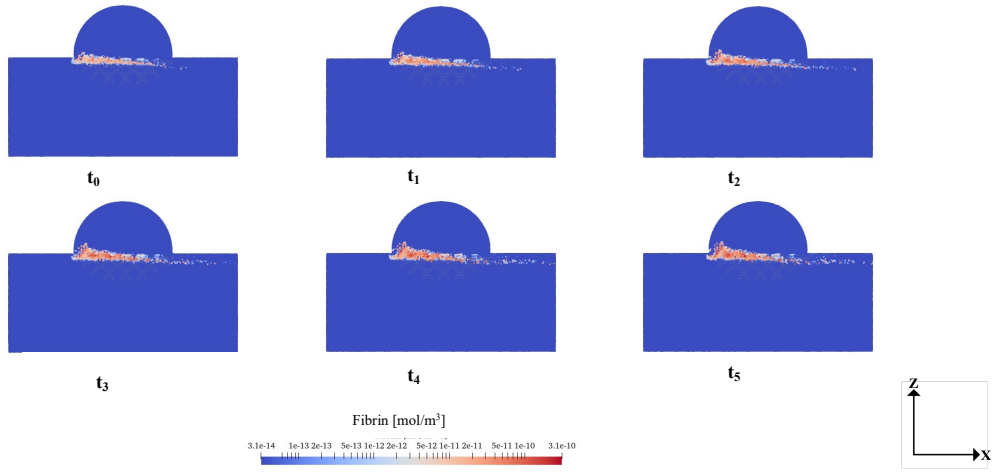

Figure 54 – Temporal growth of fibrin concentration t_0=0.1 s, t_1=0.2 s, t_2=0.3 s, t_3=0.4 s, t_4=1 s, t_5=0.5 s

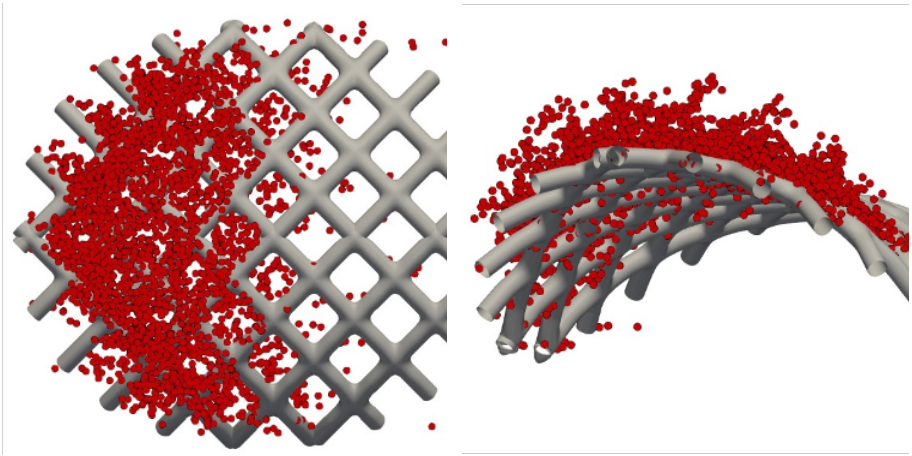

Figure 55 – Thrombi occlusion in flow diverter

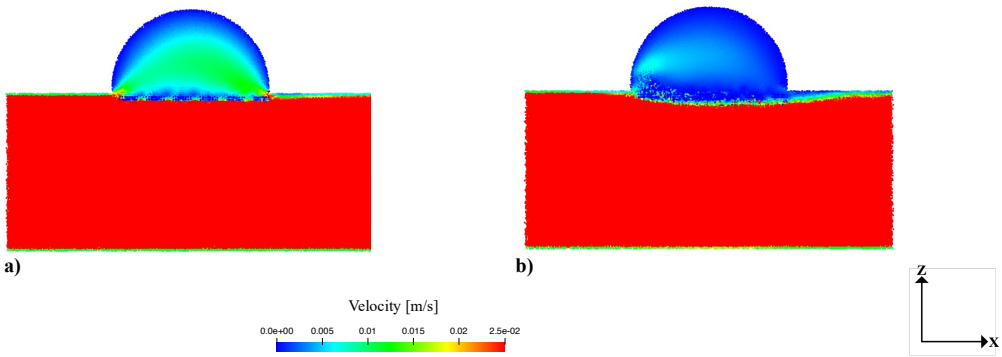

Figure 56 – Velocity field in the small aneurysm treated FD without (a) and with (b) the thrombus

5.2 Thrombus modelling inpatient-specific left atrial appendage

5.2.1 Thromboembolic risk in the left atrial appendage

Atrial fibrillation (AF), a heart arrhythmia characterised by irregular electrical activity because of numerous trigger points on the atrial surface, greatly increases the risk of clot formation. The left atrial appendage (LAA) was the site of the vast majority of intracardiac thrombi [88], [89] found in people with AF, even though the pathogenesis is still unknown.

Anatomically, the left atrial appendage is located next to the left atrium (see Figure 57). It is partially positioned on the exterior wall of the left ventricle and shares structural continuity with the left atrium. The changing phases of the cardiac cycle affect the left atrial appendage's filling and emptying times, and its morphological and physiological properties are considerably different from those of the atrium. When the atrial pressure is high, such as during ventricular systole, the left atrial appendage functions as a decompression chamber.

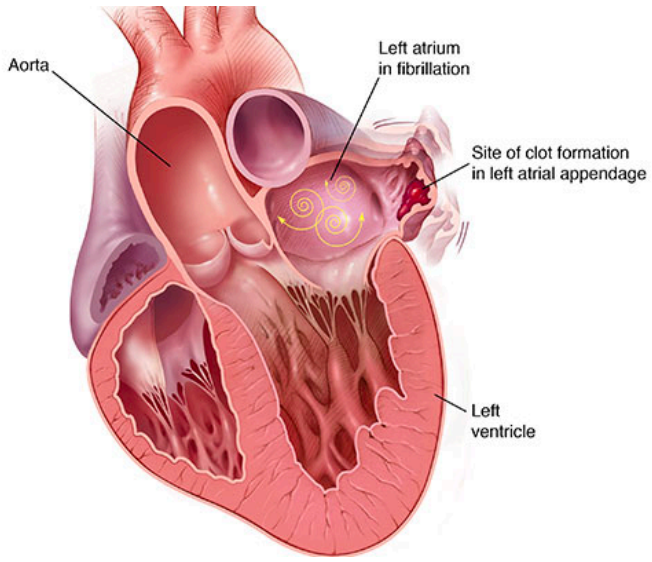

Figure 57 – Schematic representation of atrium in fibrillation (image taken from https://www.pinterest.it/pin/379639443571345737)

The LAA derives from the primordial left atrium (LA), which is formed mainly by the adsorption of the primordial pulmonary veins and their branches. It is a finger-like projection from the main body of the LA. The morphological classification of the left atrial appendage is one of the features to emphasise. This anatomical shape is

highly variable and varies from patient to patient. A typical classification comprises four broad groups based on the shape that it recalls (see Figure 59). In particular, the chicken wing morphology is the most prevalent (48%), followed by the cactus (30%), Windsock (19%), and cauliflower (3%) morphologies.

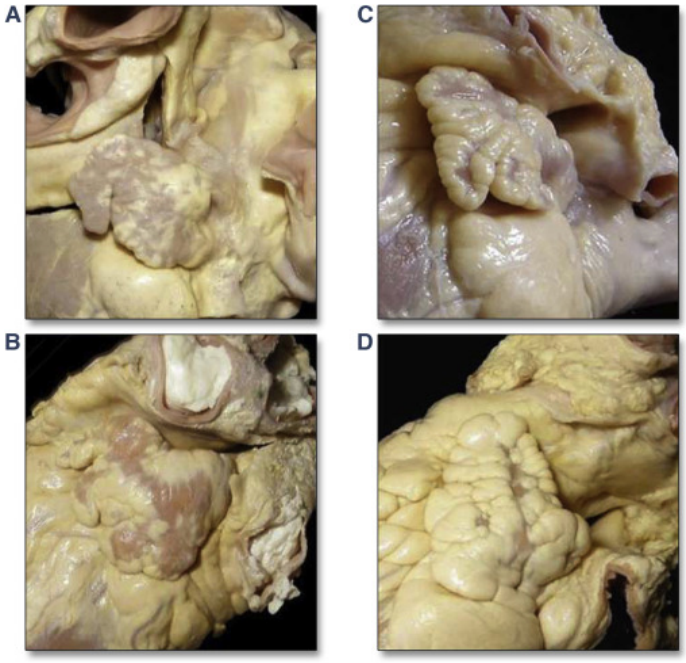

Figure 58 – LAA morphologies' s examples of explanted hearts of different: (a) Chicken wing; (b) Windsock; (c) Cauliflower; (d) Cactus (image taken from [90])

As mentioned before, AF is one of the most common type of heart arrhythmia. Arrhythmia is when the heart beats too slowly, too fast, or in an irregular way. AF occurs when the electrical impulses in the heart atria are triggered chaotically from different foci, causing them to quiver or twitch (fibrillation). Patients describe the resulting feeling as a heart fluttering or racing (known as palpitations). Electrocardiographically, this disorder is characterized by multiple trigger points on the atrial surface and by the absence of the P wave and the aperiodic R-R segment (shown in Figure 59).

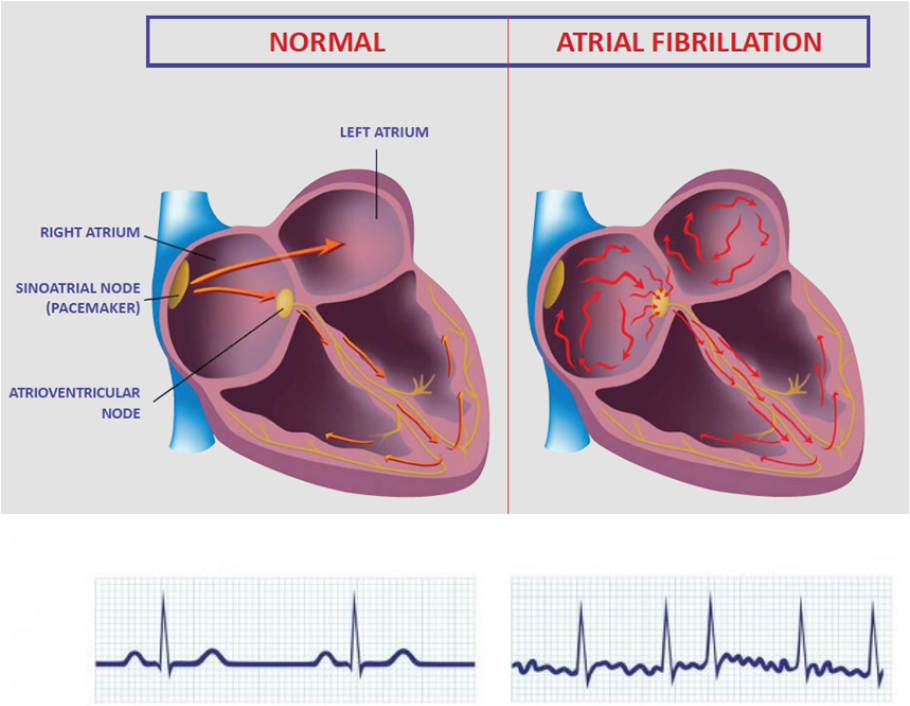

Figure 59 – Sinus rhythm and atrial fibrillation in electrocardiogram (ECG) (image taken from https://www.feinberg.northwestern.edu/giving/stories/_stories/arrhythmia- research-center-2019.html)

The possible relation between LAA morphological classification and the thrombo–embolic risk has been widely investigated in the literature, and several numerical studies have been performed on patient-specific models, aiming at identifying hemodynamic changes produced by AF that can be promote unwanted clotting.

In particular, Bosi *et al*. [91] presented computational models that highlight the major role played by the LAA morphology on the haemodynamics, both in normal and AF conditions, revealing the potential support that numerical analyses can provide in the stratification of patients under risk of thrombus formation, towards personalised patient care. Vella *et al.* [24] analysed LAA considering sinus and fibrillation contractility that is modelled by applying wall velocity/motion to models based on healthy and dilated idealised shapes of the left atrium. They indicated that the alterations in contractility and morphology associated with AF pathologies play a primary role in establishing hemodynamic conditions which promote a higher incidence of ischaemic events. Starting from Vella's work, Musotto *et al*. [25] presented a complete FSI study (considering wall motion caused by AF) applied to LAA patients-specific geometries. Di Biase *et al*. [92] investigated the LAA by CT and MRI to classify different LAA morphologies and correlate the morphology with

embolic cerebrovascular events in patients with AF. Based on the study population, stroke or transient ischemic attack (TIA) prevalence rates were 12% for those with the cactus morphology, 4% for the chicken wing morphology, 10% for the windsock morphology and 18% for those with the cauliflower morphology. Villalba *et al*. [93] investigated how LA anatomy and function impact on LA and LAA haemodynamics, and explored whether patient-specific analysis by computational fluid dynamics (CFD) can predict the risk of LAA thrombosis. They analysed 4D-CT acquisitions of LA wall motion with an in-house immersed-boundary CFD solver. Hautmann *et al.* [94] emphasised that, considering different clinical case studies, LAA thrombus formation is promoted by advanced structural heart disease, inflammation, diabetes and impaired renal function. Younger age, non-permanent AF and higher LAA flow velocities were predictors of thrombus resolution.

In conclusion, several studies in the literature have highlighted the clinical importance of studying the presence of thrombi in LAA. A diagnostic phase is being sought to identify aspects (low velocity, SSR, and morphology) that can predict thromboembolic risk in one individual versus another. The next paragraph will illustrate a methodology adopted to individuate thrombus formation in LAA patients-specific model in AF condition.

5.2.2 FSI simulation of LAA with ANSYS software

The main purpose of this paragraph is to describe the methodology used to reproduce the physiological and atrial fibrillation conditions of LAA [22] .

Software from the ANSYS WORKBENCH platform was used in this stage. The platform is suitable for treating multi-physical systems. For the structural part of the numerical model, ANSYS TRANSIENT STRUCTURAL software was used. The fluid dynamics simulations were performed using ANSYS CFX, and the two-way coupled simulations were performed using ANSYS SYSTEM COUPLING. A component of ANSYS Workbench is System Coupling. Simulations in based on multiphysics approaches can be run on this environment.

As shown in Figure 60, the first step is to reproduce the geometry of the LAA and transform the computed tomography scan into a suitable domain for the analysis. The analysed LAA geometries were defined starting from patient-specific morphologies used in Bosi's work [91].

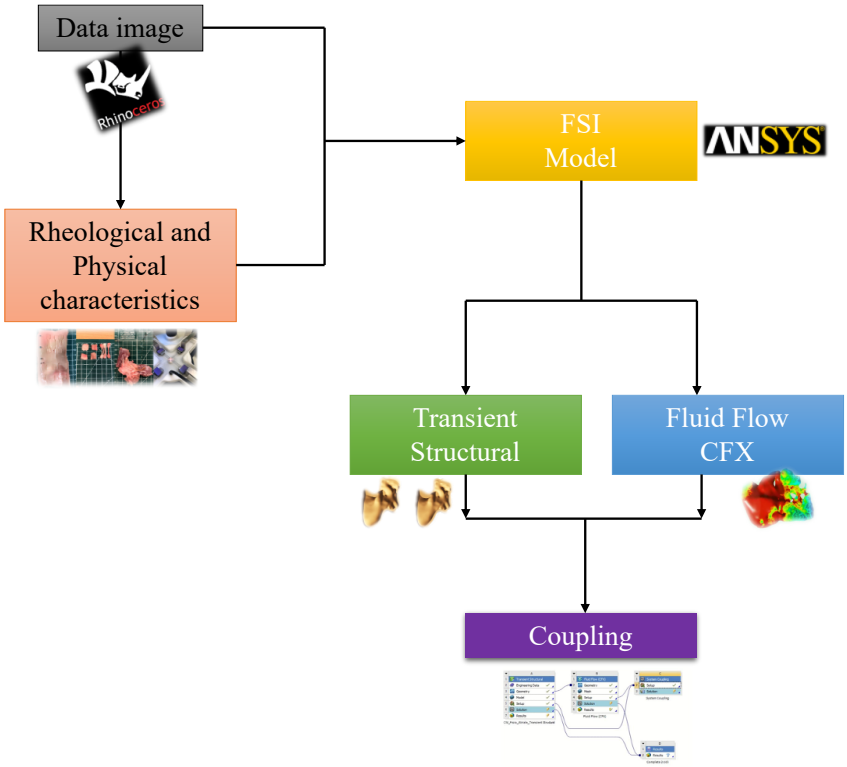

Figure 60 – Schematic view of FSI study applied to LAA

These are based on radiological scans that return the blood content internal to the LAA and represent the four typical morphologies of the adult population not affected by AF. First, the internal wall surface (corresponding to the external blood surface) was smoothened to remove all discontinuities caused by the trabeculae and offset by 2.1 mm in the external direction. In particular, the internal and external meshes were transformed into poly surfaces and integrated into a solid volume through the commercial computer-aided design (CAD) software Rhinoceros 7.0. Chronic AF is typically associated with an enlargement of the LAA volume. This condition is well documented for its increase in volume but in literature has no quantitative information on the anatomical changes associated with this remodeling. Hence, to verify potential fluid dynamic changes produced by persistent AF, enlarged versions of the four LAA models were created by scaling them up by 150%.

The second phase involves setting the assumptions for the rheological and mechanical properties. As for blood, it was preferred to model the fluid as Newtonian, with a density of 1,062 kg/m^3 and a viscosity of 0.0037 Pa·s, replicating the common physical properties of human blood at large shear rates.

The non-linear constitutive behavior of biological soft tissues [27] is characterised by a low-modulus region, a transitional region with progressive

stiffening with strain increases, and a stiff region at greater strains. Anisotropy is typically reduced in the LAA wall [27] and was therefore neglected. Since the clinical morphological scans were taken from pressurised operating hearts, the wall material was modeled as linear elastic. The Young's modulus was set equal to 1.5 MPa, a value intermediate between those low and high regions reported for porcine heart left atria [35]. In this study, a Poisson's ratio of 0.49 was used. This factor accounts for the material's incompressibility. A combination of elastic tissue response to pressure variation and active contraction of the wall muscle is reported to reduce LAA volume by approximately 60% of its maximum value during contraction.

As for the boundary conditions, different loads are applied to simulate AF or sinus conditions of LAA. Physiological atrial pressure was applied uniformly at the open surface of the fluid to simulate standard sinus rhythm conditions [25]. Then a virtual change of temperature was applied to the structure to simulate active contraction (see Figure 61). A constant virtual temperature of 0 °C was applied to simulate acute AF conditions, and the pressure curve was modified to account for the lack of atrial contraction at a fluid-free surface [25].

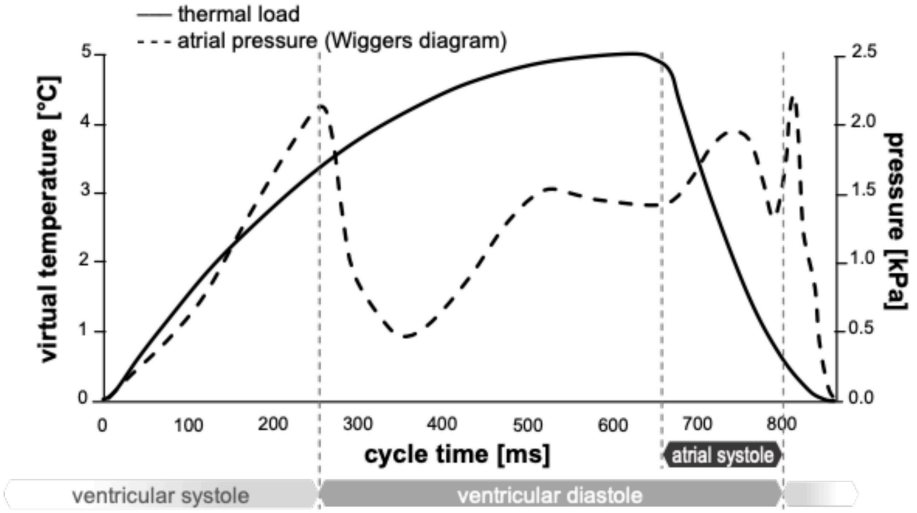

Figure 61 - Thermal load (continuous line) and physiological atrial pressure curve (dashed line).(image taken from[25], p.5, fig.4)

The simulated heart rate was 70 beats/min, resulting in a cycle duration of 860 ms.

The SSR variable was used to identify areas with a greater thromboembolic risk. To identify regions of the potential risk of thrombosis, the fluid-wall surface that remains exposed for the entire duration of the cycle to SSR values below 10 and 5 s^{-1} are represented in Figure 62a. These thresholds were selected to better identify the

regions of low and very low persistent shear rates, where red blood cell aggregation is expected to be more pronounced with a consequent increase in viscosity (in the real case) and clotting. As shown in Figure 63b, flow conditions that promote blood thickening and clotting are more likely to occur in specific regions. These high-risk regions are extremely reduced (less than 5% of the LAA surface experience constant SSR below 5 s^{-1}) and confined at the distal portion of the lobes for the healthy case, but occupy over 55% under acute AF conditions. This confirms that the active contraction of the LAA plays a clear and marked role in the correct haemodynamics of the region, allowing adequate washing and reducing the risk of clot formation. The maps of risk also demonstrate the crucial role played by the lobes (Figure 63a) and knees (see yellow regions in Figure 63b) in establishing low shear rates.

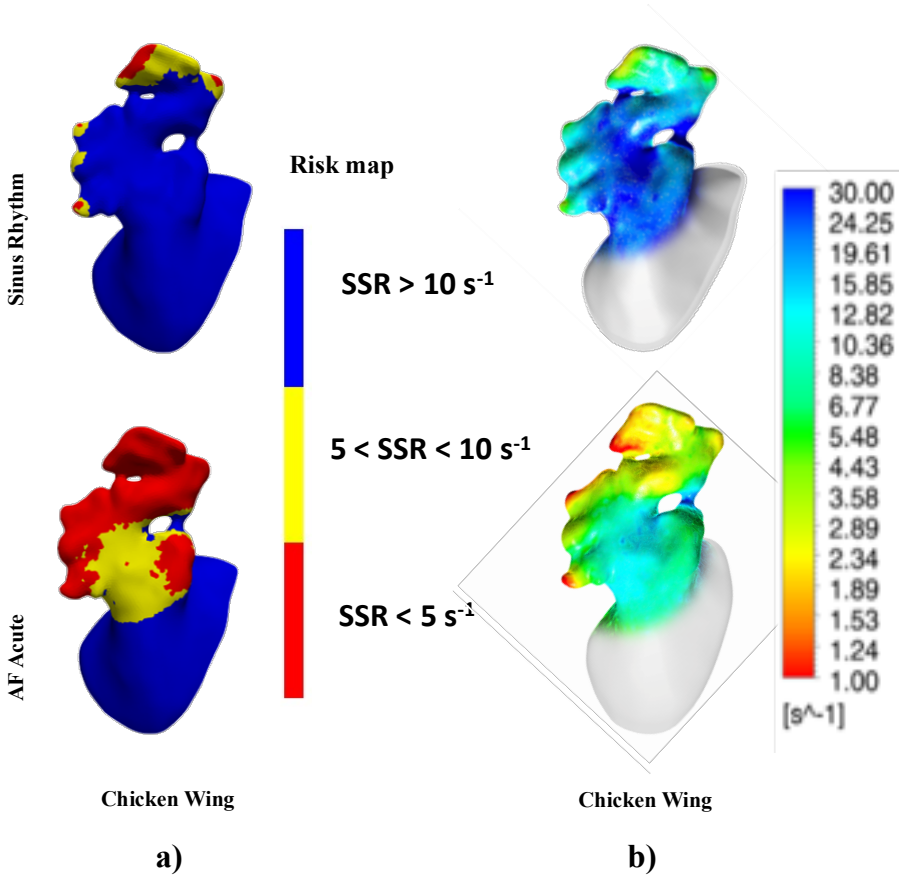

Figure 62 – a) Risk area maps in Sinus and AF conditions; b) SSR maps of the maximum wall SSR at the instant of the cycle when they reach the maximum value

5.2.3 Thrombus modelling in the patient-specific left atrial appendage

In the study of FSI simulation applied to LAA patients-specific models (above described) [25], it was demonstrated that active contractility of the left atrial appendage muscle wall ensures physiologically healthy flow, and its impairment caused by AF conditions is the major factor resulting in thromboembolic risk-related hemodynamic conditions.

Considering this, the next step was to model the formation and growth of the thrombus inside the LAA using the monolithic solver described in the previous chapters. Thus, it was necessary to write a script for transferring results obtained from Ansys FSI simulations to PANORMUS SPH simulations.

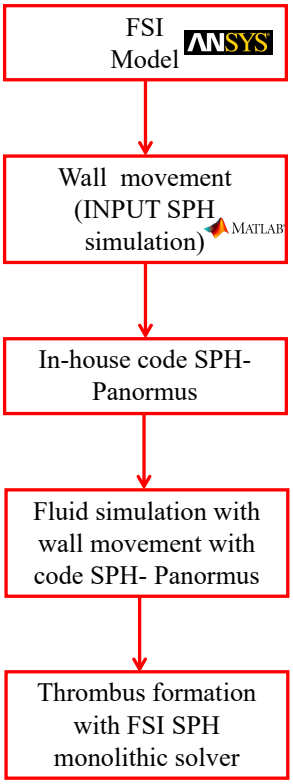

Figure 63 – Flowchart of Ansys coupling with Monolithic SPH solver

As described in the flowchart represented in Figure 63, LAA's wall movement as results of Ansys simulation must be reproduced in SPH simulation. The script is realised using MATLAB [96] and reported in Appendix A. It can be summarised in the following steps:

1. definitions of geometry, the temporal duration and a time step of Ansys FSI simulation;

2. all coordinates (x, y, z) of the nodes of the triangles discretising the LAA surface are extrapolated (inlet, wall);
3. run the MATLAB script (see Appendix A) and save the files (.txt format) that contain the coordinates of the moving wall nodes;
4. LAA's wall nodes movement (.txt files) is an input for SPH simulation.

A new subroutine has been created to transfer information between Ansys output and PANORMUS SPH code (named *Update wall deforming*). The subroutine made is divided into different phases described below:

1. Temporal identification of current time (t_n): the current time of the simulation t_r is compared to the cycle time T_c thus $t_n = t_r - T_c$ when t_r is > T_c;

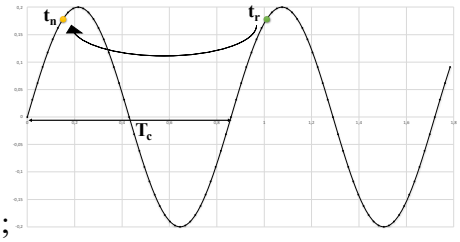

;

2. Reading wall deforming files: reading and choosing Ansys result output files considering the time before (t_1) and after (t_2) the simulated time. $t_1 < t_n < t_2$

3. Wall node position calculation: once the files and times are identified, it is possible to interpolate the node positions of the wall at t_1 and t_2, based on the current time;

4. Wall velocity computation: at each triangle, the velocities are calculated as the average of the velocities of the three nodes (as shown in Figure 64).

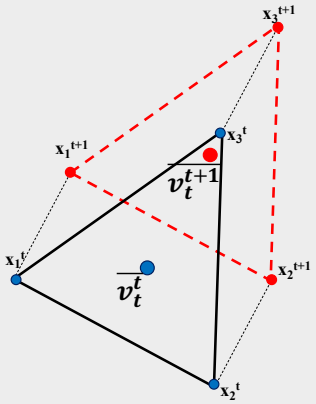

Figure 64 – Sketch of the velocity of a triangle: blue are nodes at time instant t; red is used to describe nodes at next instant t+1.

It is important to underline that the above-mentioned procedure is iteratively repeated for each instant and for each wall particle. The diagram in Figure 65 shows the steps that the SPH solver performs to simulate the formation and growth of the thrombus within a moving atrial appendage.

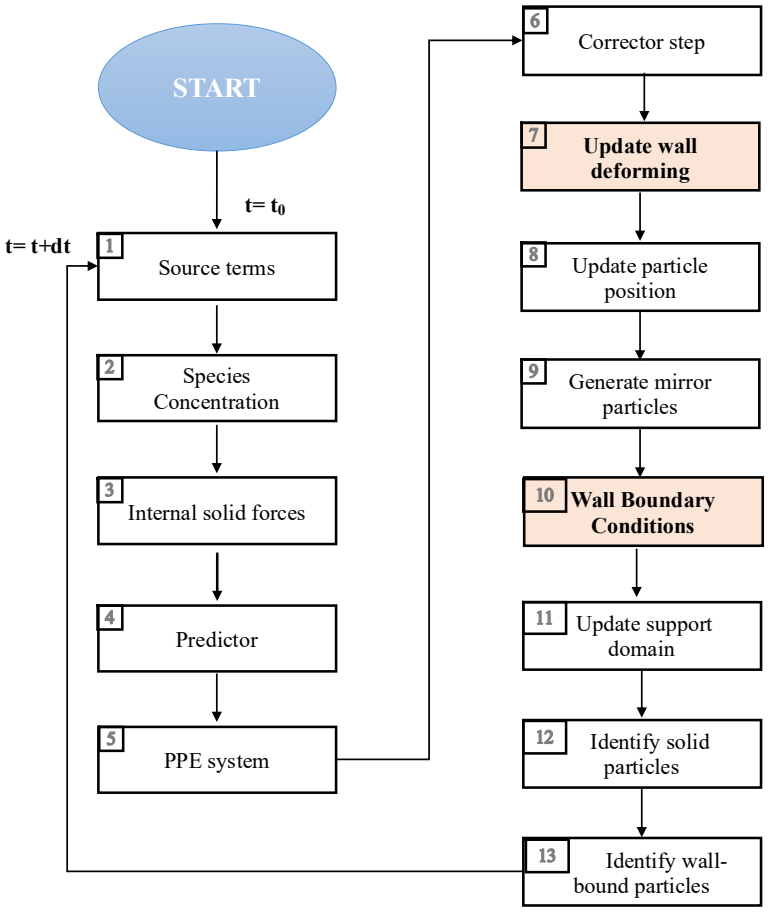

Figure 65 - Action of the SPH code to simulate thrombus formation in (orange boxes represent actions about LAA wall movement)

5.2.4 Thrombus formation and growth in chicken wing LAA: a case study.

This paragraph focuses on the numerical simulation of thrombus formation in a LAA patient-specific model. The chicken wings shape, which is the most common LAA morphology [92] is considered for this numerical study. According to what was discussed above, the input of SPH simulation is the result of the FSI study simulated with Ansys, as presented in section 5.2.2. In order to provide clarity and completeness, the following Table 3 presents the main settings adopted in Ansys simulation.

Chicken wing model	
Mesh density	70 element/mm^3
Number of inlet nodes	4716
Number of wall nodes	11424
Time cycle	0.86 s
Time step	0.0215 s

Table 3 – Data setup of Ansys System Coupling (CFX & Transient Structural)

A smoothing length h = 5×10^{-4} m was set with a total number of particles at the beginning N_e = 571 060.

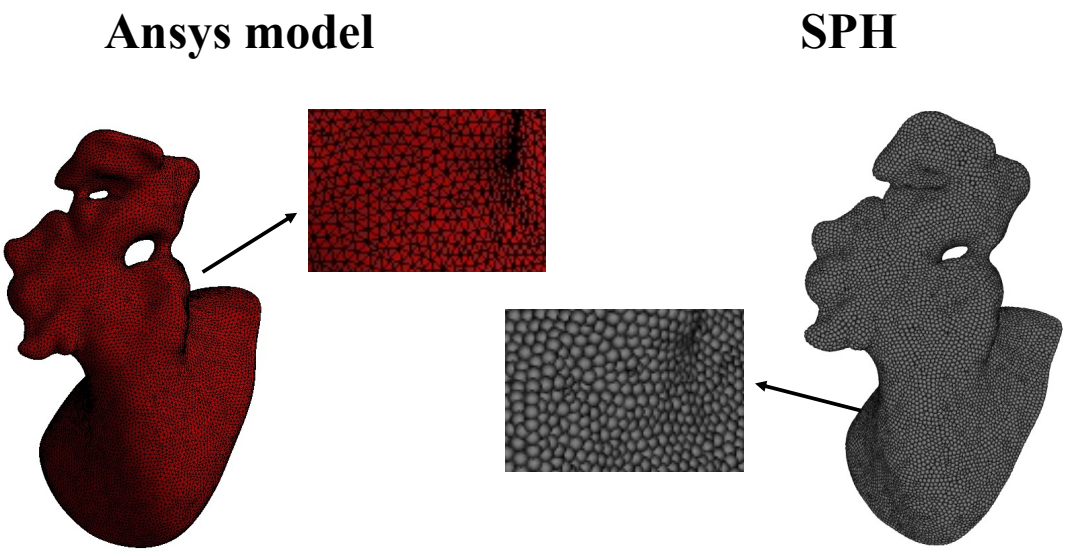

Figure 66 – Chicken wing LAA model (from ANSYS to SPH domain) with An enlargement of mesh and SPH points

In this case study, blood was modelled as an incompressible Newtonian fluid in a laminar flow regime. The fluid density and dynamic viscosity were set to 1,060 kg/m^3 and 0.004 Pa·s, respectively, corresponding to a kinematic viscosity $\nu = 3.77\times10^{-6}$ m$^{2/}$s.

As discussed in Figure 65, the fourth step involves simulating the fluid dynamics into the LAA under physiological conditions (sinus) and atrial fibrillation. Several cycles (with period T_{cycle} = 0.86 s) were performed before obtaining a stable simulation. The results (considering physiological conditions) are reported in Figure 67, where the velocity field is shown. The red outline of the LAA represents its maximal expansion at 0.43 s (mid-cycle). The other four images, taken at different times, show the appendage contracting and expanding phases. The maximum value of wall velocity is at 0.7095 s.

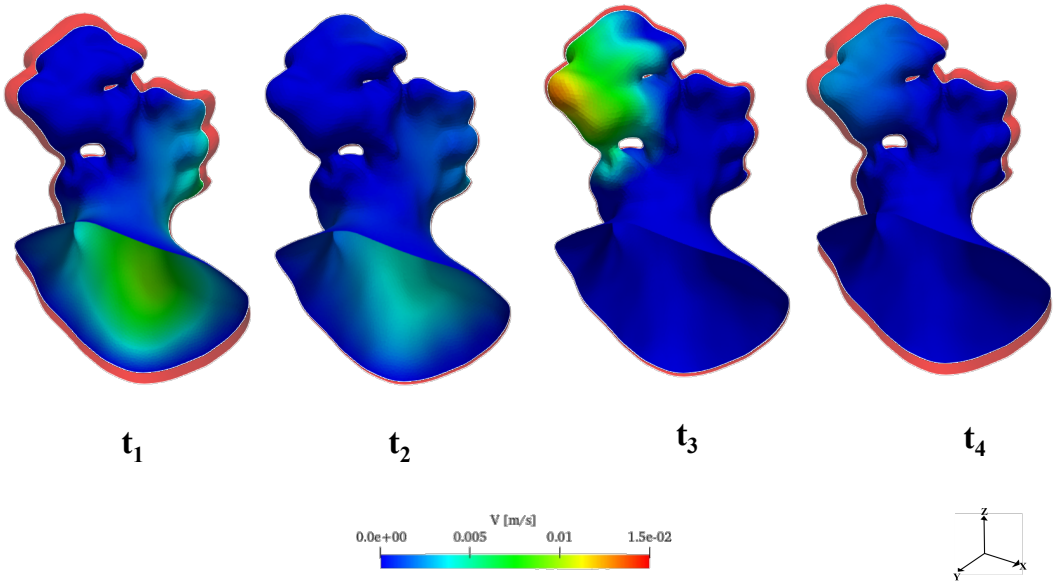

Figure 67 – LAA wall velocity at t_1=0.0215 s; t_2=0.3225 s, t_3=0.7095 s and t_4=0.8325 s

Unlike the physiological case, in atrial fibrillation conditions, no movement of the wall is clearly visible. From a fluid dynamic point of view, stasis of the blood flow and a corresponding increase in the hypercoagulability of the blood can be noted. According to [97], there is increasingly strong evidence for the presence of a prothrombotic or hypercoagulable state in atrial fibrillation. This condition was reproduced in simulation considering an initial concentration of thrombin equal to 9.11×10^{-8} mol/m^3. The values of other species concentrations are the same as reported in section 4.4. Also in this case, since thrombosis is a very slow phenomenon, the simulation was speeded up through an amplifying coefficient for thrombin, one of the

key parameters used in the computational model presented in this thesis.[6] A threshold value of 1 s^{-1} was chosen for SSR, in order to emphasise the stasis of atrial fibrillation and the absence of blood washing out. It allows thrombin and other clotting factors to be released at the site of growth. Figure 68-70 show thrombin concentration during different time instants. The first considers the entire volume of the LAA, while the second uses a section to see the concentration trend more clearly.

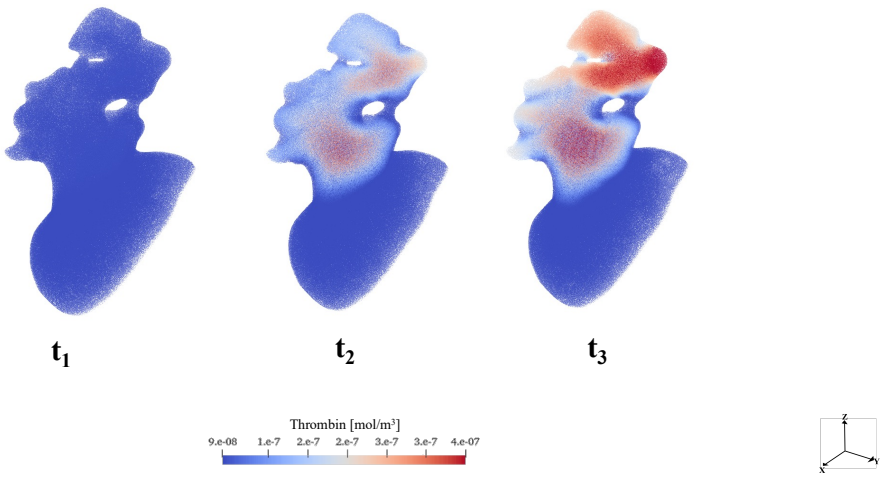

Figure 68- Thrombin concentration in chicken wing model at time instants t_1=0.0215 s, t_2=2.15 s and t_3=4.3 s

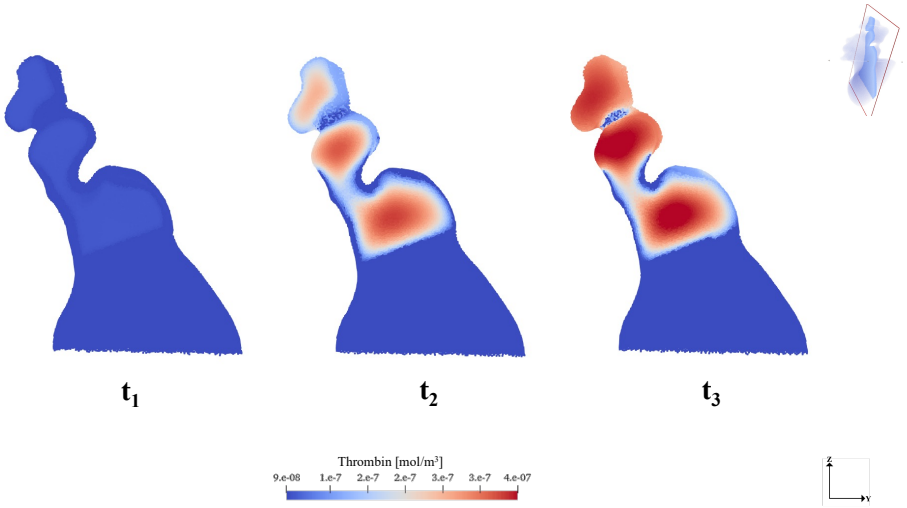

Figure 69 - Thrombin concentration in a section of LAA at time instants t_1=0.0215,; t_2=2.15 s and t_3=4.3 s

[6] An amplification value equal to 10^5 was employed for the diffusive coefficient and source term of thrombin. Moreover, this coefficient was related to the SSR by applying it to particles having SSR lower that an imposed threshold value.

After several cycles, the simulation was performed until the thrombin reached the limit value to activate the platelets and subsequently form the bound platelets (see section 4.1 and eqns 4.14-4.15).

The graph in Figure 70 shows the temporal growth of the thrombus in the LAA. The thrombus begins to form at about 4 seconds, and in successive time instants a rapid growth can be seen up to a stabilisation, that represents the greatest growth up to 5.6 seconds. The percentage of occluded thrombus is calculated from the ratio of the total particles of the appendage to the percentage of particles labelled as thrombus.

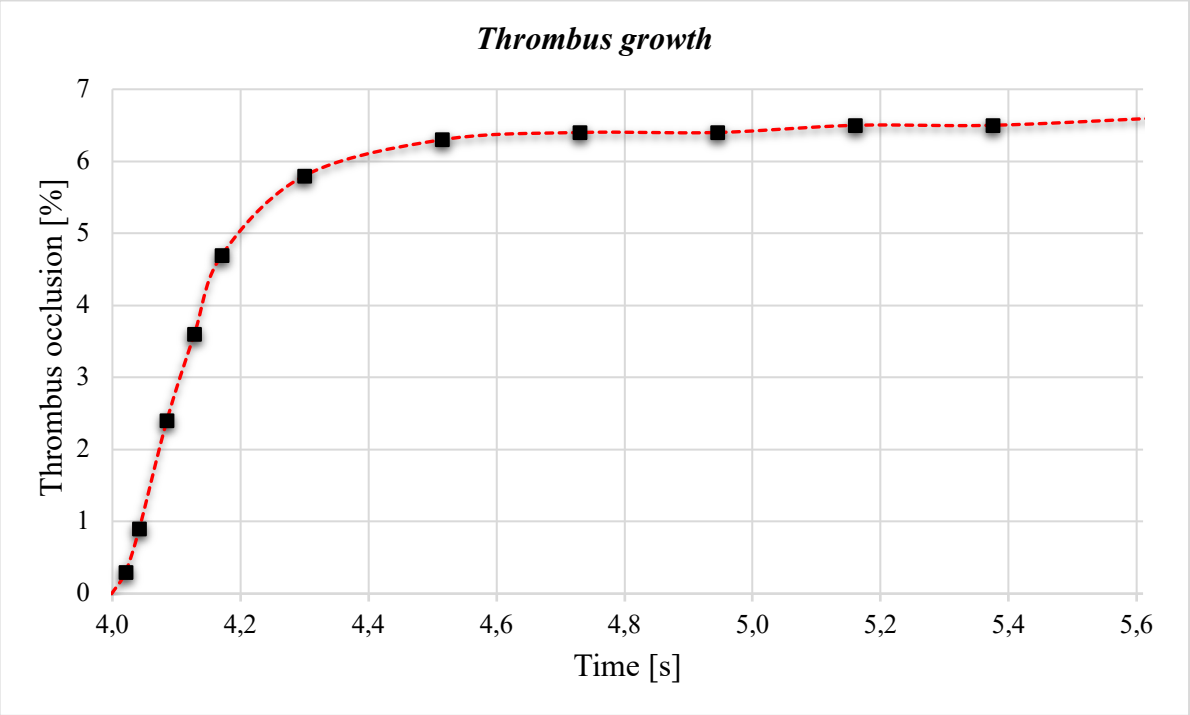

Figure 70 – Thrombus growth in LAA between 4-6 seconds

The evolution of the thrombus formation in the LAA under atrial fibrillation is shown in Figure 71. As it can be observed, a thrombus starts to form from the LAA tip and progressively growths towards the orifice. This finding is in agreement with the results of [25], where the obtained thromboembolic risk maps confirm an inadequate blood washout at the LAA end, lobes and trabeculae, which are recognised as regions likely to promote clot formation.

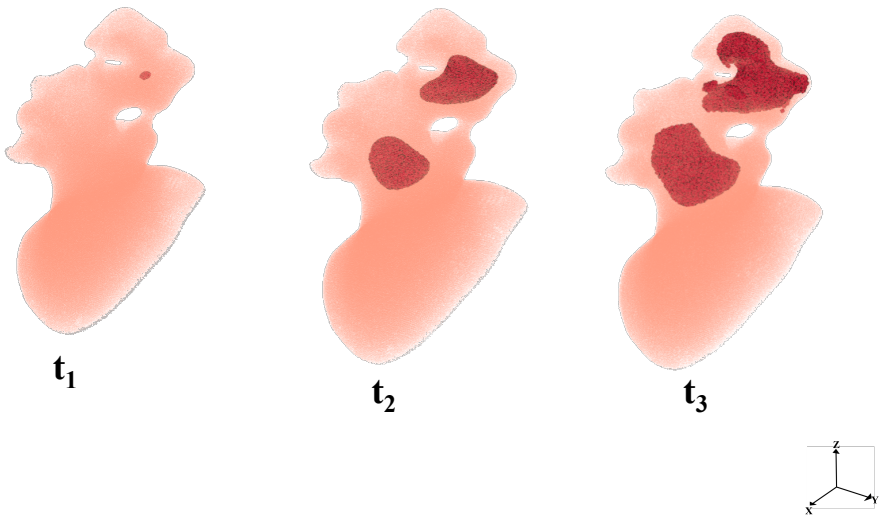

Figure 71 - Thrombus formation in a patient-specific LAA (t_1=3.99 s; t_2=4.12 s; t_3=5.63 s)

5.3 Conclusions

In this chapter, two application cases of the numerical model of thrombus formation using the sph method have been presented.

The results of the performed numerical simulations clearly show that thrombus formation in an idealised geometry of a cerebral aneurysm is a complex interaction between hemodynamic and biochemical factors. It can be noted in both cases that the areas in which the thrombus has developed are the areas in which the speed in hydrodynamic conditions has very low values.

A more complex study was performed in the evaluation of thrombus formation and growth in the left atrial appendage. The use of a patient-specific geometry has made it possible to simulate a pathology that often afflicts people suffering from atrial fibrillation. Also, it was discovered that the thrombogenic regions—those with low SSR values and stasis—are where the thrombus forms and develops. Additionally, the atrial appendage's trabeculae and lobes favour a blood flow rate that allows less washing of these regions and, as a result, a longer reaction time for the available biochemical variables.

Chapter 6

6. Conclusions and future works

Thrombosis phenomena is the core of this work. The main objective was to create an accurate, reliable and adaptable platform to analyse thrombosis in different pathologies, based on a careful analysis of the current numerical methods. In this thesis, a more accurate model for thrombus assessment was implemented by integrating hydrodynamic parameters such as shear stress and coagulation factors (biological and chemical). Computational fluid dynamics can be a powerful tool for simulating haemodynamics in patient-specific models. Numerical tools may help to evaluate the impact of various clinical interventions and to identify hemodynamic factors affecting treatment outcomes.

The study has implemented a new an SPH numerical method to model thrombosis formation. Due to its Lagrangian nature, SPH is able to ease up the treatment of geometrically complex domains such as LAA. In order to analyse thrombus growth and dissolution, the open-source code PANORMUS-SPH was used.

The presented method is able to realistically describe the thrombosis phenomenon, including blood clotting variables (platelets, coagulative cascade enzymes), hydrodynamic parameters (shear strain rate and velocity) and mutual interactions between fluid dynamics of blood and the progression in thrombus growth. Differently from the partitioned FSI approach, in the proposed technique, no interface is requested and an intrinsic coupling between fluid and solid phases is performed, saving computational costs.

The mathematical model proposed was applied to a wide range of clinical situations in which thrombosis occurs. Firstly, to describe how thrombosis in giant cerebral aneurysms develops, where hemodynamic and biochemical factors interact to promote its development. Secondly, to determine how changes in blood flow may promote blood clots. As with the insertion of the flow diverter to treat small cerebral aneurysms. This last case also presents another important novelty. It was adapted and

modified to simulate the flow diverter with fixed particles using the same FSI SPH monolithic solver, reducing computation costs significantly.

Another case study regards thrombi formation in LAA in atrial fibrillation. Starting from the results previously obtained (identification of the maps of greater thromboembolic risk), the code was able to simulate the growth of the thrombus in the various areas of the appendage. It is also important to emphasize the novelty of this code, which, through the development of a MATLAB-based stand-alone code, can be coupled with a variety of solvers, allowing information to be exchanged for a more realistic pathology simulation.

Anyway, the present study involves several limitations, which should be addressed in order to refine predictions. Some of the major limitations of this work are discussed below, with suggestions for future work.

As for thrombosis in cerebral aneurysm, the geometric models used are based on idealised geometries. This provides limitations because, as described in the literature, aneurysm findings are sensitive to small changes in size and location. For this reason, the next step of the work is using patient-specific models that can be obtained from imaging techniques.

Another limitation is due to the fact that blood has been modeled as a Newtonian fluid, the use of non-Newtonian fluid models could lead to more accurate solutions. In fact, such modelling is reasonable in low-shear rate regions such as recirculation zones, vortex structures and flow stagnation zones. Future work could be directed towards the non-Newtonian characterization of blood, perhaps integrating into the PANORMUS code a mathematical model that can simulate the thixotropy of blood, starting from data obtained experimentally.

Regarding the study of thrombosis in the atrial appendage, the model was applied only to the chicken wing morphology. Surely by adopting different morphologies and simulating different clinical cases, more information on the formation and growth of thrombi in the appendages can be obtained. Moreover, this study should make it possible to establish a stronger link between thromboembolic risk and haemodynamic variables such as velocity or SSR.

The modelling of thrombus dissolution could be subjected to further improvement. In fact, only the distance between the active particles—which must be greater than a threshold value is taken into account when lysis of the thrombus occurs. Linking thrombus dissolution to biochemical factors like fibrin concentration could be

a significant upgrade. Numerous investigations have shown that thrombus lysis happens when a concentration limit value is exceeded. This could improve how accurately the code simulates the entire process.

Further investigation could address about pharmacological treatment of the thrombosis as a potential development of the proposed model. Specifically, analysing the drug impact about thrombosis lysis or studying new therapeutic treatments.

Furthermore, as a consequence of its simplicity and flexibility, the approach can be implemented into a new tool supporting the design of safer and more effective medical devices and, in future, the accurate modelling of several pathologies as case studies would provide further clarifications and indications for the mitigation and treatment of these pathologies.

Appendix A

The script below was written using MATLAB software. The tool is intended to read the results (output data) of the ANSYS FSI (structural and CFX) simulations as well as transform this information (movement of the walls) into input data (reading them as contour files) for the SPH simulation.

```
clear all;close all;clc

   1) Boudary file ------------------------------------------------
      ----------
n_inlet = 4716; % to modify
n_wall = 11424; % to modify

% Reading nodes inlet coordinates
nodes_inlet = csvread('..\triangle_inlet.csv',6,0,[6 0 n_inlet-1
2]);

% Reading nodes coordinates wall deforming
nodes_wall = csvread('..\triangle_wall.csv',6,0,[6 0 n_wall-1 2]);

% Reading triangle inlet
ind_inlet = csvread('..\triangle_inlet.csv',n_inlet+2,0);

% Reading triangle wall
ind_wall = csvread('..\triangle_wall.csv',n_wall+2,0);

% Print initial boundary file
fileID = fopen('boundary.inp','w');

% Print coordinates nodes inlet
 for i = 1:length(nodes_inlet)
     fprintf(fileID,'%e %e %e\n',nodes_inlet(i,1:3));
 end

 % Print coordinates nodes wall deforming
  for i = 1:length(nodes_wall)
     fprintf(fileID,'%e %e %e\n',nodes_wall(i,1:3));
  end


 string = '';
 fprintf(fileID,'%s\n',string);

 % Print index triangle inlet
  for i = 1:length(ind_inlet)
     n1 = ind_inlet(i,1)+1;
     n2 = ind_inlet(i,3)+1;
     n3 = ind_inlet(i,2)+1;
     fprintf(fileID,'%i %i %i %i\n',n1,n2,n3,0);
     string = 'pressure';
     fprintf(fileID,'%s\n',string);
     fprintf(fileID,'%e %e %e\n',0.00,0.00,0.00);
     string = '';
     fprintf(fileID,'%s\n',string);
  end
```

```
   % Print index triangle wall deforming
  for i = 1:length(ind_wall)
     n1 = ind_wall(i,1)+1+length(nodes_inlet);
     n2 = ind_wall(i,3)+1+length(nodes_inlet);
     n3 = ind_wall(i,2)+1+length(nodes_inlet);
     fprintf(fileID,'%i %i %i %i\n',n1,n2,n3,1);
     string = 'adherence';
     fprintf(fileID,'%s\n',string);
     fprintf(fileID,'%e %e %e\n',0.00,0.00,0.00);
     string = '';
     fprintf(fileID,'%s\n',string);
  end

fclose(fileID);
% ------------------------------------------------------------------
-------

   2) Nodes wall_deforming (in the time) --------------------------
      ----------------
% Reading csv files for all nodes of "wall_deforming"
files = dir('*.csv');
num_files = length(files);
results = cell(length(files), 1);

for i = 1:num_files
  results{i} = csvread(files(i).name,6,0);

  x(i,:) = results{i}(1:end,1);
  y(i,:) = results{i}(1:end,2);
  z(i,:) = results{i}(1:end,3);
end


for t = 1:num_files
    j = t-1;
    fileID = fopen(sprintf('wall_%d.txt',j),'wt');

    for n = 1:length(nodes_wall)
        fprintf(fileID,'%e %e %e\n',x(t,n),y(t,n),z(t,n));
    end
    fclose(fileID);
end
```

Publications

The publications during the PhD program are listed as follows.

1) A. Monteleone, A. Viola, E. Napoli, e G. Burriesci, «Modelling of thrombus formation using smoothed particle hydrodynamics method», *PLOS ONE*, vol. 18, fasc. 2, p. e0281424, feb. 2023;

2) Musotto G., Monteleone A, Vella D., Di Leonardo S., Viola A., Pitarresi G., Zuccarello B., Pantano A., Cook A., Bosi, G. M., Burriesci, G., «The Role of Patient-Specific Morphological Features of the Left Atrial Appendage on the Thromboembolic Risk Under Atrial Fibrillation», *Front. Cardiovasc. Med.*, vol. 9, p. 894187, lug. 2022, doi: 10.3389/fcvm.2022.894187.

References

[1] A. M. Wendelboe e G. E. Raskob, «Global Burden of Thrombosis: Epidemiologic Aspects», *Circ. Res.*, vol. 118, fasc. 9, pp. 1340–1347, apr. 2016, doi: 10.1161/CIRCRESAHA.115.306841.

[2] N. M. Cheng, Y. C. Chan, e S. W. Cheng, «COVID-19 related thrombosis: A mini-review», *Phlebol. J. Venous Dis.*, vol. 37, fasc. 5, pp. 326–337, giu. 2022, doi: 10.1177/02683555211052170.

[3] Rodrigo Mendez Rojano, «Thrombosis modeling in blood coated medical devices», Université Montpellier, 2018.

[4] G. A. Roth *et al.*, «Global Burden of Cardiovascular Diseases and Risk Factors, 1990–2019», *J. Am. Coll. Cardiol.*, vol. 76, fasc. 25, pp. 2982–3021, dic. 2020, doi: 10.1016/j.jacc.2020.11.010.

[5] J. Sun, Y. Qiao, M. Zhao, C. G. Magnussen, e B. Xi, «Global, regional, and national burden of cardiovascular diseases in youths and young adults aged 15–39 years in 204 countries/territories, 1990–2019: a systematic analysis of Global Burden of Disease Study 2019», *BMC Med.*, vol. 21, fasc. 1, p. 222, giu. 2023, doi: 10.1186/s12916-023-02925-4.

[6] D. M. Siegal *et al.*, «A toolkit for the collection of thrombosis-related data elements in COVID-19 clinical studies», *Blood Adv.*, vol. 4, fasc. 24, pp. 6259–6273, dic. 2020, doi: 10.1182/bloodadvances.2020003269.

[7] K. E. Brummel-Ziedins, T. Orfeo, P. W. Callas, M. Gissel, K. G. Mann, e E. G. Bovill, «The Prothrombotic Phenotypes in Familial Protein C Deficiency Are Differentiated by Computational Modeling of Thrombin Generation», *PLoS ONE*, vol. 7, fasc. 9, p. e44378, set. 2012, doi: 10.1371/journal.pone.0044378.

[8] Virchow R., «Gesammelte abhandlungen zur wissenschaftlichen medicin.tle.», 1856.

[9] F. Khan, C. Vaillancourt, e G. Bourjeily, «Diagnosis and management of deep vein thrombosis in pregnancy», *BMJ*, p. j2344, mag. 2017, doi: 10.1136/bmj.j2344.

[10] N. Woolf, *Pathology: basic and systemic*. London: Saunders, 1998.

[11] T. Bodnár, A. Fasano, e A. Sequeira, «Mathematical Models for Blood Coagulation», in *Fluid-Structure Interaction and Biomedical Applications*, T. Bodnár, G. P. Galdi, e Š. Nečasová, A c. di, in Advances in Mathematical Fluid Mechanics. ,

Basel: Springer Basel, 2014, pp. 483–569. doi: 10.1007/978-3-0348-0822-4_7.

[12] S. Cito, M. D. Mazzeo, e L. Badimon, «A Review of Macroscopic Thrombus Modeling Methods», *Thromb. Res.*, vol. 131, fasc. 2, pp. 116–124, feb. 2013, doi: 10.1016/j.thromres.2012.11.020.

[13] P. D. Stein, H. N. Sabbah, e J. V. Pitha, «Continuing disease process of calcific aortic stenosis», *Am. J. Cardiol.*, vol. 39, fasc. 2, pp. 159–163, feb. 1977, doi: 10.1016/S0002-9149(77)80185-9.

[14] J. D. Hellums, «1993 Whitaker lecture: Biorheology in thrombosis research», *Ann. Biomed. Eng.*, vol. 22, fasc. 5, pp. 445–455, set. 1994, doi: 10.1007/BF02367081.

[15] A. Sarrami-Foroushani, T. Lassila, S. M. Hejazi, S. Nagaraja, A. Bacon, e A. F. Frangi, «A computational model for prediction of clot platelet content in flow-diverted intracranial aneurysms», *J. Biomech.*, vol. 91, pp. 7–13, giu. 2019, doi: 10.1016/j.jbiomech.2019.04.045.

[16] D. L. Bark, A. N. Para, e D. N. Ku, «Correlation of thrombosis growth rate to pathological wall shear rate during platelet accumulation», *Biotechnol. Bioeng.*, vol. 109, fasc. 10, pp. 2642–2650, ott. 2012, doi: 10.1002/bit.24537.

[17] J. Biasetti, F. Hussain, e T. C. Gasser, «Blood flow and coherent vortices in the normal and aneurysmatic aortas: a fluid dynamical approach to intra-luminal thrombus formation», *J. R. Soc. Interface*, vol. 8, fasc. 63, pp. 1449–1461, ott. 2011, doi: 10.1098/rsif.2011.0041.

[18] J. F. Wendt, J. D. Anderson, e Von Karman Institute for Fluid Dynamics, A c. di, *Computational fluid dynamics: an introduction*, 3rd ed. Berlin ; [London]: Springer, 2008.

[19] E. H. Dowell e K. C. Hall, «M ODELING OF F LUID -S TRUCTURE I NTERACTION», *Annu. Rev. Fluid Mech.*, vol. 33, fasc. 1, pp. 445–490, gen. 2001, doi: 10.1146/annurev.fluid.33.1.445.

[20] E. N. Sorensen, G. W. Burgreen, W. R. Wagner, e J. F. Antaki, «Computational Simulation of Platelet Deposition and Activation: I. Model Development and Properties», *Ann. Biomed. Eng.*, vol. 27, fasc. 4, pp. 436–448, lug. 1999, doi: 10.1114/1.200.

[21] K. Leiderman e A. L. Fogelson, «Grow with the flow: a spatial-temporal model of platelet deposition and blood coagulation under flow», *Math. Med. Biol.*, vol. 28, fasc. 1, pp. 47–84, mar. 2011, doi: 10.1093/imammb/dqq005.

[22] M. Anand, K. Rajagopal, e K. R. Rajagopal, «A Model for the Formation and Lysis of Blood Clots», *Pathophysiol. Haemost. Thromb.*, vol. 34, fasc. 2–3, pp. 109–120, 2005, doi: 10.1159/000089931.

[23] C. Menichini e X. Y. Xu, «Mathematical modeling of thrombus formation in idealized models of aortic dissection: initial findings and potential applications», *J. Math. Biol.*, vol. 73, fasc. 5, pp. 1205–1226, nov. 2016, doi: 10.1007/s00285-016-0986-4.

[24] D. Vella, A. Monteleone, G. Musotto, G. M. Bosi, e G. Burriesci, «Effect of the Alterations in Contractility and Morphology Produced by Atrial Fibrillation on the Thrombosis Potential of the Left Atrial Appendage», *Front. Bioeng. Biotechnol.*, vol. 9, p. 586041, feb. 2021, doi: 10.3389/fbioe.2021.586041.

[25] G. Musotto *et al.*, «The Role of Patient-Specific Morphological Features of the Left Atrial Appendage on the Thromboembolic Risk Under Atrial Fibrillation», *Front. Cardiovasc. Med.*, vol. 9, p. 894187, lug. 2022, doi: 10.3389/fcvm.2022.894187.

[26] C. Farhat e M. Lesoinne, «Two efficient staggered algorithms for the serial and parallel solution of three-dimensional nonlinear transient aeroelastic problems», *Comput. Methods Appl. Mech. Eng.*, vol. 182, fasc. 3–4, pp. 499–515, feb. 2000, doi: 10.1016/S0045-7825(99)00206-6.

[27] M. Souli, A. Ouahsine, e L. Lewin, «ALE formulation for fluid–structure interaction problems», *Comput. Methods Appl. Mech. Eng.*, vol. 190, fasc. 5–7, pp. 659–675, nov. 2000, doi: 10.1016/S0045-7825(99)00432-6.

[28] E. Kuhl, S. Hulshoff, e R. de Borst, «An arbitrary Lagrangian Eulerian finite-element approach for fluid-structure interaction phenomena», *Int. J. Numer. Methods Eng.*, vol. 57, fasc. 1, pp. 117–142, mag. 2003, doi: 10.1002/nme.749.

[29] G. Lipari e E. Napoli, «The impacts of the ALE and hydrostatic-pressure approaches on the energy budget of unsteady free-surface flows», *Comput. Fluids*, vol. 37, fasc. 6, pp. 656–673, lug. 2008, doi: 10.1016/j.compfluid.2007.10.005.

[30] C. S. Peskin, «The immersed boundary method», *Acta Numer.*, vol. 11, pp. 479–517, gen. 2002, doi: 10.1017/S0962492902000077.

[31] Th. Dunne, «An Eulerian approach to fluid–structure interaction and goal-oriented mesh adaptation», *Int. J. Numer. Methods Fluids*, vol. 51, fasc. 9–10, pp. 1017–1039, lug. 2006, doi: 10.1002/fld.1205.

[32] T. Richter, «A Fully Eulerian formulation for fluid–structure-

interaction problems», *J. Comput. Phys.*, vol. 233, pp. 227–240, gen. 2013, doi: 10.1016/j.jcp.2012.08.047.

[33] J. Fan *et al.*, «A monolithic Lagrangian meshfree scheme for Fluid–Structure Interaction problems within the OTM framework», *Comput. Methods Appl. Mech. Eng.*, vol. 337, pp. 198–219, ago. 2018, doi: 10.1016/j.cma.2018.03.031.

[34] P. B. Ryzhakov, R. Rossi, S. R. Idelsohn, e E. Oñate, «A monolithic Lagrangian approach for fluid–structure interaction problems», *Comput. Mech.*, vol. 46, fasc. 6, pp. 883–899, nov. 2010, doi: 10.1007/s00466-010-0522-0.

[35] A. Franci, E. Oñate, e J. M. Carbonell, «Unified Lagrangian formulation for solid and fluid mechanics and FSI problems», *Comput. Methods Appl. Mech. Eng.*, vol. 298, pp. 520–547, gen. 2016, doi: 10.1016/j.cma.2015.09.023.

[36] D. S. Morikawa e M. Asai, «Coupling total Lagrangian SPH–EISPH for fluid–structure interaction with large deformed hyperelastic solid bodies», *Comput. Methods Appl. Mech. Eng.*, vol. 381, p. 113832, ago. 2021, doi: 10.1016/j.cma.2021.113832.

[37] C. Antoci, M. Gallati, e S. Sibilla, «Numerical simulation of fluid–structure interaction by SPH», *Comput. Struct.*, vol. 85, fasc. 11–14, pp. 879–890, giu. 2007, doi: 10.1016/j.compstruc.2007.01.002.

[38] M. Toma, «The Emerging Use of SPH In Biomedical Applications», *Significances Bioeng. Biosci.*, vol. 1, fasc. 1, ott. 2017, doi: 10.31031/SBB.2017.01.000502.

[39] S. Shahriari e L. Kadem, «Smoothed Particle Hydrodynamics Method and Its Applications to Cardiovascular Flow Modeling», in *Numerical Methods and Advanced Simulation in Biomechanics and Biological Processes*, Elsevier, 2018, pp. 203–219. doi: 10.1016/B978-0-12-811718-7.00011-3.

[40] Y.-P. Chui e P.-A. Heng, «A meshless rheological model for blood-vessel interaction in endovascular simulation», *Prog. Biophys. Mol. Biol.*, vol. 103, fasc. 2–3, pp. 252–261, dic. 2010, doi: 10.1016/j.pbiomolbio.2010.09.003.

[41] M. Al-Saad, C. A. Suarez, A. Obeidat, S. P. A. Bordas, e S. Kulasegaram, «Application of Smooth Particle Hydrodynamics Method for Modelling Blood Flow with Thrombus Formation», *Comput. Model. Eng. Sci.*, vol. 122, fasc. 3, pp. 831–862, 2020, doi: 10.32604/cmes.2020.08527.

[42] M. B. Liu e G. R. Liu, «Smoothed Particle Hydrodynamics (SPH): an Overview and Recent Developments», *Arch. Comput. Methods Eng.*, vol. 17, fasc. 1,

pp. 25–76, mar. 2010, doi: 10.1007/s11831-010-9040-7.

[43] E. Napoli, M. De Marchis, e E. Vitanza, «PANORMUS-SPH. A new Smoothed Particle Hydrodynamics solver for incompressible flows», *Comput. Fluids*, vol. 106, pp. 185–195, gen. 2015, doi: 10.1016/j.compfluid.2014.09.045.

[44] Monteleone Alessandra, «SPH modeling of blood flow in cerebral aneurysms», Università degli Studi di Palermo, 2019.

[45] F. Roman, E. Napoli, B. Milici, e V. Armenio, «An improved immersed boundary method for curvilinear grids», *Comput. Fluids*, vol. 38, fasc. 8, pp. 1510–1527, set. 2009, doi: 10.1016/j.compfluid.2008.12.004.

[46] S. J. Lind, R. Xu, P. K. Stansby, e B. D. Rogers, «Incompressible smoothed particle hydrodynamics for free-surface flows: A generalised diffusion-based algorithm for stability and validations for impulsive flows and propagating waves», *J. Comput. Phys.*, vol. 231, fasc. 4, pp. 1499–1523, feb. 2012, doi: 10.1016/j.jcp.2011.10.027.

[47] A. J. Chorin, «Numerical solution of the Navier-Stokes equations», *Math. Comput.*, vol. 22, fasc. 104, pp. 745–762, 1968, doi: 10.1090/S0025-5718-1968-0242392-2.

[48] *Solving Ordinary Differential Equations I*, vol. 8. in Springer Series in Computational Mathematics, vol. 8. Berlin, Heidelberg: Springer Berlin Heidelberg, 1993. doi: 10.1007/978-3-540-78862-1.

[49] R. Xu, P. Stansby, e D. Laurence, «Accuracy and stability in incompressible SPH (ISPH) based on the projection method and a new approach», *J. Comput. Phys.*, vol. 228, fasc. 18, pp. 6703–6725, ott. 2009, doi: 10.1016/j.jcp.2009.05.032.

[50] A. Monteleone, A. Viola, E. Napoli, e G. Burriesci, «Modelling of thrombus formation using smoothed particle hydrodynamics method», *PLOS ONE*, vol. 18, fasc. 2, p. e0281424, feb. 2023, doi: 10.1371/journal.pone.0281424.

[51] J. Rosing, J. van Rijn, E. Bevers, G. van Dieijen, P. Comfurius, e R. Zwaal, «The role of activated human platelets in prothrombin and factor X activation», *Blood*, vol. 65, fasc. 2, pp. 319–332, feb. 1985, doi: 10.1182/blood.V65.2.319.319.

[52] L. Michaelis e M. L. Menten, «Die kinetik der invertinwirkung», *Biochem Z*, vol. 49, pp. 333–369, 1913.

[53] H. J. Weiss, *Platelets: Pathophysiology and Antiplatelet Drug Therapy*. Liss, 1982.

[54] «Mathematical modeling in systems biology: an introduction», *Choice Rev. Online*, vol. 51, fasc. 07, pp. 51-3830-51–3830, mar. 2014, doi: 10.5860/CHOICE.51-3830.

[55] M. Anand, K. Rajagopal, e K. R. Rajagopal, «A Model Incorporating Some of the Mechanical and Biochemical Factors Underlying Clot Formation and Dissolution in Flowing Blood», *J. Theor. Med.*, vol. 5, fasc. 3–4, pp. 183–218, 2003, doi: 10.1080/10273660412331317415.

[56] J. M. Grunkemeier, W. B. Tsai, e T. A. Horbett, «Hemocompatibility of treated polystyrene substrates: Contact activation, platelet adhesion, and procoagulant activity of adherent platelets», *J. Biomed. Mater. Res.*, vol. 41, fasc. 4, pp. 657–670, set. 1998, doi: 10.1002/(SICI)1097-4636(19980915)41:4<657::AID-JBM18>3.0.CO;2-B.

[57] M. Tsiang *et al.*, «Protein Engineering Thrombin for Optimal Specificity and Potency of Anticoagulant Activity *in Vivo*», *Biochemistry*, vol. 35, fasc. 51, pp. 16449–16457, gen. 1996, doi: 10.1021/bi9616108.

[58] K. Leiderman e A. L. Fogelson, «Grow with the flow: a spatial-temporal model of platelet deposition and blood coagulation under flow», *Math. Med. Biol.*, vol. 28, fasc. 1, pp. 47–84, mar. 2011, doi: 10.1093/imammb/dqq005.

[59] J. I. Borissoff, H. M. H. Spronk, S. Heeneman, e H. ten Cate, «Is thrombin a key player in the "coagulation-atherogenesis" maze?», *Cardiovasc. Res.*, vol. 82, fasc. 3, pp. 392–403, giu. 2009, doi: 10.1093/cvr/cvp066.

[60] M. Ranucci, T. Laddomada, M. Ranucci, e E. Baryshnikova, «Blood viscosity during coagulation at different shear rates», *Physiol. Rep.*, vol. 2, fasc. 7, p. e12065, lug. 2014, doi: 10.14814/phy2.12065.

[61] T. Bodnár e A. Sequeira, «Numerical Simulation of the Coagulation Dynamics of Blood», *Comput. Math. Methods Med.*, vol. 9, fasc. 2, pp. 83–104, 2008, doi: 10.1080/17486700701852784.

[62] H. Kamada, Y. Imai, M. Nakamura, T. Ishikawa, e T. Yamaguchi, «Computational analysis on the mechanical interaction between a thrombus and red blood cells: Possible causes of membrane damage of red blood cells at microvessels», *Med. Eng. Phys.*, vol. 34, fasc. 10, pp. 1411–1420, dic. 2012, doi: 10.1016/j.medengphy.2012.01.003.

[63] H. Kamada, K. Tsubota, M. Nakamura, S. Wada, T. Ishikawa, e T. Yamaguchi, «A three-dimensional particle simulation of the formation and collapse of

a primary thrombus», *Int. J. Numer. Methods Biomed. Eng.*, vol. 26, fasc. 3–4, pp. 488–500, mar. 2010, doi: 10.1002/cnm.1367.

[64] A. Monteleone, G. Borino, E. Napoli, e G. Burriesci, «Fluid–structure interaction approach with smoothed particle hydrodynamics and particle–spring systems», *Comput. Methods Appl. Mech. Eng.*, vol. 392, p. 114728, mar. 2022, doi: 10.1016/j.cma.2022.114728.

[65] A. Tosenberger, F. Ataullakhanov, N. Bessonov, M. Panteleev, A. Tokarev, e V. Volpert, «Modelling of platelet–fibrin clot formation in flow with a DPD–PDE method», *J. Math. Biol.*, vol. 72, fasc. 3, pp. 649–681, feb. 2016, doi: 10.1007/s00285-015-0891-2.

[66] J. O. Taylor *et al.*, «In Vitro Quantification of Time Dependent Thrombus Size Using Magnetic Resonance Imaging and Computational Simulations of Thrombus Surface Shear Stresses», *J. Biomech. Eng.*, vol. 136, fasc. 7, p. 071012, lug. 2014, doi: 10.1115/1.4027613.

[67] A. Monteleone, M. Monteforte, e E. Napoli, «Inflow/outflow pressure boundary conditions for smoothed particle hydrodynamics simulations of incompressible flows», *Comput. Fluids*, vol. 159, pp. 9–22, dic. 2017, doi: 10.1016/j.compfluid.2017.09.011.

[68] A. Monteleone, G. Burriesci, e E. Napoli, «A distributed-memory MPI parallelization scheme for multi-domain incompressible SPH», *J. Parallel Distrib. Comput.*, vol. 170, pp. 53–67, dic. 2022, doi: 10.1016/j.jpdc.2022.08.004.

[69] K. G. Link *et al.*, «A local and global sensitivity analysis of a mathematical model of coagulation and platelet deposition under flow», *PLOS ONE*, vol. 13, fasc. 7, p. e0200917, lug. 2018, doi: 10.1371/journal.pone.0200917.

[70] A. Bouchnita e V. Volpert, «A multiscale model of platelet-fibrin thrombus growth in the flow», *Comput. Fluids*, vol. 184, pp. 10–20, apr. 2019, doi: 10.1016/j.compfluid.2019.03.021.

[71] M. N. Ngoepe, A. F. Frangi, J. V. Byrne, e Y. Ventikos, «Thrombosis in Cerebral Aneurysms and the Computational Modeling Thereof: A Review», *Front. Physiol.*, vol. 9, p. 306, apr. 2018, doi: 10.3389/fphys.2018.00306.

[72] V. L. Rayz *et al.*, «Numerical Modeling of the Flow in Intracranial Aneurysms: Prediction of Regions Prone to Thrombus Formation», *Ann. Biomed. Eng.*, vol. 36, fasc. 11, pp. 1793–1804, nov. 2008, doi: 10.1007/s10439-008-9561-5.

[73] O. Malaspinas *et al.*, «A spatio-temporal model for spontaneous

thrombus formation in cerebral aneurysms», *J. Theor. Biol.*, vol. 394, pp. 68–76, apr. 2016, doi: 10.1016/j.jtbi.2015.12.022.

[74] A. Bouchnita, A. V. Belyaev, e V. Volpert, «Multiphase continuum modeling of thrombosis in aneurysms and recirculation zones», *Phys. Fluids*, vol. 33, fasc. 9, p. 093314, set. 2021, doi: 10.1063/5.0057393.

[75] A. S. Bedekar, K. Pant, Y. Ventikos, e S. Sundaram, «A Computational Model Combining Vascular Biology and Haemodynamics for Thrombosis Prediction in Anatomically Accurate Cerebral Aneurysms», *Food Bioprod. Process.*, vol. 83, fasc. 2, pp. 118–126, giu. 2005, doi: 10.1205/fbp.05020.

[76] S. Zimny *et al.*, «A Multiscale Approach for the Coupled Simulation of Blood Flow and Thrombus Formation in Intracranial Aneurysms», *Procedia Comput. Sci.*, vol. 18, pp. 1006–1015, 2013, doi: 10.1016/j.procs.2013.05.266.

[77] D. M. Sforza, C. M. Putman, e J. R. Cebral, «Hemodynamics of Cerebral Aneurysms», *Annu. Rev. Fluid Mech.*, vol. 41, fasc. 1, pp. 91–107, gen. 2009, doi: 10.1146/annurev.fluid.40.111406.102126.

[78] A. Keedy, «An overview of intracranial aneurysms», *McGill J. Med. MJM Int. Forum Adv. Med. Sci. Stud.*, vol. 9, fasc. 2, pp. 141–146, lug. 2006.

[79] Morón F, Benndorf G, Akpek S, Dempsy R, Strother CM., «Spontaneous thrombosis of a traumatic posterior cerebral artery aneurysm in a chil», *AJNR Am J Neuroradiol*, vol. 26, 2005.

[80] K. Gester *et al.*, «In Vitro Evaluation of Intra-Aneurysmal, Flow-Diverter-Induced Thrombus Formation: A Feasibility Study», *Am. J. Neuroradiol.*, vol. 37, fasc. 3, pp. 490–496, mar. 2016, doi: 10.3174/ajnr.A4555.

[81] J. Xiang *et al.*, «Hemodynamic–Morphologic Discriminants for Intracranial Aneurysm Rupture», *Stroke*, vol. 42, fasc. 1, pp. 144–152, gen. 2011, doi: 10.1161/STROKEAHA.110.592923.

[82] S. S. Shishir, Md. A. K. Miah, A. K. M. S. Islam, e A. B. M. T. Hasan, «Blood Flow Dynamics in Cerebral Aneurysm - A CFD Simulation», *Procedia Eng.*, vol. 105, pp. 919–927, 2015, doi: 10.1016/j.proeng.2015.05.116.

[83] Ø. Evju e K.-A. Mardal, «On the Assumption of Laminar Flow in Physiological Flows: Cerebral Aneurysms as an Illustrative Example», in *Modeling the Heart and the Circulatory System*, vol. 14, A. Quarteroni, A c. di, in MS&A, vol. 14. , Cham: Springer International Publishing, 2015, pp. 177–195. doi: 10.1007/978-3-319-05230-4_7.

[84] D. Ribeiro de Sousa *et al.*, «Determination of a shear rate threshold for thrombus formation in intracranial aneurysms», *J. NeuroInterventional Surg.*, vol. 8, fasc. 8, pp. 853–858, ago. 2016, doi: 10.1136/neurintsurg-2015-011737.

[85] K. Ravindran, A. M. Casabella, J. Cebral, W. Brinjikji, D. F. Kallmes, e R. Kadirvel, «Mechanism of Action and Biology of Flow Diverters in the Treatment of Intracranial Aneurysms», *Neurosurgery*, vol. 86, fasc. Supplement_1, pp. S13–S19, gen. 2020, doi: 10.1093/neuros/nyz324.

[86] T. Lenz-Habijan *et al.*, «Comparison of the Thrombogenicity of a Bare and Antithrombogenic Coated Flow Diverter in an In Vitro Flow Model», *Cardiovasc. Intervent. Radiol.*, vol. 43, fasc. 1, pp. 140–146, gen. 2020, doi: 10.1007/s00270-019-02307-5.

[87] G. Girdhar *et al.*, «Thrombogenicity assessment of Pipeline, Pipeline Shield, Derivo and P64 flow diverters in an in vitro pulsatile flow human blood loop model», *eNeurologicalSci*, vol. 14, pp. 77–84, mar. 2019, doi: 10.1016/j.ensci.2019.01.004.

[88] L. Marroquin *et al.*, «Management and outcomes of patients with left atrial appendage thrombus prior to percutaneous closure», *Heart*, vol. 108, fasc. 14, pp. 1098–1106, lug. 2022, doi: 10.1136/heartjnl-2021-319811.

[89] M. M. Farkowski *et al.*, «Diagnosis and management of left atrial appendage thrombus in patients with atrial fibrillation undergoing cardioversion or percutaneous left atrial procedures: results of the European Heart Rhythm Association survey», *EP Eur.*, vol. 22, fasc. 1, pp. 162–169, gen. 2020, doi: 10.1093/europace/euz257.

[90] R. Beigel, N. C. Wunderlich, S. Y. Ho, R. Arsanjani, e R. J. Siegel, «The Left Atrial Appendage: Anatomy, Function, and Noninvasive Evaluation», *JACC Cardiovasc. Imaging*, vol. 7, fasc. 12, pp. 1251–1265, dic. 2014, doi: 10.1016/j.jcmg.2014.08.009.

[91] G. M. Bosi *et al.*, «Computational Fluid Dynamic Analysis of the Left Atrial Appendage to Predict Thrombosis Risk», *Front. Cardiovasc. Med.*, vol. 5, p. 34, apr. 2018, doi: 10.3389/fcvm.2018.00034.

[92] L. Di Biase *et al.*, «Does the Left Atrial Appendage Morphology Correlate With the Risk of Stroke in Patients With Atrial Fibrillation?», *J. Am. Coll. Cardiol.*, vol. 60, fasc. 6, pp. 531–538, ago. 2012, doi: 10.1016/j.jacc.2012.04.032.

[93] M. García-Villalba *et al.*, «Demonstration of Patient-Specific

Simulations to Assess Left Atrial Appendage Thrombogenesis Risk», *Front. Physiol.*, vol. 12, p. 596596, feb. 2021, doi: 10.3389/fphys.2021.596596.

[94] M. Hautmann *et al.*, «Left atrial appendage thrombus formation, potential of resolution and association with prognosis in a large real-world cohort», *Sci. Rep.*, vol. 13, fasc. 1, p. 889, gen. 2023, doi: 10.1038/s41598-023-27622-3.

[95] Musotto Giulio, «The role of patient specific morphology and contractility of the left atrial appendage on the thromboembolic risk in atrial fibrillation», Università degli Studi di Palermo, 2022.

[96] «The MathWorks, Inc. (2022). MATLAB version: 9.13.0 (R2022b). Accessed: January 01, 2023.» [Online]. Disponibile su: Available: https://www.mathworks.com

[97] T. Watson, E. Shantsila, e G. Y. Lip, «Mechanisms of thrombogenesis in atrial fibrillation: Virchow's triad revisited», *The Lancet*, vol. 373, fasc. 9658, pp. 155–166, gen. 2009, doi: 10.1016/S0140-6736(09)60040-4.